

# Early results in the search for extreme coronal line emitters with the Dark Energy Spectroscopic Instrument

Peter Clark<sup>1,2</sup>\*, Joseph Callow<sup>1,2</sup>†, Or Gaur<sup>1,2,3</sup>, Alexei V. Filippenko<sup>1,4</sup>, Thomas G. Brink<sup>1,4</sup>, WeiKang Zheng<sup>1,4</sup>, Jessica Aguilar<sup>1,5</sup>, Steven Ahlen<sup>1,6</sup>, Segev BenZvi<sup>1,7</sup>, Davide Bianchi<sup>1,8,9</sup>, David Brooks<sup>1,10</sup>, Todd Claybaugh<sup>1,5</sup>, Andrei Cuceu<sup>1,5</sup>, Axel de la Macorra<sup>1,11</sup>, Arjun Dey<sup>1,12</sup>, Peter Doel<sup>1,10</sup>, Jaime E. Forero-Romero<sup>1,13,14</sup>, Enrique Gaztañaga<sup>1,15,2,16</sup>, Satya Gontcho A Gontcho<sup>1,5,17</sup>, Gaston Gutierrez<sup>1,18</sup>, Victoria Fawcett<sup>1,19</sup>, Mustapha Ishak<sup>1,20</sup>, Jorge Jimenez<sup>1,21</sup>, Dick Joyce<sup>1,22</sup>, Stephanie Juneau<sup>1,22</sup>, Theodore Kisner<sup>1,5</sup>, Anthony Kremin<sup>1,5</sup>, Martin Landriau<sup>1,5</sup>, Laurent Le Guillou<sup>1,23</sup>, Marc Manera<sup>1,24,21</sup>, Aaron Meisner<sup>1,22</sup>, Ramon Miquel<sup>1,25,21</sup>, John Moustakas<sup>1,26</sup>, Seshadri Nadathur<sup>1,2</sup>, Will J. Percival<sup>1,27,28,29</sup>, Francisco Prada<sup>1,30</sup>, Ignasi Pérez-Ràfols<sup>1,31</sup>, Graziano Rossi<sup>1,32</sup>, Eusebio Sanchez<sup>1,33</sup>, David Schlegel<sup>1,5</sup>, Michael Schubnell<sup>1,34,35</sup>, Joseph Harry Silber<sup>1,5</sup>, David Sprayberry<sup>1,22</sup>, Gregory Tarlé<sup>1,35</sup>, Benjamin A. Weaver<sup>1,22</sup>, Rongpu Zhou<sup>1,5</sup> and Hu Zou<sup>1,36</sup>

<sup>1</sup> School of Physics and Astronomy, University of Southampton, Southampton, SO17 1BJ, UK

<sup>2</sup> Institute of Cosmology and Gravitation, University of Portsmouth, Portsmouth, PO1 3FX, UK

<sup>3</sup> Department of Astrophysics, American Museum of Natural History, New York, NY 10024, USA

<sup>4</sup> Department of Astronomy, University of California, Berkeley, CA 94720-3411, USA

<sup>5</sup> Lawrence Berkeley National Laboratory, 1 Cyclotron Road, Berkeley, CA 94720, USA

<sup>6</sup> Physics Dept., Boston University, 590 Commonwealth Avenue, Boston, MA 02215, USA

<sup>7</sup> Department of Physics & Astronomy, University of Rochester, 206 Bausch and Lomb Hall, P.O. Box 270171, Rochester, NY 14627-0171, USA

<sup>8</sup> Dipartimento di Fisica “Aldo Pontremoli”, Università degli Studi di Milano, Via Celoria 16, I-20133 Milano, Italy

<sup>9</sup> INAF-Osservatorio Astronomico di Brera, Via Brera 28, 20122 Milano, Italy

<sup>10</sup> Department of Physics & Astronomy, University College London, Gower Street, London, WC1E 6BT, UK

<sup>11</sup> Instituto de Física, Universidad Nacional Autónoma de México, Circuito de la Investigación Científica, Ciudad Universitaria, Cd. de México C. P. 04510, México

<sup>12</sup> NSF NOIRLab, 950 N. Cherry Ave., Tucson, AZ 85719, USA

<sup>13</sup> Departamento de Física, Universidad de los Andes, Cra. 1 No. 18A-10, Edificio Ip, CP 111711, Bogotá, Colombia

<sup>14</sup> Observatorio Astronómico, Universidad de los Andes, Cra. 1 No. 18A-10, Edificio H, CP 111711 Bogotá, Colombia

<sup>15</sup> Institut d'Estudis Espacials de Catalunya (IEEC), c/ Esteve Terradas 1, Edifici RDIT, Campus PMT-UPC, 08860 Castelldefels, Spain

<sup>16</sup> Institute of Space Sciences, ICE-CSIC, Campus UAB, Carrer de Can Magrans s/n, 08913 Bellaterra, Barcelona, Spain

<sup>17</sup> University of Virginia, Department of Astronomy, Charlottesville, VA 22904, USA <sup>18</sup> Fermi National Accelerator Laboratory, PO Box 500, Batavia, IL 60510, USA

<sup>19</sup> European Southern Observatory, Karl-Schwarzschild-Straße 2, 85748 Garching bei München, Germany

<sup>20</sup> Department of Physics, The University of Texas at Dallas, 800 W. Campbell Rd., Richardson, TX 75080, USA

<sup>21</sup> Institut de Física d'Altes Energies (IFAE), The Barcelona Institute of Science and Technology, Edifici Cn, Campus UAB, 08193, Bellaterra (Barcelona), Spain

<sup>22</sup> NSF NOIRLab, 950 N. Cherry Ave., Tucson, AZ 85719, USA

<sup>23</sup> Sorbonne Université, CNRS/IN2P3, Laboratoire de Physique Nucléaire et de Hautes Energies (LPNHE), FR-75005 Paris, France

<sup>24</sup> Departament de Física, Serra Húnter, Universitat Autònoma de Barcelona, 08193 Bellaterra (Barcelona), Spain

<sup>25</sup> Institució Catalana de Recerca i Estudis Avançats, Passeig de Lluís Companys, 23, 08010 Barcelona, Spain

<sup>26</sup> Department of Physics and Astronomy, Siena College, 515 Loudon Road, Loudonville, NY 12211, USA

<sup>27</sup> Department of Physics and Astronomy, University of Waterloo, 200 University Ave W, Waterloo, ON N2L 3G1, Canada

<sup>28</sup> Perimeter Institute for Theoretical Physics, 31 Caroline St. North, Waterloo, ON N2L 2Y5, Canada

<sup>29</sup> Waterloo Centre for Astrophysics, University of Waterloo, 200 University Ave W, Waterloo, ON N2L 3G1, Canada

<sup>30</sup> Instituto de Astrofísica de Andalucía (CSIC), Glorieta de la Astronomía, s/n, E-18008 Granada, Spain

<sup>31</sup> Departament de Física, EEBE, Universitat Politècnica de Catalunya, c/Eduard Maristany 10, 08930 Barcelona, Spain

<sup>32</sup> Department of Physics and Astronomy, Sejong University, 209 Neungdong-ro, Gwangjin-gu, Seoul 05006, Republic of Korea

<sup>33</sup> CIEMAT, Avenida Complutense 40, E-28040 Madrid, Spain

<sup>34</sup> Department of Physics, University of Michigan, 450 Church Street, Ann Arbor, MI 48109, USA

<sup>35</sup> University of Michigan, 500 S. State Street, Ann Arbor, MI 48109, USA

## ABSTRACT

Here we present the results of our search through the Early Data Release (EDR) of the Dark Energy Spectroscopic Instrument (DESI) for extreme coronal line emitters (ECLEs) - a rare classification of galaxies displaying strong, high-ionization iron coronal emission lines within their spectra. With the requirement of a strong X-ray continuum to generate the coronal emission, ECLEs have been linked to both active galactic nuclei (AGNs) and tidal disruption events (TDEs). We focus our search on identifying TDE-linked ECLEs. We identify three such objects within the EDR sample, highlighting DESI's effectiveness for discovering new nuclear transients, and determine a galaxy-normalized TDE-linked ECLE rate of  $R_G = 5_{-3}^{+5} \times 10^{-6}$  galaxy $^{-1}$  yr $^{-1}$  at a median redshift of  $z = 0.2$  - broadly consistent with previous works. Additionally, we also identify more than 200 AGNs displaying coronal emission lines, which serve as the primary astrophysical contaminants in searches for TDE-related events. We also include an outline of the custom python code developed for this search.

**Key words:** transients: tidal disruption events – galaxies: active

## 1 INTRODUCTION

Extreme coronal line emitters (ECLEs) are defined by the presence of prominent coronal emission lines from highly ionised iron ([Fe vii], [Fe x], [Fe xi], [Fe xiv]) in their spectra. Such emission lines are rare, requiring a high-energy X-ray continuum to generate, and are most commonly seen in the Solar corona (giving them their name). The two primary sources for extragalactic coronal lines are active galactic nuclei (AGNs) and tidal disruption events (TDEs).

The actively accreting central supermassive black hole (SMBH) in an AGN can generate the requisite X-ray continuum to produce coronal lines. If present, these lines are typically seen with line strengths of a few percent that of the [O III]  $\lambda 5007\text{\AA}$  line (Nagao et al. 2000). Due to the common use of the abbreviation 'CL' when referring to 'changing look' AGN in the literature, to avoid potential confusion we abbreviate 'coronal line' to 'CrL' throughout this work. Thus, and AGN displaying coronal line emission is referred to as a 'CrL AGN'. In ECLEs, however, the coronal lines are much stronger, with some exceeding 30 per cent the strength of [O III]  $\lambda 5007\text{\AA}$  (Wang et al. 2012). Only a small fraction of CL-AGNs are ECLEs, which indicates that AGN-linked ECLEs may either be drawn from the high end of a continuum of AGN CL activity or reflect unique environments around some SMBHs.

TDEs are luminous flaring transients produced by the gravitational shredding of a star that passes too close to its galaxy's central SMBH. Around half of the star's mass remains gravitationally bound to the SMBH following the disruption and produces an accretion disk of accreting material (Ulmer 1999). The mass eventually accreted is significantly less than the initial bound mass, with more material becoming unbound as the system evolves (Ayal et al. 2000). Analysis suggests that the majority of TDEs involve SMBHs of  $< 10^8 M_\odot$ . At larger SMBH masses the Roche limit (the radius within which a star will be tidally disrupted) of a solar like star is within the SMBH's event horizon resulting in the star being absorbed prior to disruption and so producing no observable transient (Hills 1975). While the details of TDE emission are still debated, the circularisation of material into the accretion disk or collisions within the infalling material streams (or a combination of both) are the currently preferred mechanisms (e.g., Lacy et al. 1982; Phinney 1989; Evans & Kochanek 1989).

The first ECLEs were discovered by Komossa et al. (2008), Wang et al. (2011) and Wang et al. (2012). Spectroscopic follow-up obser-

vations of the Wang et al. (2012) sample of seven ECLEs selected from the seventh data release of the Sloan Digital Sky Survey (SDSS; York et al. 2000), conducted by Yang et al. (2013), revealed the coronal emission lines in four of the seven objects to have faded during the interim several years. This indicated that the process involved in generating the CrLs was transient in nature, as expected from a TDE. Mid-infrared (MIR) analysis conducted by Dou et al. (2016) showed that those objects with fading coronal lines showed long-term declines in their MIR luminosities and changes in colour, evolving from AGN-like values at the start of observations to colours expected of non-AGN hosts.

These analyses have been corroborated and extended by Clark et al. (2024) through additional follow-up spectroscopy obtained nearly two decades after the original SDSS spectra. Two of the Wang et al. (2012) objects displayed persistent coronal lines, as well as optical and MIR luminosity and colour variability consistent with AGN activity. We treat these objects as AGN-ECLEs. We note that the physical division between these and other AGNs that display coronal lines is unclear, other than the elevated strength of the coronal emission. The remaining five objects display no re-brightening of their coronal lines, with the latest observations (obtained in 2021) showing that three now lack all coronal emission lines, with the remaining two (SDSS J1241+4426 and SDSS J1342+0530) displaying only the lowest-energy [Fe viii] lines. This spectral evolution and the long-term power-law declines in the MIR emission of these five objects were found to remain consistent with a TDE origin. We term objects such as these TDE-ECLEs.

TDEs are known to be X-ray luminous, e.g., Auchettl et al. 2017, 2018. In the case of TDE-ECLEs, the initial disruption and subsequent accretion processes produce an intense X-ray continuum that ionises material at some (individual system dependent) distance from the SMBH. It is this material - unrelated to the star being disrupted - that is responsible for both the coronal emission lines and the reprocessing of the UV-optical flux into the long-term MIR emission seen in ECLEs. Observations have shown this emission can persist for several years following the TDE, compared to the months to years-long duration of the direct emission from the TDE seen in the optical and UV. Given that these ECLEs are driven by the reprocessing of TDE emission, they can be thought of as TDE light echoes.

Recently, direct links between TDEs and ECLEs have been made through observations of coronal emission lines developing in the spectra of live TDEs where the TDE was identified whilst the direct emission was still visible. Whilst only a small number of examples are currently known (14 at time of writing see, e.g., Fraser et al. 2017; Neustadt et al. 2020; Onori et al. 2022; Newsome et al. 2022;

\* E-mail: P.S.J.Clark@soton.ac.uk

† E-mail: joecallow2809@gmail.com

Wang et al. 2024; Hinkle et al. 2024; Clark et al. 2025), there is already indication of significant variation in properties (e.g., the time-lag between the occurrence of the TDE and the emergence of the coronal lines) which is likely to increase as more such objects are identified. Clark et al. (2025) explored the MIR properties of these objects and identified tentative evidence of a colour-luminosity relationship. Specifically, for TDEs that are observed with coronal lines, those with brighter MIR flares show more significant reddening at outburst, potentially related to material covering fractions or other environmental conditions increasing the level of MIR reprocessing. Such a relation was not seen in the AGNs explored in the study, which also displayed much smaller changes in peak MIR luminosity overall. Other work has also shown that differences in the MIR properties of TDEs and AGNs could be used as a distinguishing characteristic (Hinkle 2024; Yao et al. 2025).

This work describes the results of a new systematic search for ECLEs in the early data release (EDR) of the Dark Energy Spectroscopic Instrument (DESI; DESI Collaboration et al. 2016a,b; Schlafly et al. 2023; Miller et al. 2024; Poppett et al. 2024) and includes an outline of our custom python code for detecting and analysing ECLEs, the Spectroscopic Light Echo Identification Protocol Now in Realtime SLEIPNIR<sup>1</sup>. As described in Callow et al. (2024, 2025), SLEIPNIR has already been used on the data from two SDSS surveys, exploring both the SDSS Legacy DR17 (Abdurro'uf et al. 2022) and Baryon Oscillation Spectroscopic Survey (BOSS) LOWZ (Dawson et al. 2013) surveys. As part of these analyses, SLEIPNIR successfully retrieved all seven objects from the original systematic search conducted in SDSS DR7 (Abazajian et al. 2009) by Wang et al. (2012), one new TDE-ECLE in BOSS LOWZ, as well as numerous other candidates that were ultimately classified as AGN-ECLEs.

Whilst the sample size of TDE-ECLEs is still small, rates analyses are already providing important insights. Work conducted on the previous SDSS-based samples in Callow et al. (2024, 2025) find the observed rates of TDE-ECLEs to be consistent with the general observed TDE rate, if between 10 and 40 per cent of TDEs display ECLE behaviour. Larger samples of TDE-ECLEs obtained over a range of redshifts will be needed to reduce the statistical uncertainties of such rate calculations, made challenging by the inherently low rates of TDEs generally and the wide time scales over which such behaviour can occur. The exploration of large spectroscopic samples is thus essential to improve our understanding of ECLEs.

We structure the work as follows. In Section 2 we outline the spectroscopic and photometric datasets along with the value-added catalogue used to identify and classify our identified ECLE candidates. In Section 3, we describe our SLEIPNIR code and outline sources of potential contamination for similar searches and how these are dealt with in our survey. In Section 4 we describe the construction, processing, and classification of the DESI EDR ECLE sample. In Section 5 we move to specific descriptions of the most promising candidates identified through the search, including three objects we identify as being linked to TDEs. A sample of AGNs with coronal emission lines (CrL-AGNs) identified in the EDR search, which whilst not the focus of this work, can serve as a reference catalogue and basis for further work on such objects, is described in Appendix 5.2. In Section 6, we discuss the properties of our newly identified TDE-ECLEs and place their MIR evolution in context with the existing sample. We also determine galaxy normalised, mass normalised, and volumetric rates for TDE-linked ECLEs based on our analysis of DESI EDR, finding these to be broadly consistent with rates determined in pre-

vious works. Finally, in Section 7 we summarise our findings that DESI is an effective search engine for TDE linked ECLEs and other coronal line displaying galaxies whilst highlighting the importance of follow-up spectroscopy to confirm the evolution and classification of such objects.

## 2 OBSERVATIONS AND DATA REDUCTION

A condensed summary of the spectroscopic datasets used in this work is given in Table 1, with the corresponding information for the photometric datasets given in Table 2.

At all times, unless otherwise stated, apparent magnitudes are given as observed, with no additional corrections. In contrast, absolute magnitudes have been corrected for Milky Way extinction using the appropriate photometric extinction coefficient. Unless specified otherwise, these coefficients have been retrieved from Schlafly & Finkbeiner (2011). To match the preferred extinction parameters of Schlafly & Finkbeiner (2011), we apply the extinction law of Fitzpatrick (1999) throughout this paper and assume  $R_V = 3.1$ .

Throughout, when converting between apparent and absolute magnitudes we assume a Hubble-Lemaître constant  $H_0 = 73 \text{ km s}^{-1} \text{ Mpc}^{-1}$  and adopt a standard cosmological model with  $\Omega_M = 0.27$  and  $\Omega_\Lambda = 0.73$ .

### 2.1 Optical spectroscopy

#### 2.1.1 Dark Energy Spectroscopic Instrument: DESI

All DESI spectra included in this work are now publicly available through the EDR and were obtained as part of the DESI survey validation programs. (DESI Collaboration et al. 2024d,e).

The spectra were processed by the custom DESI spectroscopic pipeline, which includes a full suite of processing and correction steps to provide fully flux- and wavelength-calibrated spectra (Guy et al. 2023).

DESI itself is designed primarily as a cosmological experiment, and whilst not the focus of this work, Data Release 1 provides a range of state-of-the-art cosmological analyses, including two-point clustering measurements and validation (DESI Collaboration et al. 2024a), baryon-acoustic oscillation (BAO) measurements from galaxies and quasars (DESI Collaboration et al. 2025c), and from the Ly $\alpha$  forest (DESI Collaboration et al. 2025e), as well as a full-shape study of galaxies and quasars (DESI Collaboration et al. 2024b). There are Cosmological results from the BAO measurements (DESI Collaboration et al. 2025d,b) and the full-shape analysis (DESI Collaboration et al. 2024c), as well as constraints on primordial non-gaussianities.

#### 2.1.2 GEMINI

We obtained optical spectra of two of our TDE-ECLE candidates (see Section 4 for details on candidate selection) using the Gemini Multi-Object Spectrograph (GMOS; Hook et al. 2004) on the 8.1 m Gemini South Telescope (Gemini-S) on Cerro Pachón, Chile as part of the Gemini program GS-2021B-FT-202 (PI: P. Clark). Observations were made using a combination of the B600 and R831 gratings. Data were reduced using the Data Reduction for Astronomy from Gemini Observatory North and South (DRAGONS) reduction package (Labrie et al. 2019), using the standard recipe for GMOS long-slit reductions. This includes bias correction, flat fielding, wavelength calibration, and flux calibration. As we did not have telluric

<sup>1</sup> <https://github.com/Lightbulb500/SLEIPNIR>

**Table 1.** Summary information for the spectral datasets used in this work.

Telescope	Instrument	Wavelength Range <sup>1</sup>	Type <sup>2</sup>	No. Utilised
Mayall-4m	DESI	3600–9825	Classification	634551
GEMINI	GMOS-S	3860–9330	Follow-up	2
NOT	ALFOSC	3500–9635	Follow-up	3
Keck 10m	LRIS	3135–10255	Follow-up	3
SDSS 2.5m	SDSS Legacy	3585–10400	Archival	2
SDSS 2.5m	SDSS BOSS	3810–9180	Archival	1

Notes: <sup>1</sup> In the observer frame. Due to differences between instrumental configurations used for some spectra, ranges are approximate.

<sup>2</sup> Classification: Spectra used to initially identify ECLE candidates. Archival: Spectra obtained significantly before the classification to identify any existing long-term variability. Follow-up: Spectra of previously identified candidates obtained after classification used to explore coronal line variability and/or improve obtain higher S/N data for individual objects of interest.

standards for these observations, we do not attempt telluric correction of these spectra.

### 2.1.3 Nordic Optical Telescope: NOT

We obtained follow-up spectra of several ECLE candidates using the Nordic Optical Telescope (NOT) and the Alhambra Faint Object Spectrograph and Camera (ALFOSC). These spectra were all obtained using a one arcsecond slit and Grism #4. Data reduction was conducted using a modified version of the pyNOT-REDUX (Krogager 2025) package. Reduction included wavelength calibration to a He arc lamp and flux calibration using observations of a standard star obtained on the same night as the science observations.

### 2.1.4 Sloan Digital Sky Survey: SDSS

Where available, we compared our ECLE candidates to archival spectra obtained by the SDSS several years prior to the classification spectra. These spectra were retrieved from SDSS DR18 (Almeida et al. 2023) and accessed using the Casjobs system. Due to the differing targeting parameters of SDSS and DESI, only three of the identified ECLE candidates have corresponding SDSS spectra.

### 2.1.5 Keck

We acquired spectra of three of our ECLE candidates with the Low Resolution Imaging Spectrometer (LRIS; Oke et al. 1995) on the 10m Keck I telescope at the W. M. Keck Observatory. These observations utilized the one arcsecond slit, the D560 dichroic, the 600/4000 grism, and the 400/8500 grating. This instrument configuration produced a combined wavelength range of  $\sim 3200$ –10200 Å, and a spectral resolving power of  $R \approx 900$ . To minimize slit losses caused by atmospheric dispersion (Filippenko 1982), the slit was oriented at or near the parallactic angle. The LRIS spectra were reduced with the LPIPE data reduction pipeline (Perley 2019).

## 2.2 Optical photometry

### 2.2.1 Asteroid Terrestrial-impact Last Alert System: ATLAS

ATLAS data were retrieved using the ATLAS forced-photometry server (Shingles et al. 2021).<sup>2</sup> ATLAS uses two broad-band filters: ‘cyan’ (*c*; approximately equivalent to *g* + *r*) and ‘orange’ (*o*; approximately equivalent to *r* + *i*). ATLAS observations are available

over the general MJD range 57227–60724 and were processed using a modified version of PLOT\_ATLAS\_FP.PY (Young 2024).

### 2.2.2 DESI Legacy Imaging Surveys

We utilise the DESI Legacy Imaging Surveys (Dey et al. 2019) to retrieve processed composite *grz* cut-out images of the locations of candidates to provide contextual information on their morphology.

### 2.2.3 Liverpool Telescope: LT

We obtained *ugriz*-photometry of several targets using the Liverpool Telescope (LT) using the IO:O instrument (Steele et al. 2004). The LT *ugriz*-band photometry was measured on the pre-processed imaging following median stacking using YSFITSUTIL (Bach 2023). Photometric extraction was then conducted using AUTOPHOT (Brennan & Fraser 2022) using the Moffat point spread function (PSF) (Moffat 1969) with calibration to the SDSS magnitude system using the SDSS DR16 photometric catalogue (Ahumada et al. 2020) retrieved from VizieR (Ochsenbein et al. 2000).<sup>3</sup>

### 2.2.4 Zwicky Transient Facility: ZTF

ZTF observations were made using the *gri* filters and retrieved using the ZTF Forced Photometry Service (ZFPS; Masci et al. 2023). These observations cover an overall MJD range of 58301–60725, with the specific MJD range changing slightly for each candidate explored.

## 2.3 Infrared photometry

### 2.3.1 Two Micron All-Sky Survey: 2MASS

To explore the behaviour of each identified object of interest well before its DESI spectrum, we retrieve near-infrared (NIR) photometry obtained by the Two Micron All-Sky Survey (2MASS; Skrutskie et al. 2006) from IRSA. These data consist of *JHK* photometric observations and are used to explore objects of interest in the *J*–*H* vs. *H*–*K* parameter space.

This parameter space is useful in distinguishing the source of IR emission as primarily the result of an AGN or from starlight (Hyland & Allen 1982; Komossa et al. 2009). However, we note that given the wide range of NIR colours displayed by galaxies of the same spectroscopic classification, they cannot be distinguished effectively using these NIR colours alone. Additionally, given the time offset

<sup>2</sup> <https://fallingstar-data.com/forcedphot/>

<sup>3</sup> <https://vizier.cds.unistra.fr/>

between the 2MASS and DESI observations, evolution in the NIR will not have been observed.

### 2.3.2 Wide-field Infrared Survey Explorer: WISE

Following the method described by Clark et al. (2024), we retrieve the available MIR photometry for each candidate ECLE identified by SLEIPNIR. These MIR observations were obtained by the *Wide-field Infrared Survey Explorer* (WISE), from both the AllWISE (Wright et al. 2010) and NEOWISE Reactivation Releases (NEOWISE-R) (Mainzer et al. 2011, 2014) from the NASA/IPAC infrared science archive (IRSA).<sup>4</sup>

As WISE obtained images of each region of the sky in observing visits that comprise several observations on a  $\sim$  daily cadence in blocks spaced approximately six months apart, we process the data to give a weighted average magnitude per observational block. Work by Dou et al. (2016) previously explored whether the known sample of ECLEs presented variability during each observation block, with no such variability detected. As such, combining the individual observations allows for any long-term trends to be seen more easily.

We process the WISE photometry with a custom Python script. In addition to generating the weighted per block magnitudes, the script filters out any observation that was marked as an upper limit or which was observed when the spacecraft was close to the South Atlantic Anomaly ( $saa\_sep < 5.0$ ) or the sky position of the Moon ( $moon\_masked = 1$ ). Additionally, any observations with a low frame quality or that suffered from potential ‘contamination or confusion’ as flagged by the WISE pipeline were also removed prior to further processing.

## 2.4 Radio photometry

Significant radio emission can be used as an identifying diagnostic of AGN activity (see e.g., Best et al. 2005). To aid in distinguishing TDE sources from ongoing AGN activity, we explore the positions of our most promising candidates (see Section 5) in several radio surveys.

### 2.4.1 Very Large Array Faint Images of the Radio Sky at Twenty-Centimeters (VLA FIRST)

We searched the Very Large Array Faint Images of the Radio Sky at Twenty-Centimeters (VLA FIRST) catalogue<sup>5</sup> for any recorded sources within 10 arcseconds of our TDE candidates, with no sources returned. We additionally visually inspected one arcminute cutouts around each candidate to confirm this lack of identified source. A possible faint source is tentatively visible at the position of one candidate (see Section 5.1.3) though is close to the level of other spurious sources in the region. Given its overall faintness and lack of detection in other radio data (Section 2.4.2), we do not consider this an indication of radio-AGN activity.

### 2.4.2 Very Large Array Sky Survey: VLASS

We explored the VLASS Quick Look Epoch 1 catalogue (Gordon et al. 2021b) accessed via its VizieR instance (Gordon et al. 2021a).

<sup>4</sup> <https://irsa.ipac.caltech.edu/>

<sup>5</sup> Accessed through: <https://sundog.stsci.edu/cgi-bin/searchfirst>

We searched for any identified sources within 25 arcseconds of each candidate position, with this search retrieving no catalogued sources.

To confirm this, and to search for variability in other epochs, we visually inspected the locations of each promising ECLE candidate in the VLASS datasets available through the VLASS Quicklook All Epochs interactive map.<sup>6</sup> No significant sources were observed in any epochs at the location of the candidates, ruling out the presence of any radio-loud AGN activity over the course of the epochs explored in the 2 – 4 GHz range covered by VLASS. This dataset covers an overall timespan of 2017 September (Epoch 1.1) through 2024 October (Epoch 3.2).

### 2.4.3 Low-Frequency array two-metre sky survey: LoTSS

Finally we search for sources in the Low-Frequency array two-metre sky survey (LoTSS) DR2 catalogue (Shimwell et al. 2022). Three of our candidates are within the sky-coverage of LoTSS-DR2, with one candidate closely associated with a detected radio source indicative of AGN activity, see Section 5.2.5.

## 2.5 FASTSPECFIT value added catalogue

In addition to the DESI spectra, we also make use of the FASTSPECFIT (Moustakas et al. 2023) value added catalogue (VAC) to provide additional information on the identified ECLE candidates and wider EDR sample as a whole. An outline of the parameters from FASTSPECFIT used in this work is given in Appendix A Table A1.

To generate a reference sample to compare our candidates to the overall population, we retrieve all DESI galaxies within the FASTSPECFIT EDR catalogue (initial sample size : 1,397,479 galaxies) and apply the following cuts:

- $0.01 < Z < 0.45$  : Matches the redshift range of the main search for EDR ECLEs.
- $ZWARN = 0$  : Objects that have reliable redshift measurement.
- $SFR > 0$  : Objects for which a star formation rate was measurable.

Following these cuts, our reference FASTSPECFIT sample is reduced to 388,858 individual galaxies.

## 3 SPECTROSCOPIC LIGHT ECHO IDENTIFICATION PROTOCOL NOW IN REAL-TIME: SLEIPNIR

SLEIPNIR is a PYTHON-based analysis routine designed to provide rapid identification of candidate ECLEs for more detailed analysis through triage of a large number of input spectra. Its primary goal is to identify possible candidates to significantly reduce the burden of manual visual inspection, which given the rarity of ECLEs (Wang et al. 2012; Clark et al. 2024; Callow et al. 2024, 2025) is a significant barrier to their discovery.

### 3.1 SLEIPNIR operation

#### 3.1.1 Inputs

In general, as inputs to the analysis, SLEIPNIR requires a spectrum to classify, a pre-determined redshift, and Milky Way extinction. In

<sup>6</sup> Accessed through: [https://archive-new.nrao.edu/vlass/HiPS/All\\_VLASS/Quicklook/](https://archive-new.nrao.edu/vlass/HiPS/All_VLASS/Quicklook/)

**Table 2.** Details of the photometric datasets used in this work.

Survey	Filters	MJD Range	Reference
<b>Optical</b>			
Asteroid Terrestrial-impact Last Alert System (ATLAS)	<i>c, o</i> <sup>1</sup>	57227 – 60724	Tonry et al. (2018); Shingles et al. (2021)
DESI Legacy Imaging Surveys	<i>g, r, z</i>	– <sup>2</sup>	Dey et al. (2019)
Liverpool Telescope (LT)	<i>u, g, r, i, z</i>	59792 – 60940	Steele et al. (2004)
Zwicky Transient Facility (ZTF)	<i>g, r, i</i>	58301 – 60725	Bellm et al. (2019); Masci et al. (2023)
<b>Infrared</b>			
The Two Micron All Sky Survey (2MASS)	<i>J, H, K</i>	50753 – 51838	Skrutskie et al. (2006)
AllWISE	<i>W1, W2, W3</i>	55203 – 55593	Wright et al. (2010)
NEOWISE-R	<i>W1, W2</i>	56640 – 60523	Mainzer et al. (2014)
<b>Radio</b>			
Very Large Array Faint Images of the Radio Sky at Twenty-Centimeters (VLA FIRST)	1.4 GHz	49473 – 56047 <sup>3</sup>	Becker et al. (1995)
Very Large Array Sky Survey (VLASS)	2 – 4 GHz	58000 – 60615 <sup>4</sup>	Lacy et al. (2020)
Low-Frequency array two-metre sky survey (LoTSS)	120 – 168 MHz	– <sup>5</sup>	Shimwell et al. (2022)

Notes: <sup>1</sup> ATLAS observations were made using two broad-band filters; *c* (cyan) is approximately equivalent to *g + r* and *o* (orange) is roughly *r + i*.

<sup>2</sup> Used for contextual imaging only.

<sup>3</sup> Overall MJD range. Data obtained at one epoch for each candidate.

<sup>4</sup> MJD range is approximate.

<sup>5</sup> Comprised of data obtained up to April 2021

In the case of the DESI analysis, SLEIPNIR also processes metadata for each spectrum to aid in classification. Such metadata includes the observation date of the spectrum, DESI targeting information, and pipeline processing flags. We discuss how these metadata are used to produce our input sample in Section 4.1.

### 3.1.2 Analysis outputs

As outputs, SLEIPNIR provides a rest frame spectrum (corrected for both redshift and Milky Way extinction), a general classification of the input spectrum as an ECLE candidate or not and an initial estimation of AGN activity based on simplistic Baldwin, Phillips and Telervich (BPT; Baldwin et al. 1981) emission line diagnostics. For each individual line analysed (see Section 3.1.3), the measured pseudo equivalent width (pEQW), line flux and signal-to-noise ratio (SNR) are also returned, along with a flag for the easy identification of lines detected with high SNRs (set by default to be  $> 10$ ). For the Fe coronal lines specifically, flags to indicate if each line meets all of the detection criteria and is considered ‘strong’ (see Section 3.1.3) are also returned. Input source-dependent metadata are also returned to aid in subsequent analysis of objects of interest. All textual outputs are returned in human and machine readable ascii files, for easy transfer of the data to an external database of the user’s choice for long-term and accessible storage.

In addition to these datafiles, SLEIPNIR also produces visual diagnostic diagrams for each of the identified candidates. These diagnostic diagrams include the processed input spectrum, spectral cutouts of the CrL regions, [O III]  $\lambda 5007\text{\AA}$  and H $\alpha$  complexes, BPT diagnostic diagrams, and a textual report on why the object was flagged for classification.

### 3.1.3 Line selection and measurements

A limited list of spectral lines were selected for analysis with SLEIPNIR and are listed below (see Table 3). These are primarily the Fe coronal lines, Balmer series, and the emission features used for AGN identification in BPT diagnostics. A few additional lines produced in high energy processes (e.g., [Ca xv]) or related to host galaxy properties (e.g., the extinction tracers Na I D and Mg I) are included

**Table 3.** Emission features used for candidate classification and analysis.

Line	Location (Å)	Line	Location (Å)
<b>Fe Coronal Lines</b>			
[Fe vii]	3759	<b>Other Coronal Lines</b>	
[Fe viii]	5160	[Ne v]	3347
[Fe viii]	5722	[Ne vi]	3427
[Fe viii]	6088	[Ca xv]	5446
[Fe ix]	6376		
[Fe x]	7894		
[Fe xiv]	5304		
<b>Other Lines</b>			
H $\alpha$	6562.790	[O I]	6300
H $\beta$	4861.350	[O I]	6363
H $\gamma$	4340.472	[O II]	3728.2725
H $\delta$	4101.734	[O III]	4959
		[O III]	5007
N II	6548		
N II	6584	Mg I	5175
S II	6717	[Ne III]	3869 **
S II	6731		
S II	6724 *	[He I]	4478
S III	6313	[He II]	4686
Na I D	5892.935 *		

Notes: \* Mean wavelength of a closely spaced doublet

\*\* This line was described incorrectly by both Yang et al. (2013) and Clark et al. (2024) as [Ne III]  $\lambda 3896\text{\AA}$ . The conclusions of these papers are not affected.

as well. Given their central importance to this analysis, the CrLs are explored in more detail.

A summary of the coronal lines used for analysis within SLEIPNIR is provided in Table 4. While SLEIPNIR only uses the Fe coronal lines to identify ECLE candidates, we also check for the existence of the [Ne v] and [Ca xv] coronal lines. These lines are not used for the initial identification because they are rarely covered by the DESI spectrographs in the redshift range studied here and because of the significant step change in energy required to produce [Ca xv]. The use of these coronal lines in SLEIPNIR will be revisited in future studies making use of data with different wavelength coverage (e.g.,

the NIR where coronal lines of S and Si are present (Kynoch et al. 2022) or when focused at higher redshifts.

All spectral lines are processed identically. Following a check to ensure the line is clear of possible edge effects by being too close to either the blue or red end of the spectrum (configured to be a conservative 50 Å), a conversion to velocity space relative to the expected position of the spectral line is applied. The region around the spectral line is then fitted with a linear continuum which is removed prior to the measurement of each line's spectral properties. An important caveat of the parameters provided from this analysis is that SLEIPNIR does not perform line fitting. Instead it measures the properties of lines in windows of fixed size using direct 'area under curve' methods. This method was chosen as a compromise between the individual accuracy of the measurements and operational speed given the large number of individual lines per spectrum. Testing has shown that the derived values are reliable, except in cases where multiple distinct features overlap (SLEIPNIR does not perform line de-blending) or for very broad features that extend beyond the fixed window for measurement. These are not concerns for the narrow and isolated CrL features of most interest to our study, but can significantly affect the automated measurement of BPT emission line ratios in the presence of broad features. As such, the BPT diagnostics provided by SLEIPNIR are treated as first pass indications of the presence (or absence) of AGN activity, with additional line analysis performed once promising candidates have been identified.

### 3.1.4 Candidate flagging

As SLEIPNIR returns measured parameters for each spectral line region (unless too close to the edge of the observational range), additional checks are used to confirm the detection of CrLs, as outlined in Table 5. These cuts are intended to remove the majority of false positive detections from weak or contaminated features.

Each CrL that passes these cuts contributes to an individual spectrum's 'ECLE score'. The four strongest CrLs ( $[\text{Fe viii}] \lambda 6088\text{\AA}$ ,  $[\text{Fe x}] \lambda 6376\text{\AA}$ ,  $[\text{Fe xi}] \lambda 7894\text{\AA}$ , and  $[\text{Fe xiv}] \lambda 5304\text{\AA}$ ) are each assigned an ECLE score of two. The three remaining, weaker  $[\text{Fe viii}]$  lines are each assigned an ECLE score of one. Given their relative weakness and reduced pEQW detection threshold, these lines contribute to the score only if  $[\text{Fe viii}] \lambda 6088\text{\AA}$  has met the detection criteria. The detection of all remaining lines is independent. As such, the maximum ECLE score a spectrum can reach is 11. In our search of DESI EDR, we set a threshold score of seven to flag a target for visual inspection. At redshifts exceeding 0.24, where the  $[\text{Fe xi}] \lambda 7894\text{\AA}$  line is too close to (or beyond) the red edge of the DESI spectrum, this scoring threshold is reduced to five to reflect the lower possible maximum ECLE score of nine.

We note that in contrast to the previous studies using earlier versions of SLEIPNIR (Callow et al. 2024, 2025), we do not apply the requirement that any of the Fe coronal lines have a pEQW exceeding 20 per cent that of  $[\text{O III}] \lambda 5007\text{\AA}$  for initial candidate identification. This threshold was motivated by analysis of the evolution of the initial ECLE sample observed in SDSS DR7 (Abazajian et al. 2009) by Wang et al. (2012) and was thought at the time to be a conclusive method of separating contaminating AGNs from TDE-linked objects. Late-time observations (Clark et al. 2024, 2025) of such objects has revealed that  $[\text{O III}]$  emission can develop over time as the Fe CrLs fade. With improvements to SLEIPNIR since previous studies (including improved spectral smoothing and handling of skylines) and the size of the overall DESI EDR input sample resulting in a manageable false positive rate, this constraint was removed. Scientifically, this provides two additional opportunities: late-time

TDE-ECLEs displaying strengthened  $[\text{O III}]$  emission will not be excluded from the initial samples and a sample of CrL-AGN displaying a wide range of Fe CrL line strengths can be collected for comparison purposes.

Given the range of properties displayed by the existing samples of ECLEs, SLEIPNIR has two additional candidate selection criteria: 'Strong CrL' flagging, and 'High line SNR' flagging. 'Strong CrL' flagging is triggered when any single CrL meets the detection criteria and both metrics for SNR exceed a threshold value, configured for our analysis to be ten. The motivation for this flag is to ensure that all objects with at least one CrL detected with high strength are visually inspected. The drawback for this condition is that, as it requires only one line to be detected, it is significantly more susceptible to contamination (particularly from residual skylines) and thus has a higher overall false positive rate. 'High line SNR' flagging is triggered when all  $[\text{Fe viii}]$  lines are detected with both SNR metrics exceeding a threshold (set to five in this analysis) and disregarding the pEQW line detection threshold. This flag is intended to capture any evolved objects where the higher ionisation state lines have already faded.

## 3.2 Potential sources of false positive or false negative ECLE detections

### 3.2.1 Skylines

Telluric emission lines or 'skylines' from the Earth's atmosphere can present significant contamination problems towards the red component of the optical range, though several strong lines are also present in the bluer spectral regions. A list of the skylines found to be most commonly problematic for ECLE identification is given in Table 6.

Whilst skyline removal is often conducted as part of spectral processing in large surveys (as is the case in both SDSS and DESI) and in the reduction of individual spectra, the removal of these lines can be challenging with the possibility of residual features remaining behind. Furthermore, there are two additional factors that make these residual skyline features particularly problematic in the search for ECLEs.

- (i) Skylines are narrow features produced by single line transitions. As such, if they are not removed fully, residual skyline features can present morphologies very similar to the narrow coronal lines targeted by CrL searches.
- (ii) At some redshifts, multiple skylines coincidentally align with several Fe features, compounding the potential for false positive detections.

Thankfully as skylines occur at fixed and known positions in the observer frame (see Table 6), objects with potential skyline contamination can be reliably identified and treated with additional care before classification as an ECLE candidate. Moreover SLEIPNIR includes the option to perform additional pre-processing of the spectra to remove and interpolate across the strongest skylines prior to the start of analysis. If required, the heavily contaminated telluric regions can be fully removed from consideration to reduce the number of false positive detections if these regions are a particular concern, though with the knock-on effect of reducing the ECLE recovery ability of SLEIPNIR at redshifts where coronal lines are present within these regions of the observer frame. Given the size of the EDR sample and the number of overall candidates retrieved, we do not employ this option in this work.

**Table 4.** Coronal lines used by SLEIPNIR.

Ion	Wavelength (Å) <sup>1</sup>	DESI z min <sup>2</sup>	DESI z max <sup>3</sup>	Required Energy (eV) <sup>4</sup>	Reference <sup>5</sup>
[Fe vii]	3759	0.0	> 0.45	98.985 ± 0.015	<a href="#">Gharaibeh et al. (2011)</a>
[Fe vii]	5160	0.0	> 0.45	98.985 ± 0.015	<a href="#">Gharaibeh et al. (2011)</a>
[Fe vii]	5722	0.0	> 0.45	98.985 ± 0.015	<a href="#">Gharaibeh et al. (2011)</a>
[Fe vii]	6088	0.0	> 0.45	98.985 ± 0.015	<a href="#">Gharaibeh et al. (2011)</a>
[Fe x]	6376	0.0	> 0.45	233.6 ± 0.4	<a href="#">Sugar &amp; Corliss (1985)</a>
[Fe xi]	7894	0.0	0.24	262.10 ± 0.12	<a href="#">Sugar &amp; Corliss (1985)</a>
[Fe XIV]	5304	0.0	> 0.45	361.0 ± 0.7	<a href="#">Sugar &amp; Corliss (1985)</a>
[Ne v]	3347	0.08	> 0.45	97.1900 ± 0.0025	<a href="#">Kramida et al. (1999)</a>
[Ne v]	3427	0.06	> 0.45	97.1900 ± 0.0025	<a href="#">Kramida et al. (1999)</a>
[Ca xv]	5446	0.0	> 0.45	817.2 ± 0.6	<a href="#">BiÉmont et al. (1999)</a>

Notes: <sup>1</sup> Rest wavelength as used within SLEIPNIR.

<sup>2</sup> Redshift at which the line becomes useful in this analysis, i.e., within the nominal wavelength range and clear of edge effects. Floored at  $z = 0$ .

<sup>3</sup> Redshift at which the line is too close to the edge of the nominal DESI wavelength coverage to be reliably used in this analysis. Ceilinged at the redshift limit of the study  $z = 0.45$

<sup>4</sup> Energy required to produce this ionisation state.

<sup>5</sup> Data were obtained using the National Institute of Standards and Technology (NIST): Atomic Spectra Database ([Kramida & Ralchenko 2024](#)), with references provided to the specific per-line studies.

**Table 5.** Each CrL must pass all of the outlined cuts to be considered ‘detected’.

Description	Values
The central feature region <sup>1</sup> is clear from masked artefacts or spectral gaps	Central feature region contains no NaN values
The peak of a feature must occur within a given threshold of the expected line position	$\pm 350 \text{ kms}^{-1}$
The targeted feature is the strongest emission feature within a region around the expected line position	$\pm 800 \text{ kms}^{-1}$
Central region of a feature must exceed a minimum threshold	Peak scaled flux $> 1.05$
Measured line pEQW must exceed a minimum threshold	$\text{pEQW} < -1.5^2$
The minimum value of feature must be below a minimum threshold	Minimum scaled flux within the central feature region $>= 0.7$
Feature’s peak SNR relative to the local region <sup>3</sup> must exceed a given threshold	Peak relative local SNR within region $>= 3$
Feature’s minimum SNR relative to the local region <sup>4</sup> must exceed a given threshold	Minimum relative local SNR within region $>= -1$
Feature’s minimum SNR relative to the error spectrum must exceed a given threshold	Minimum error spectrum derived SNR $>= 3$

Notes: <sup>1</sup> Central feature region is defined as  $\pm 350 \text{ kms}^{-1}$  of the expected line position.

<sup>2</sup> By convention, emission features are defined with negative pEQWs. This threshold is relaxed by 1 Å for the three weaker [Fe vii] emission lines.

<sup>3</sup> Defined as: Maximum scaled flux in the central feature region / Mean standard deviation of the local continuum regions.

<sup>4</sup> Defined as: Minimum scaled flux in the central feature region / Mean standard deviation of the local continuum regions.

**Table 6.** A list of the telluric emission lines (skylines) identified as most problematic for ECLE identification.

Line	Rest Frame Wavelength (Å)	Source
[Hg I]	4358.34	Light pollution
[O I]	5577.338	Auroral emission
[O I]	6300.304	Auroral emission
OH	7276.405	OH Meinel emission
OH	7630	OH Meinel emission

### 3.2.2 Instrumental architecture

Each telescope and instrument has a unique configuration and architecture that must be considered in its use for transient detection. These factors can include chip gaps across the spectrograph range where individual wavelength regimes will not be sampled (or sampled at lower SNR in composite observations), spectra obtained using multiple spectrographs with differing wavelength coverage which are then combined to produce a single continuous spectrum.

These architectural differences can introduce configuration-specific artefacts into the resulting spectra that can resemble real coronal line features and lead to false positive detections. As with skylines, as these artefacts occur at predictable wavelengths, when

identified they can be mitigated through pre-analysis processing steps on a per-configuration basis.

As described in detail by [DESI Collaboration et al. \(2022\)](#), the DESI instrument system consists of three independent spectra ranges with regions of overlap between each to enable co-addition into continuous spectra. These spectrographs (or arms) are: B; 3600 – 5930Å, R; 5600 – 7720Å, and Z; 7470 – 9800Å. Co-addition of DESI spectra is not handled internally by SLEIPNIR, instead we make use of the co-added files produced by the DESISPEC ([Guy et al. 2023](#)) reduction pipeline directly. Whilst the co-addition performed by the DESISPEC pipeline is robust, residual features within the overlapping regions can be present in the final spectra. These features can resemble narrow emission lines following processing and are most common at the edges and centre of the co-added regions. As previously described with telluric emission features (Section 3.2.1), when these features occur they do so at fixed positions in the observer frame allowing any coincidental alignments with redshifted Fe lines to be identified and such candidates to be discounted as ECLE candidates.

### 3.2.3 Incorrect redshifts

SLEIPNIR relies on accurate external redshifts for proper line identifications. Small discrepancies in redshifts could potentially result

in spectral features moving outside the line detection windows. More significant redshift errors can also result in false-positive detections where unrelated lines are mistakenly placed at the location of the Fe coronal lines in the rest-frame. We will return to this specific source of false positive detection in our discussion of the DESI EDR sample itself in Section 5.

### 3.2.4 Low signal-to-noise

At low SNRs, whether due to operational issues or due to faint sources, noise-related artefacts can remain in the spectra even following processing steps such as smoothing or rebinning. In such cases, if smoothing is too aggressive, strong noise features can be blurred to resemble real spectral features.

These cases can be reduced by applying observed brightness / magnitude cuts to the input spectral samples, though given the random nature of noise contamination, visual inspection remains necessary to remove all such cases from the final object samples. Given the size of the DESI EDR and SLEIPNIR’s false positive rate, these cuts have been set very conservatively (roughly equivalent to predicted source magnitudes of 24.5 in each DESI camera) though would likely need to be raised for larger studies to prevent an unfeasibly high absolute number of false positives during manual inspection.

### 3.2.5 Multiple sources within a single spectrum

Whilst the vast majority of spectra will contain only one source, care must be taken when handling cases where more than one object is in close proximity; in particular when these objects are at differing redshifts. In these cases the blending of the objects produces composite spectra with additional emission features that can align with the expected positions of Fe coronal lines and lead to false positive detections. Visual inspection and object confirmation is required to deal with such cases, as the spectral features responsible for the false detections are real features and thus will look and behave in the same manner as the desired Fe features during spectral processing. One such example was however identified in the previous search of the BOSS LOWZ sample - DESI ID 39628342705525273 / SDSS J2218+2334 is described in depth in [Callow et al. \(2025\)](#). Thankfully, the number of such cases is small, with none directly encountered during the EDR search.

## 3.3 Detection efficiency

We determine the detection efficiency of SLEIPNIR by running it on simulated DESI EDR coronal line galaxy spectra. These were generated by planting coronal lines from known ECLEs into 10,000 random DESI spectra from the sample described in Section 4.1. For each spectrum, the coronal lines from a randomly selected ECLE from the [Wang et al. \(2012\)](#) sample were planted at the wavelengths of the coronal lines. For each simulated spectrum, the strengths of the coronal lines were modified using a scaling factor. This scaling factor was randomly sampled from between 0 and a maximum value set depending on the presence of  $[\text{O III}] \lambda 5007\text{\AA}$  in the base spectrum. If this line was present, then the maximum scaling factor was set such that the strongest coronal line would have the same strength as  $[\text{O III}]$ . If it was not present, the maximum scaling factor was set to 1. This was motivated by the fact that none of the coronal lines in the [Wang et al. \(2012\)](#) ECLEs was stronger than the  $[\text{O III}] \lambda 5007\text{\AA}$  line in the spectra if it was present. SLEIPNIR reaches 50 per cent detection efficiency at an average coronal line strength of  $\sim -1.3 \text{\AA}$ , and has

a maximum efficiency of  $\sim 90$  per cent. Compared to the efficiency of the algorithm on SDSS and BOSS spectra [Callow et al. \(2024, 2025\)](#), it is slightly worse, which is likely due to the overall lower SNR of DESI spectra, though other factors likely also play a role (e.g., differences in galaxy properties between the sample). A comparison of efficiency between the samples is provided in Figure B1.

## 4 SAMPLE CONSTRUCTION AND CLASSIFICATION

In this section we outline the processing of the DESI EDR data and the classification of the spectra to produce our sample of TDEs and other CrL objects. A visual summary of the process is provided in Fig. 1.

### 4.1 Input DESI spectral sample

The DESI survey is composed of multiple survey programs with distinct (though overlapping) targeting criteria. A full description of the DESI targeting selection can be found in [DESI Collaboration et al. \(2024e\)](#) and the references within, whilst a summary of the relevant information for this work now follows.

The three primary DESI surveys for extragalactic targets, in order of increasing average redshift, are the Bright Galaxy Survey (BGS), the Emission Line Galaxies (ELG) sample and the Luminous Red Galaxies (LRG) sample. Additionally, the QSO sample spans a much larger overall redshift range specifically selecting AGNs and QSOs otherwise excluded from the main targeting selections. In addition to these main programs, DESI includes several secondary-target programs with more specific science goals than those of the larger programs. Of particular interest to this work is the *BGS-AGN*. This sample consists of QSOs and other AGN at low-z (distribution peak  $z \sim 0.5$ ) which were rejected by the main BGS survey’s star-galaxy selection criteria, but meet photometric diagnostics indicative of an AGN rather than stellar nature. Objects within this sample have been shown to match the properties of the main DESI-QSO sample, though at significantly lower redshifts ([Juneau et al. 2025](#)). Due to overlapping targeting criteria, an individual galaxy may be selected by multiple programs.

As this work is interested in detecting TDE-ECLEs and other galaxies with coronal line emission (e.g., AGNs with a range of coronal emission lines for comparison purposes), we do not restrict the study to a specific program, though we do preserve each object’s original targeting program(s) for additional analysis. However, given the large number of small secondary programs, we condense these into a single ‘Secondary’ category.

Selection for SLEIPNIR relies on meta information from the DESI spectroscopic pipeline, including the measured spectral redshift measured by the DESI redshift fitter REDROCK and a basic spectroscopic classification of the object as a galaxy rather than a stellar source [Guy et al. \(2023\)](#). The full selection parameters and reasoning are outlined in Table 7.

All criteria must be met for a object to be processed by the primary SLEIPNIR analysis routine. Whilst we do not select spectra from specific observational programs, the upper redshift cut ( $z \leq 0.45$ ) significantly limits the number of spectra selected from the LRG, ELG and QSO samples, for which the peak of the redshift distributions are significantly higher than our upper cut-off. As such, our input sample is dominated numerically by the BGS sample. The upper left panel of Figure 2 is a redshift distribution showing the breakdown of the input sample. Note that a single galaxy can be classified for observation as part of more than one program and as

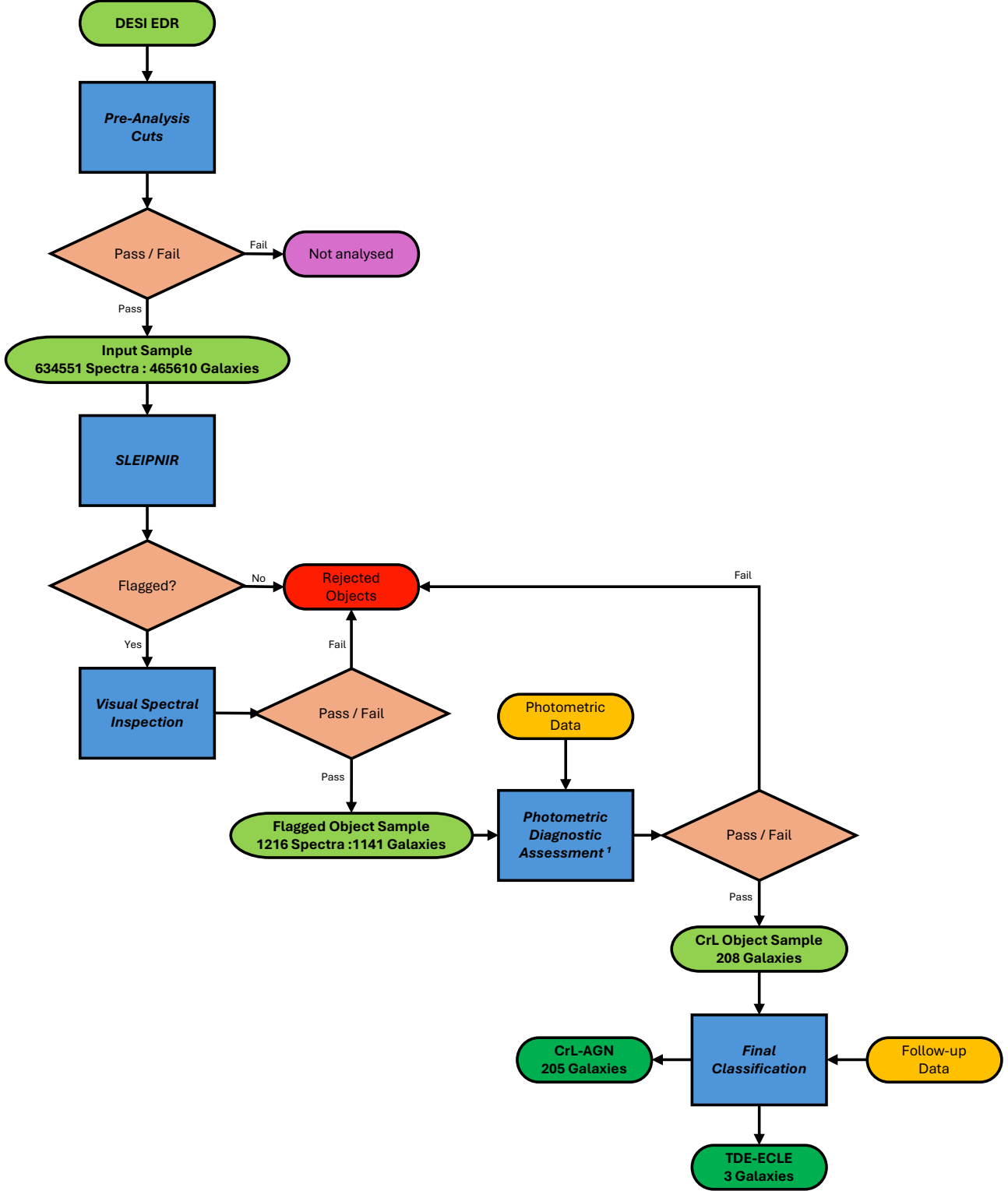


**Figure 1.** Summary of the workflow involved in the processing and classification of the spectra from DESI EDR. Note <sup>1</sup> prior to this point in the workflow, individual spectra are treated independently, following this point all spectra obtained for a single galaxy are used to provide a single classification.

such the full sample redshift distribution is not a simple numeric sum of the individual program redshift distributions. The bottom panel of Figure 2 serves as a summary of this program distribution.

Some objects were observed by DESI multiple times under potentially different observing conditions and for varying effective expo-

sure times. This is a consequence of some objects being located in the footprint of multiple DESI observing ‘Tiles’ (telescope pointings with specific target configurations) and meeting the requirements for observation as part of each. As our initial selection criteria for analysis are primarily based on basic parameters of each galaxy the

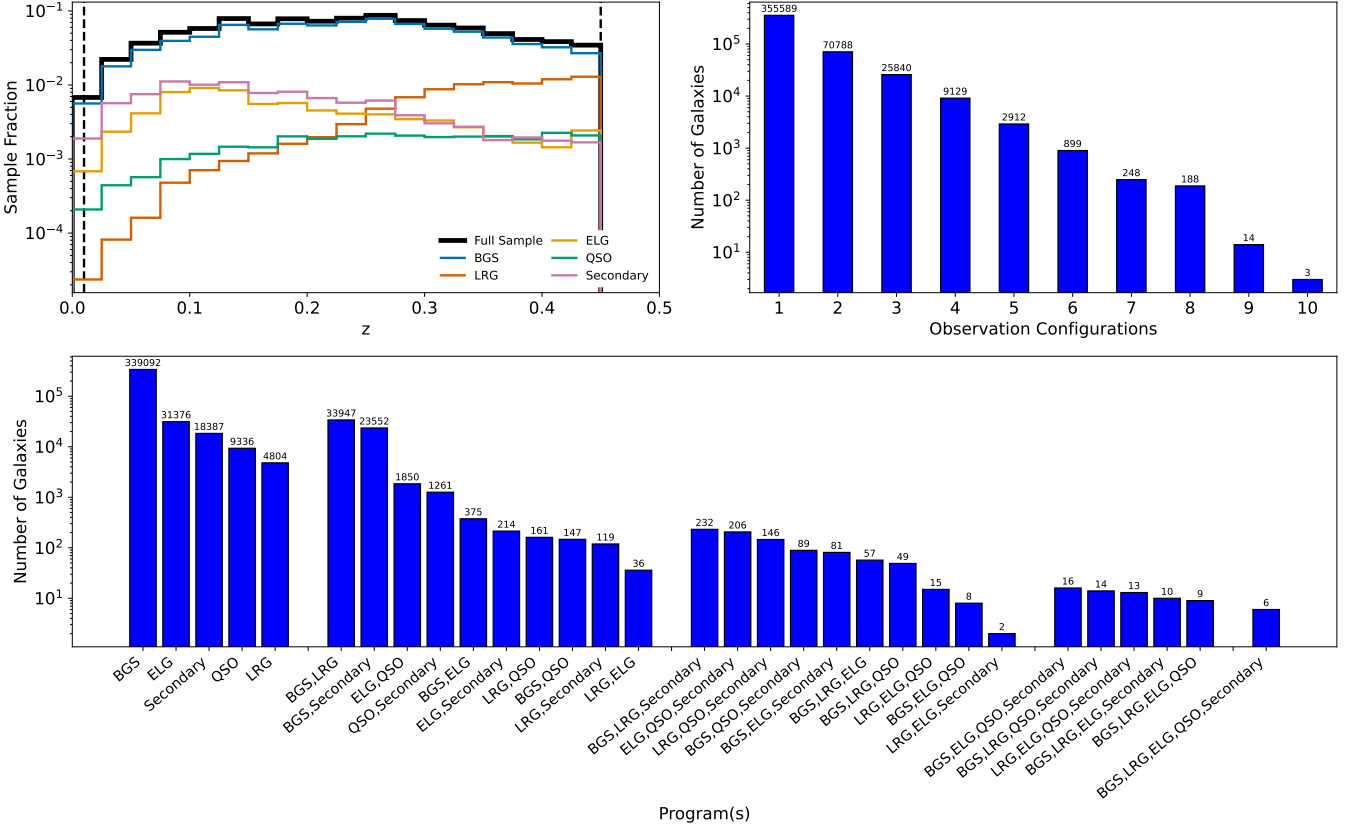


**Figure 2.** *Upper left:* The redshift distribution of the SLEIPNIR input object sample including a per observational program breakdown highlighting the numeric dominance of the DESI-BGS sample. Note: Each targeted galaxy can be included in the selection for more than one program and as such the full sample redshift distribution is not a simple numeric sum of the individual program redshift distributions. BGS selected targets dominate the sample with 85.4% of objects being included in the BGS selection. *Upper right:* Breakdown of the number of observational configurations (and hence spectra) per galaxy in the SLEIPNIR input object. 23.63% of the sample have been observed in multiple configurations. *Bottom:* Breakdown of the DESI observational program distribution of the SLEIPNIR object input sample. 13.44% of the SLEIPNIR input object sample are part of multiple observational programs.

analysis is conducted on a per-tile basis. As such, galaxies that have been observed in multiple tiles will have their spectra processed and analysed independently multiple times. Given the potential for time-variability in the CrL signatures, we do not pre-stack or combine the spectra of objects across different tiles; instead, any galaxy with observations in multiple tiles are compared during the candidate analysis stage. In some cases, an individual tile may be observed more than once if the first observation failed to reach the depth required for the main survey. The data in such cases are combined by the DESI pipeline; the combined data are then fed into SLEIPNIR. As a result of these considerations, the SLEIPNIR galaxy sample explored in this work comprises 465610 unique galaxies. A breakdown showing the number of objects observed with differing numbers of tiles and configurations is given in the upper right panel of Figure 2. As such we define the ‘SLEIPNIR Galaxy Sample’ as the sample of unique galaxies explored by this work (which is comprised of 465610 galaxies).

## 4.2 Sample classification

Of the 465610 unique galaxies in the SLEIPNIR Galaxy Sample, SLEIPNIR flagged a total of 1141 potential candidates - 0.25 per cent of the sample. A breakdown of the flagged candidates based on

the condition upon which they were flagged as a potential candidate is given in Table 8.

All spectra flagged by SLEIPNIR as being a potential ECLE underwent a series of additional analysis and classification steps to both remove false positive identifications (as detailed in Section 3.2) to classify these as being either TDE or AGN-related. The sample is initially cleaned via visual inspection of the flagged spectra. Following this, classification is made through a combination of BPT diagnostics, archival NIR colour-colour classification, MIR photometric analysis, optical photometric analysis, crossmatching with existing databases, and spectroscopic follow-up for the most interesting candidates.

As noted in Section 3.1.4, we do not apply a line strength cut on the CrLs relative to  $[\text{O III}] \lambda 5007\text{\AA}$  emission in this study, and make use of other diagnostics to distinguish between TDEs and AGNs. As such, our definition of ‘ECLE’ is somewhat different from other studies. Furthermore, given the increasing range of CrL strengths observed in AGNs (see e.g., Clark et al. 2024) we do not subdivide our AGN sample further based on line strengths, deferring such analysis to future work. Instead, we divide our CrL object sample simply into TDE and AGN-linked classifications. Figure 3 shows the distribution of candidates across the various flagging criteria and ECLE scores obtained by the initial SLEIPNIR automated flagging compared to the distributions obtained following the removal of all false positive detections.

**Table 7.** Outline of the selection criteria to construct our input spectral sample.

Selection Criterion	Code	Rationale
isTGT	fibermap['OBJTYPE'] == 'TGT'	Removes fibers used for reference sky calibration etc.
isProgram	'Reduced program' contains at least one of: 'BGS', 'LRG', 'ELG', 'QSO', 'Secondary'	Removes identified Milky Way stellar targets
isGal	zbest['SPECTYPE'] in ['GALAXY', 'QSO']	Additional cut to filter potential stellar sources <sup>2</sup>
isGoodFiber	fibermap['COADD_FIBERSTATUS'] == 0	Removes any spectra from fibers with detected issues
isGoodZBest	(zbest['DELTACHI2'] > 25.) & (zbest['ZWARN'] == 0)	Quality cut on determined redshifts
inZRange	0.01 < zbest['Z'] <= 0.45	<sup>3</sup>
hasGFlux, hasRFlux, hasZFlux	fibermap['FLUX_X'] > 0.25	<sup>4</sup>

*Notes:* <sup>1</sup> As TDEs (and thus TDE-ECLEs) occur in a wide range of galaxy types, we do not restrict our initial input sample to galaxies selected by any specific criteria.

<sup>2</sup> Determined by the REDROCK redshift analysis pipeline, where the best fitting spectral template is either a QSO or normal galaxy.

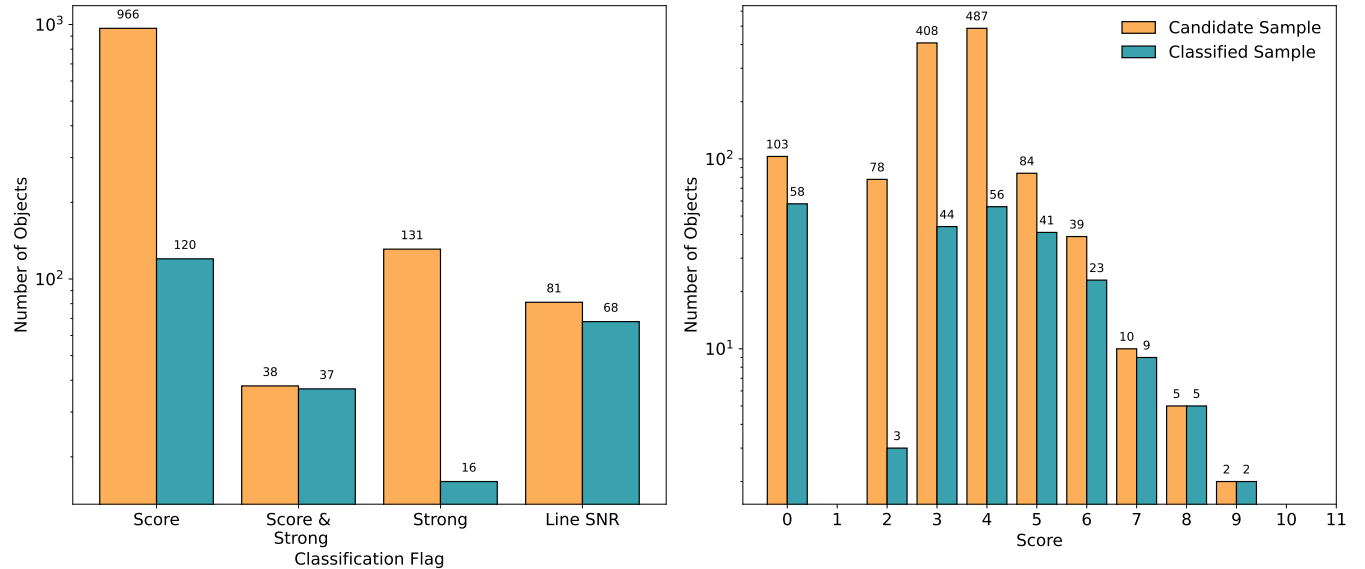
<sup>3</sup> Restricts analysis to objects within a redshift range where H $\alpha$  is within the DESI spectrograph range. Also further removes any remaining galactic sources.

We note here that some classes of source (e.g., QSOs) whose redshift are better measured by specific 'afterburner' codes such as QUASARNET (Green et al. 2025) rather than REDROCK. In this search we make use of REDROCK derived redshifts only. Further searches (in particular at higher redshifts where QSO's are larger component of the sample) will make use of these additional sources of redshift determination.

<sup>4</sup> Cut on the observed brightness of each object as a basic cut on expected signal to noise. Each filter must pass the flux cut (in nanomaggies) corresponding to an approximate magnitude of 24. This is a relaxed cut to initially filter only extremely faint spectra.

**Table 8.** Breakdown of the candidates selected by SLEIPNIR. Values without brackets give the raw breakdown (i.e., per observation with no consideration of duplicates), with those in brackets are for the sample of unique objects.

Flagging Characteristic	Number Flagged		Percentage of SLEIPNIR Input Samples		Percentage of Flagged Samples	
	Spectral Sample	Galaxy Sample	Spectral Sample	Galaxy Sample	Flagged Spectral Sample	Flagged Galaxy Sample
High Scoring	966	928	0.152%	0.199%	79.44%	81.33%
High Scoring & Strong Fe Feature	38	29	0.008%	0.006%	3.13%	2.54%
Strong Fe Feature	131	129	0.021%	0.028%	10.77%	11.31%
FeVII SNR	81	79	0.013%	0.017%	6.66%	6.92%
Any	1216	1141	0.192%	0.245%	-	-
Input Sample Totals	634551	465610	-	-	-	-

**Figure 3.** *Left:* Comparison of the flagging criteria between the number of spectra flagged by SLEIPNIR before and following full classification. The highest fractions of false positives are seen in the those spectra flagged on general score and single strong features. With this being the result of a combination of low SNR, skyline contamination and the effect of single serendipitously located bright artefacts. *Right:* Comparison of the ECLE detection score between the number of spectra flagged by SLEIPNIR before and following full classification. As expected, those objects flagged with lower scores (i.e., fewer confident Fe CrL detections) are more likely to be assessed as false positives.

We compare the redshift and mass distributions of the potential candidates to the overall EDR galaxy sample in Figures 4 and 5. We also include the distributions of the coronal line galaxies detected in SDSS Legacy and BOSS LOWZ (Callow et al. 2024, 2025). Compared to the overall EDR galaxy sample, the candidate galaxies are

under-represented between  $0.11 < z < 0.22$  and over-represented between  $0.28 < z < 0.44$ . The high redshift over-representation is likely due to the fact that [Fe xi]  $\lambda 7894\text{\AA}$  is not within the wavelength range of DESI above  $z \sim 0.3$ , so the threshold for a galaxy to be detected by our algorithm is lowered. Therefore, galaxies with

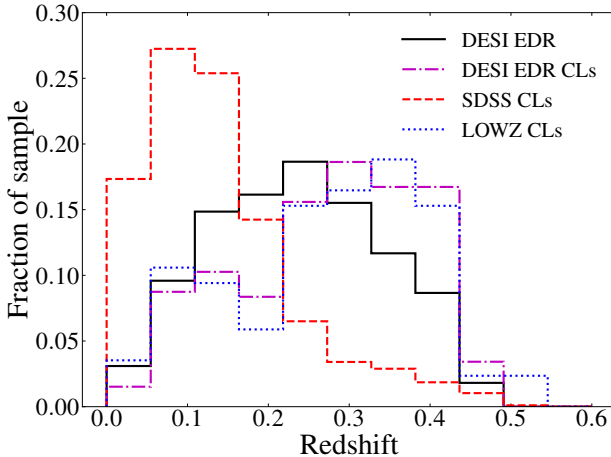


**Figure 4.** Comparison of the redshift distributions of the DESI input sample and the SLEIPNIR flagged sample of candidate coronal line galaxies (solid black and dot-dashed purple curves, respectively). We also include the distributions of the coronal line galaxies selected from searches of SDSS Legacy and BOSS LOWZ galaxy samples (red dashed and blue dotted curves, respectively; Callow et al. 2024, 2025). The EDR coronal line galaxies are under-represented compared to the overall EDR sample between  $0.11 < z < 0.22$  and over-represented between  $0.28 < z < 0.44$ . Note: As in Callow et al. (2025), the comparison BOSS LOWZ sample has been filtered to remove galaxies at the narrow redshift bands most heavily contaminated by skyline emission features at the position of the Fe-CrLs.

fewer coronal lines will be detected more often above this redshift. The under-representation covers a redshift range in which the coronal lines frequently lie at the observed wavelengths of known problematic skylines, so are removed as part of the preprocessing of the spectra. A Kolmogorov-Smirnov test between the EDR overall galaxy and candidate galaxy samples produces a  $p\text{-value} < 0.01$ , meaning we can reject the null hypothesis that these distributions are drawn from the same overall population. Further reinforcing these reasons for the differences between the overall EDR sample and candidate galaxies is the similarity between the EDR and LOWZ coronal-line galaxy distributions. The overall samples cover similar redshift ranges, so the similarities are likely as a result of our detection algorithm.

Comparing the mass distributions of the same samples, we see that the peak of the EDR candidate galaxy sample is slightly lower than that of the overall EDR sample. We also detect very few candidate galaxies with masses below  $10^9 M_\odot$ , similar to the results of the SDSS Legacy search. A reason for this lack of lower-mass galaxies may be that they typically host lower-mass BHs, as accretion on to a SMBH is one of the main processes that can create coronal lines. Lower-mass SMBHs are less able to sustain accretion and therefore produce coronal lines, so we are less likely to detect lower-mass galaxies with coronal lines. We are able to reject the null hypothesis that the EDR galaxy and candidate galaxy samples are drawn from the same population with a Kolmogorov-Smirnov test that gave a  $p\text{-value} < 0.01$ . We remind the reader, that these distributions are constructed from the galaxies satisfying the automatic SLEIPNIR classification criteria and should not be used to determine specifics of the final object samples.

#### 4.3 Sample crossmatching

To further explore our sample and determine if any of the objects within are of special interest (based on existing galaxy classifications

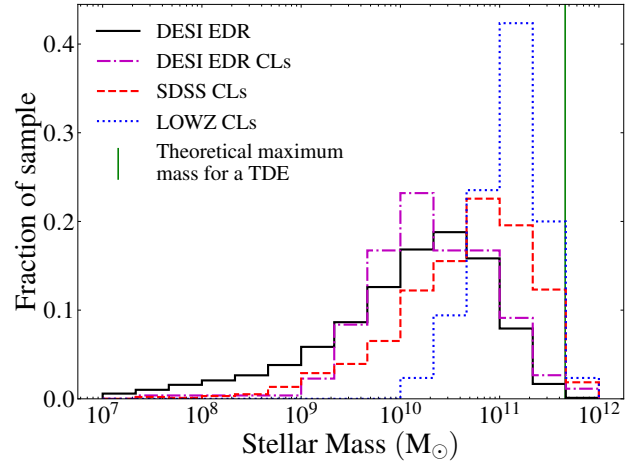


**Figure 5.** Comparison of the mass distributions of the DESI input sample and the SLEIPNIR flagged sample of candidate coronal line galaxies (solid black and dot-dashed purple curves, respectively). We also include the distributions of the coronal line galaxies selected from searches of SDSS Legacy and BOSS LOWZ galaxy samples (red dashed and blue dotted curves, respectively; Callow et al. 2024, 2025). The vertical green line marks the theoretical galaxy stellar mass limit above which a Sun-like star would fall directly into the galaxy’s SMBH instead of being disrupted as a TDE (Rees 1988). The relation between the stellar mass of a galaxy and the mass of its SMBH used in this calculation is from (Reines & Volonteri 2015). The peak of the EDR coronal line galaxy sample is lower than the overall EDR sample, but very few galaxies with masses below  $10^9 M_\odot$  are detected as CrL galaxies.

or transient activity reports) we crossmatch against six catalogues. A breakdown of these crossmatches follows, with a summary provided in Table 9. More detailed breakdown of the results of each crossmatch are included in Appendix C.

##### 4.3.1 Transient Name Server: TNS

The position of each candidate identified by SLEIPNIR is used to query the Transient Name Server (TNS)<sup>7</sup> to identify any potential existing transient connection to our candidate sample. Transient matching is performed using a cone search with a radius of 3 arcseconds. This radius was chosen to be the diameter of the DESI fiber to remain focused on the nuclear regions of galaxies whilst allowing some tolerance for the presence of transients some distance from the nucleus.

These crossmatches identified 1219 galaxies within the SLEIPNIR Input Galaxy Sample hosting at least one TNS recorded transient (outlined in Table C1). Of these, 6 galaxies are within the SLEIPNIR CrL Object Sample (as outlined in Table 10), though none of the corresponding TNS transients have been independently classified.

##### 4.3.2 TDE literature search crossmatch

In addition to a general search of the TNS we conduct an additional search of objects compiled from the literature that have been identified as TDEs or related phenomena that have not necessarily been reported to the TNS.

Our database of literature objects for this crossmatching includes all objects classified as TDEs on the TNS (for general completeness), the original ECLE sample from Wang et al. (2012), the IR-TDE sample from Masterson et al. (2024), the TDE sample compiled by

<sup>7</sup> <https://www.wis-tns.org/>

**Table 9.** Results summary for the crossmatch searches conducted between the DESI EDR ECLE candidate sample numerous catalogues as described in the text.

Crossmatch Source	SLEIPNIR Galaxy Sample <sup>1</sup>		Final CrL Object Sample <sup>2</sup>	
	Matches	Percentage Matched	Matches	Percentage Matched
TNS Classified Sources <sup>3</sup>	1219	0.262%	6	2.885%
Literature Derived TDE Candidate Catalogue <sup>4</sup>	11	0.002%	0	0.000%
SDSS Legacy CrL Sample <sup>5</sup>	18	0.004%	5	2.404%
BOSS LOWZ CrL Sample <sup>6</sup>	7	0.002%	0	0.000%
MILLIQUAS <sup>7</sup>	7154	1.536%	163	78.365%
Ding et al. 2025 <sup>8</sup>	47	0.010%	19	9.135%

Notes: <sup>1</sup> This sample consists of the 465610 unique galaxies present within the initial sample processed by SLEIPNIR.

<sup>2</sup> This sample consists of the 208 unique objects identified as displaying real coronal lines following processing by SLEIPNIR and manual inspection and confirmation.

<sup>3</sup> Crossmatch performed on the full TNS database as of 2025 August 28.

<sup>4</sup> See Section 4.3.2 for details.

<sup>5</sup> Consists of the SLEIPNIR flagged objects from the SDSS Legacy Survey DR17 as detailed in Callow et al. (2024).

<sup>6</sup> Consists of the SLEIPNIR flagged objects from the BOSS LOWZ sampled as detailed in Callow et al. (2025).

<sup>7</sup> Utilises v8 of the Million Quasars (MILLIQUAS) catalogue, consisting of 1021800 individually identified AGN from a range of sources see Flesch (2023) for details.

<sup>8</sup> Sourced from the independent search of ECLEs in DESI EDR detailed in Ding et al. (2025).

**Table 10.** Results of the crossmatch search between the SLEIPNIR CrL Object Sample and objects recorded in the full TNS database as of 2025 August 28.

DESI ID	CrL Classification <sup>1</sup>	TNS Name	TNS Classification
39628506220463012	CrL-AGN	AT 2018mer	None
39633304189666247	CrL-AGN	AT 2019jw	None
39633300653869008	CrL-AGN	AT 2021lar	None
39627782338120416	CrL-AGN	AT 2021mks	None
39633453855017885	CrL-AGN	AT 2021vje	None
39627758191511075 <sup>2</sup>	CrL-AGN	AT 2025ils	None

Notes: <sup>1</sup> Classification of the source of the CrLs observed in this source made by this work.

<sup>2</sup> This transient is linked to a CrL-AGN identified as having broad CrL emission and discussed in Appendix D.

Qin et al. (2022), *e*ROSITA X-ray selected TDEs from Sazonov et al. (2021), Grotova et al. (2025) and Eyles-Ferris et al. (2025). Also included in this cross-match are those Mid-infrared Outbursts in Nearby Galaxies (MIRONGs) identified by Jiang et al. (2021a) and interpreted by Wang et al. (2022) as being likely TDEs (noting that the MIRONG sample as a whole is likely dominated by AGNs; Dodd et al. 2023), with additional archival TDEs. In addition to objects with well established TDE classifications, we also include those which may have a TDE-linked origin, including the samples of ambiguous nuclear transients (ANTs) from Hinkle (2024) and Wiseman et al. (2025), as well as the quasiperiodic eruptions (QPEs) collated by Jiang & Pan (2025). In total this database currently consists of 370 verified TDEs, TDE candidates and other related nuclear transients. Given the developing nature of nuclear transient classification, this database of comparison objects is not intended to be a pure sample of conventional TDEs, rather serving as a reference for all non-AGN-related nuclear transients.

This crossmatch identifies 11 transients with spectra in the full SLEIPNIR Input Galaxy Sample, as summarised in Table C2. As none of these DESI spectra passed the cuts for initial visual inspection (i.e., SLEIPNIR did not identify them as potential ECLEs), all individual spectra of these galaxies were manually inspected following the crossmatch and confirmed to be absent of coronal lines. A more in-depth study of TDE host galaxies observed by DESI is planned but goes beyond the scope of this current work.

#### 4.3.3 SDSS crossmatches

We also perform crossmatch searches between the SLEIPNIR Input Galaxy Sample and the samples of galaxies returned as ECLE candidates by earlier versions of SLEIPNIR when analysing the SDSS samples described in Callow et al. (2024, 2025). Crossmatches were performed against the raw forms of these SDSS samples (i.e., all objects flagged by SLEIPNIR including those later identified as false positives) for sample validation purposes. We note that the DESI spectra used in the analysis of the ECLEs identified in Callow et al. (2024, 2025) were obtained after the DESI EDR and are thus not part of the SLEIPNIR Input Galaxy Sample.

The crossmatch of the SLEIPNIR Input Galaxy Sample to the SDSS Legacy DR17 sample from Callow et al. (2024) returned 18 objects, of which five are within the EDR CrL Object Sample. All five of the objects within the EDR CrL Object Sample have been classified as CrL-AGN prior to the crossmatch. The crossmatch of the SLEIPNIR Input Galaxy Sample to the BOSS LOWZ CrL sample from Callow et al. (2025) returned seven objects, none of which are included in the EDR CrL Object Sample. The full results of these crossmatches are summarised in Appendix C3.

#### 4.3.4 MILLIQUAS crossmatch

Our penultimate crossmatch compared the SLEIPNIR Input Galaxy Sample to the eight version of the Million Quasars (MILLIQUAS) catalogue (Flesch 2023), with the goal of further supporting or ruling out AGN classification of galaxies displaying coronal lines. We note here that as the MILLIQUAS catalogue includes classifications

making use of DESI spectral data, it is not a fully independent AGN classification source in all cases.

Given the relative abundance of AGNs and the presence of coronal line AGNs, it is unsurprising that this crossmatch generated the most matches, with 7154 galaxies in the SLEIPNIR Input Galaxy Sample also present in the MILLIQUAS catalogue, 163 of these within the Final CrL Object Sample. Of the latter, all were classified as CrL-AGNs.

In addition to these galaxies, 55 additional crossmatched AGNs were flagged by SLEIPNIR as potential ECLEs but discarded as false positives that do not display real CrL emission features at various stages of the classification process. These false positive identifications were the result of skyline contamination and other artefacts producing serendipitous features strong enough to flag the spectrum for inspection.

#### 4.3.5 Ding et al. (2025) crossmatch

A recently published independent search for ECLEs in DESI EDR by Ding et al. (2025) identified 84 CrL galaxies which they classified as non-AGN hosts based on BPT diagnostics. Key differences between the Ding et al. (2025) analysis and the analysis presented in this work include:

- There is no upper redshift cut on the Ding et al. (2025) sample, compared to the limit of  $z < 0.45$  employed here.
- The Ding et al. (2025) sample applies a line strength cut according to which at least one CrL must exceed 20 per cent the strength of  $[\text{O III}] \lambda 5007\text{\AA}$  to remove AGN.
- The presence of  $[\text{Ne V}] \lambda 3347\text{\AA}$  and  $[\text{Ne V}] \lambda 3427\text{\AA}$  are included as object selection criteria for the Ding et al. (2025) sample but are not included here.
- Unlike the multi-wavelength approach adopted here, Ding et al. (2025) classify their candidates based almost exclusively on the DESI EDR spectrum (in combination with a limited number of archival SDSS spectra).
- An object can be selected as an ECLE in the Ding et al. (2025) sample based purely on the presence of one emission line (e.g.,  $[\text{Fe XIV}] \lambda 5304\text{\AA}$ ) regardless of whether or not other lower ionisation state lines are present. In our analysis, while such objects could be flagged based on the ‘Strong CrL’ criterion by SLEIPNIR and visually inspected, such objects would be rejected as unphysical artefacts if they lack any other Fe CrLs.

When a redshift cut of  $z = 0.45$  is applied to the Ding et al. (2025) sample to match that of our SLEIPNIR-based analysis, 47 potential shared objects are obtained, all of which were manually reinspected by us. Of these, 19 were flagged by SLEIPNIR as potential ECLEs. From this subsample, five were rejected as being artefacts due to residual skylines or instrumental effects. This includes DESI J179.8036-00.5238 which was reported by Ding et al. (2025) as showing  $[\text{Fe VII}] \lambda 6088\text{\AA}$  in the DESI EDR spectrum but not in an archival SDSS observation, indicating potential transient activity. Following reinspection of the EDR spectrum, no other  $[\text{Fe VII}]$  emission line is observed (nor are any higher ionisation state lines). No indications of either TDE or AGN activity are observed in the object’s optical or MIR photometry. Additionally, the  $[\text{Fe VII}]$  feature is not present in the DESI DR1 (DESI Collaboration et al. 2025a) spectrum of the same galaxy, which used a different version of the DESI reduction pipeline. As such, we conclude that the apparent  $[\text{Fe VII}] \lambda 6088\text{\AA}$  emission feature is an artefact and not an indication of CrL emission, TDE-related or otherwise. The remaining 19 objects within the sub-sample were found to show real CrL emission

in this work but were identified as being the result of AGN activity following our classification process.

Of the remaining 23 candidates, three objects failed the initial selection for inclusion within the SLEIPNIR sample, with inspection of these revealing the apparent  $[\text{Fe VII}]$  detections to be artefacts due to either skylines or reduction issues. The 20 remaining shared objects were included in the SLEIPNIR input sample but were not flagged as ECLE candidates for human inspection. This is the result of either their inclusion in the Ding et al. (2025) sample being exclusively due to the presence of  $[\text{Ne V}]$  emission - which is not a selection criterion for SLEIPNIR - or because the Fe CrL emission in the spectrum was rejected due to SLEIPNIR’s line selections indicating the feature as erroneous. Manual inspection of these spectra confirms these assessments. Due to the outlined issues with sample construction, the Ding et al. (2025) analysis and its conclusions should be interpreted with care.

However, we note that galaxies displaying  $[\text{Ne V}]$  emission lines but no (or extremely weak)  $[\text{Fe VII}]$  emission features (e.g., DESI J172.1834+51.8532 / DESI spectroscopic ID: 39633274758236748) are of interest for further study. Given the very similar energy requirements to produce the two ions (see Table 4), these lines would be expected to occur together. The lack of  $[\text{Fe VII}]$  emission features in galaxies displaying  $[\text{Ne V}]$  offers a potentially sensitive diagnostic of the strength of the X-ray ionisation continuum in such galaxies.

## 5 DESI EDR ECLES

Following our multi-stage classification, our sample of galaxies displaying verified CrLs in their EDR spectra consists of 208 individual objects. We first focus on the three objects we ultimately classify as being linked to TDEs (Section 5.1), before discussing six additional objects that were identified during our analysis as initially being ambiguous during their classification as either TDE or AGN-related, though are ultimately classified as AGN activity or other contaminants (Section 5.2).

We give summary information for all of these objects in Table 11, along with providing contextual  $grz$  optical imaging from the DESI Legacy Surveys for each in Fig. 6, their MIR evolution in Fig. 7 and archival NIR colour information in Fig. 8. We note here that the DESI spectra used in the follow-up analysis of the original Wang et al. (2012) ECLE sample as part of Clark et al. (2024) were obtained following the cut-off for inclusion in EDR and are thus not part of our EDR sample.

### 5.1 TDE-linked candidates

#### 5.1.1 DESI 39627794400938039 : Pidgeot

Pidgeot was identified by SLEIPNIR as an ECLE candidate through a combination of multiple Fe CrL detections ( $[\text{Fe VII}]$  and  $[\text{Fe X}]$ ) and a high SNR  $[\text{Fe VII}] \lambda 5722\text{\AA}$  line detection.

Pidgeot was observed in two DESI tiles (298 and 310) with both observations meeting the SLEIPNIR flagging criteria, though only the tile 298 spectrum satisfying the high SNR  $[\text{Fe VII}] \lambda 5722\text{\AA}$  line requirements. We note that whilst the  $[\text{Fe VII}] \lambda 6088\text{\AA}$  line is close to a problematic skyline, its peak is sufficiently separated to provide a conclusive detection - supported by the clear and unambiguous presence of other  $[\text{Fe VII}]$  emission lines.  $[\text{Fe X}] \lambda 6376\text{\AA}$  is close to the centre of the overlap region of the  $r$  and  $z$  cameras, whilst also being affected by telluric absorption and other line contamination, affecting

**Table 11.** EDR TDE Candidate Information

DESI Target ID	Internal Name <sup>1</sup>	RA	DEC	$z$ <sup>2</sup>	$z$ err	EBV
<b>TDE-Linked Candidates</b>						
39633332819985805	Pidgeot	243.37986	55.75283	0.193	$3.62 \times 10^{-6}$	0.008
39627794400938039	Raticate	216.58918	0.14369	0.115	$9.62 \times 10^{-6}$	0.033
39627884763023878	Raichu	204.39900	3.87760	0.057	$1.37 \times 10^{-6}$	0.026
<b>AGN-Linked Candidates</b>						
39627700695996439	Venusaur	30.46915	-3.58470	0.160	$3.37 \times 10^{-6}$	0.026
39627887837451274	Charizard	27.95254	4.19518	0.079	$4.20 \times 10^{-6}$	0.037
39633118667214268	Fearow	236.47605	42.29324	0.152 <sup>3</sup>	$2.90 \times 10^{-5}$	0.031
39633066745924399	Arbok	115.57303	39.43668	0.416	$1.21 \times 10^{-5}$	0.056
39633255741260888	Sandslash	172.66753	50.61793	0.058	$1.29 \times 10^{-6}$	0.013
39633290029695741	Nidoqueen	212.95561	52.76762	0.074	$6.67 \times 10^{-6}$	0.010

*Notes:* <sup>1</sup> To prevent confusion between objects with similar DESI target IDs, each promising candidate was assigned an internal name derived from the popular Pokémon media franchise. We refer to the objects by these internal names within the following text and plots for conciseness.

<sup>2</sup> Redshift as determined by the REDROCK pipeline.

<sup>3</sup> Erroneous determination, true redshift is  $\sim 3.928$ . See Section 5.2.3 for details.

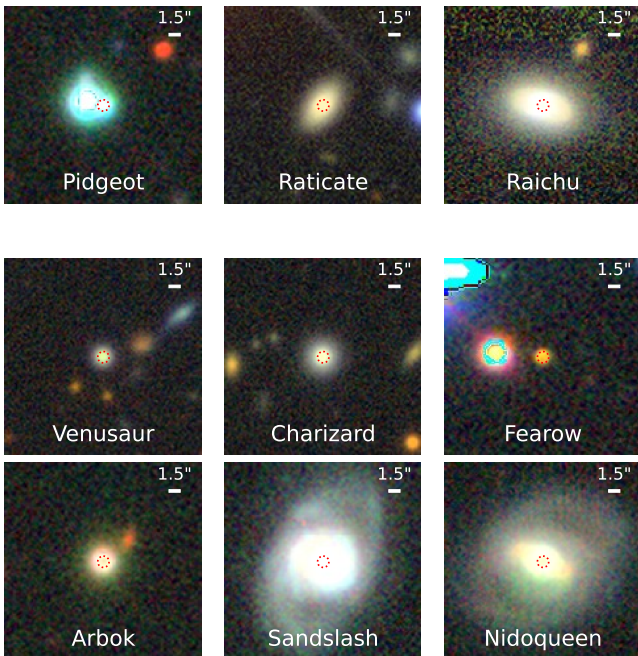


**Figure 6.** DESI Legacy Survey  $grz$  composite images of each of the EDR ECLE candidates. *Top row:* Candidates identified as being TDE-related following full classification. *Lower rows:* Candidates identified as being AGN-related following full classification. Dashed circle indicates the location of the DESI fibre used to obtain each object’s spectrum.

the quality of its line profile and making a definitive detection of this line impossible. Pidgeot is located on a line of sight close to an unrelated foreground Milky Way star (see Figure 6) confirmed to be unrelated both an additional Keck+LRIS spectrum obtained at the same time as our primary follow-up. As both DESI spectra of Pidgeot were obtained just four days apart, we use the higher SNR spectrum for our analysis.

We obtained optical follow-up spectra of Pidgeot with both NOT+ALFOSC and Keck+LRIS as shown in Figure 9. The Keck spectrum has a significantly higher SNR, but both follow-up spectra show a reduction in the relative line strengths of both the  $[\text{Fe VII}] \lambda 5722\text{\AA}$  and  $[\text{Fe VII}] \lambda 6088\text{\AA}$  lines, accompanied by a re-

duction in the strength of the  $[\text{Ne V}] \lambda 3427\text{\AA}$  line of very similar ionisation energy. Additionally, the Keck+LRIS spectrum indicates an increase in  $[\text{O III}]$  and  $[\text{Ne III}] \lambda 3869\text{\AA}$  emission, similar to the behaviour observed in other TDE linked CrL galaxies (e.g., Clark et al. 2024, 2025).

2MASS NIR photometry does not indicate the presence of an AGN, nor is Pidgeot present within the MILLIQUAS database. However, emission line diagnostics from the spectra indicate Seyfert-like activity, including the presence of broad components to both the  $\text{H}\alpha$  and  $\text{H}\beta$  features, which are also present throughout follow-up observations (see the bottom row of Fig. 9). These BPT diagnostics (along with those reported for the other candidates) are not based on the initial automated measurements performed by SLEIPNIR during initial analysis, and instead reflect measurements made following emission line fitting using the Image Reduction and Analysis Facility (IRAF) Splot routine (Tody 1986, 1993; Fitzpatrick et al. 2024).

ZTF optical photometry (whilst limited) does not show the presence of any outburst behaviour, nor do our LT observations display significant evolution. ATLAS forced photometry does show a potential outburst in the *cyan* band close to the start of the survey (from survey start until MJD 58000) though this is not matched by a corresponding outburst in the *orange* band, which instead shows erratic negative difference flux relative to the baseline. We thus attribute this ‘activity’ to observational artifacts near the start of the survey.

The MIR behaviour of Pidgeot is the most interesting aspect of its evolution (Figs. 27 and 7). AllWISE colour diagnostics classify it as a spiral galaxy that does not host an AGN. NEOWISE-R data indicate the galaxy is a non-AGN host that displayed a significant TDE-like MIR outburst, starting between MJD 57042 and 57215, reaching a peak at  $\sim$  MJD 57575. We note that the star in close proximity to Pidgeot will affect the underlying measurements through overlapping PSFs at the resolution of WISE. However the observed outburst can conclusively be linked to the host galaxy of Pidgeot through inspection of the measured centroid position of the source which moves to the position of Pidgeot’s host galaxy during the outburst before drifting back to between both objects as the outburst fades. Additionally, as noted, the AllWISE colour-colour diagnostics are indicative of a starforming galaxy rather than a stellar source.

Whilst CrL-TDE outbursts that are superficially very similar have been seen in the past (e.g., AT 2017gge and AT 2018dyk among others; Clark et al. 2025), the overall evolution of Pidgeot is more complex. In previously studied transients, where the quiescent behaviour was observed both pre and post outburst, the brightness and

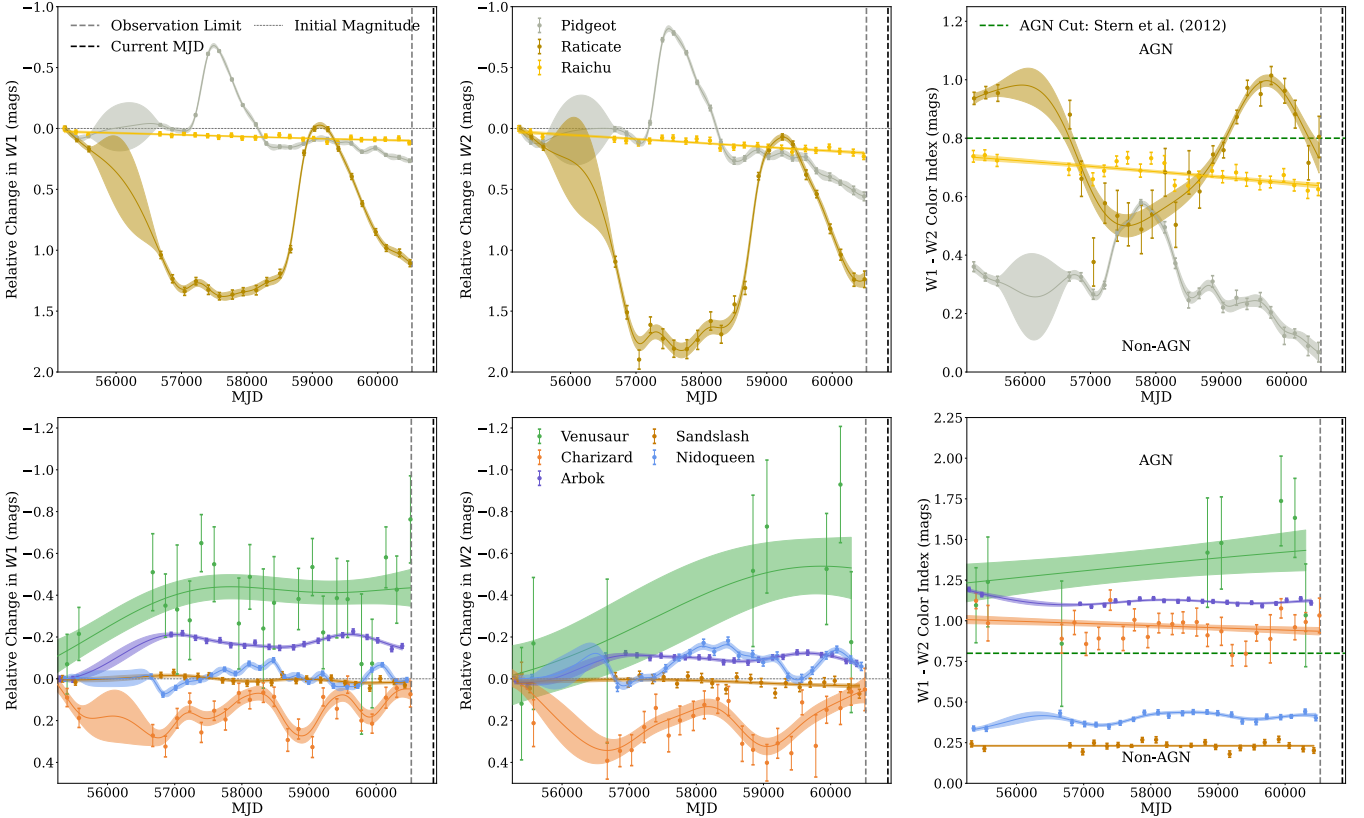


**Figure 7.** MIR evolution of the EDR-ECLE candidates. *Top row*: Candidates linked to TDE activity following full classification. *Bottom row*: Candidates linked to AGN activity following full classification. *Left panels*: Relative change in  $W1$  compared to observed  $W1$  peak. *Middle panels*: Relative change in  $W2$  compared to observed  $W2$  peak. *Right panels*:  $W1$ – $W2$  colour evolution. The dashed horizontal line shown is the AGN/non-AGN dividing line from Stern et al. (2012). Colours above this line are typical of AGN. In all panels, fits displayed are obtained through Gaussian processes, with shaded regions indicating the  $1\sigma$  fitting uncertainties.

colours match in both phases (see AT 2018dyk and AT 2019azh in fig. 7 of Clark et al. 2025). We note the limited number of objects for which this assessment is possible due to the lifespan of the WISE spacecraft and the multi-year durations of the majority of these outbursts. This is not the case in Pidgeot, with the post-flare quiescent  $W1$  state observed to be approximately 0.4 mag dimmer than the pre-outburst quiescent state. Additionally, the  $W2$  luminosity displayed a 1300-day-long plateau (MJD 58300–59600) before declining an additional  $\sim 0.2$  mags until the most recent observations. The colour of Pidgeot has also continued to trend blueward following the outburst (where it displayed the usual reddening behaviour typical of TDE MIR outbursts Clark et al. 2025) with it now being  $\sim 0.2$  mag bluer in the WISE bands than pre-outburst.

This may be the result of the TDE responsible for the outburst occurring in a galaxy already displaying long-term variability, specifically a galaxy displaying a long-term reduction in MIR luminosity whilst trending towards bluer MIR colours. Alternatively, this long term decline may also be at least partially due to the contamination of the observations with flux from the nearby star. We will return to the MIR evolution of Pidgeot in Section 6.1 to place it in context with the existing nuclear transient population.

Pidgeot is within the sky-coverage region of LoTSS-DR2, and is not associated with a radio source in any of the radio surveys examined in this work, ruling out radio-loud AGN activity. We conclude

that Pidgeot is best explained as a TDE with a significant MIR outburst, likely occurring within a gas-rich environment.

### 5.1.2 DESI 39627794400938039 : Raticate

Raticate was identified by SLEIPNIR as an ECLE candidate by the presence of a high SNR  $[\text{Fe}\,\text{xi}]$  feature, along with the detection of  $[\text{Fe}\,\text{x}]$ . Visual inspection confirmed these features, as well as the presence of weak  $[\text{Fe}\,\text{vii}]$  lines that did not meet the automatic pEQW detection threshold.

Skyline contamination near the  $[\text{O}\,\text{iii}] \lambda 5007\text{\AA}$  line affected the automatic emission line diagnostic determination. Inspection of this line region indicates that whilst the blue wing of the feature may be somewhat contaminated, the central core is sufficiently separated from the skyline position in the DESI spectrum to confirm the lack of particularly strong  $[\text{O}\,\text{iii}] \lambda 5007\text{\AA}$  emission – further supported by the strength of the uncontaminated  $[\text{O}\,\text{iii}] \lambda 4959\text{\AA}$  emission feature. These emission-line properties disfavour the presence of a significant AGN in Raticate’s host galaxy, a statement further supported by this galaxy’s absence within the MILLIQUAS AGN database. However, we note that the BPT diagnostics measured from the DESI spectrum indicate Seyfert-like activity driven by the weakness of the  $\text{H}\beta$  emission. Our follow-up spectra, whilst unable to provide additional BPT diagnostic measurements due to a lack of  $\text{H}\beta$  emission detection (and a slight wavelength calibration issue with the

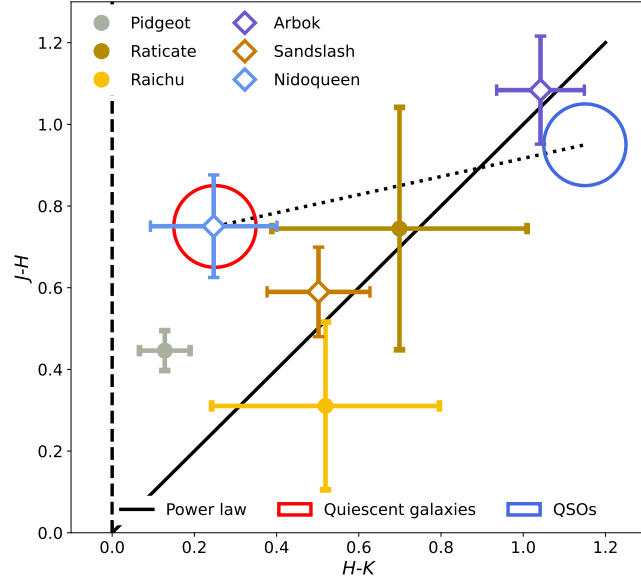


**Figure 8.** 2MASS photometric diagnostic plot for the DESI EDR TDE-ECLE candidates. Filled markers indicate candidates linked to TDEs following overall classification. Hollow markers indicate candidates which have been ruled out as being TDE linked following overall classification. NIR classification based on Hyland & Allen (1982) and Komossa et al. (2009). As described by Clark et al. (2024), whilst NIR classification is a useful assistive diagnostic, given both the time difference between the NIR observations and the wide range of colours displayed by galaxies of the same optical spectroscopic classification, it cannot be used to identify TDE-related activity on its own. The candidates Venusaur, Charizard and Fearow are not included as they were not detected in the 2MASS survey.

NOT+ALFOSC spectrum), do show the complete fading of [Fe x] and [Fe xi] emission and a reduction in [Fe vii], suggesting transient activity.

Photometrically, no transients were reported close to Raticate's position, and the host galaxy displayed no optical outbursts prior to the DESI observation. Pre-outburst, NIR photometry from 2MASS is too uncertain to provide clear classification.

MIR photometry from AllWISE indicates Seyfert AGN-like MIR colours, though the most interesting aspect of Raticate's behaviour is seen in the NEOWISE-R dataset, where two distinct MIR outbursts are observed. The first was in its active state during the AllWISE observations (seen in both the  $W1$  and  $W2$  light curves bands and in the AGN-like  $W1-W2$  colour), though the start and true peak of this outburst occurred prior to the start of observations. Raticate then faded between the AllWISE and NEOWISE-R surveys, reaching apparent quiescence at  $MJD \sim 57000$  with an accompanying shift to a bluer  $W1-W2$  colour. This low state persisted until  $MJD \sim 58000$ , with brightening and reddening then seen with a significant outburst at  $MJD \sim 58750$  reaching a luminosity peak at  $MJD \sim 59250$  and a delayed peak redness at  $MJD \sim 59750$ . The MIR light curve then declined towards the previous quiescent state.

Possible explanations for this MIR behaviour include the occurrence of two distinct TDEs, each responsible for one of the outbursts; a repeating partial TDE; or an AGN repeatedly switching on and off. Additionally, whilst Raticate is not within the sky-coverage region of LoTSS-DR2, it is not associated with a radio source in either VLA-FIRST or VLASS indicating a lack of radio-loud AGN activity. We investigate the MIR outburst behaviour and compare to other

nuclear transients in Section 6.1. For the purposes of this analysis, we conclude that Raticate is the result of the occurrence of at least one TDE.

### 5.1.3 DESI 39627884763023878 : Raichu

Raichu was identified by SLEIPNIR as an ECLE candidate based on the weak presence of [Fe vii] lines. Visual inspection of the spectrum also shows the presence of a weak [Fe x] feature and a potential [Fe xi] feature (though contaminated by skyline emission). Optical emission line diagnostics indicate the presence of a narrow-line AGN (in particular strong [O iii] lines are present). Prior NIR photometry from the 2MASS survey provides an unclear classification based on the classification scheme of Hyland & Allen (1982) (see Figure 8). Optical photometry from ATLAS and ZTF shows stable fluxes over the course of observations without indication of TDE-like outbursts or AGN-like photometric variability.

Raichu is not present within the MILLIQUAS AGN catalogue, with AllWISE  $W1-W2$  vs  $W2-W3$  photometry obtained years prior to the DESI spectrum showing that the galaxy did not meet the AGN classification criteria of either Stern et al. (2012) or Mateos et al. (2012), though it occupies a somewhat ambiguous region of parameter space per the Wright et al. (2010) colour diagnostics, including both AGN and non-AGN galaxies (see Fig. 27). Raichu is not within the sky-coverage region of LoTSS-DR2 and is not associated with a catalogued source in either VLA-FIRST or VLASS. As described in Section 2.4.1, a possible faint source is visually observable at its location in the VLA-FIRST cutout image. This source is of similar strength to other spurious noise features in the cutout, which in combination with Raichu's non-detection in alter VLASS radio observations lead us to conclude that radio-loud AGN activity is not present.

Most interestingly, Raichu displays a long-term decline in both the  $W1$  and  $W2$  bands, with an associated blueward trend in its  $W1-W2$  colour, moving further from the red colour indices associated with AGN activity. Such behaviour has previously been observed in TDE-ECLEs (Clark et al. 2024). We further explore this behaviour in Section 6.1.

Additionally, strong [O iii] emission (and the accompanying BPT diagnostics) more typically seen in AGNs has been observed in several other TDE-ECLEs and CrL-TDEs at late-times, including SDSS J134244.41+053056.1 (Clark et al. 2024) and AT 2018dyk (Clark et al. 2025). The development of these features in such objects is explained by the delayed response of material at greater distances from the SMBH. Whilst our follow-up spectra do not show significant alterations in [O iii] emission strength compared to the DESI spectrum. Variation is observed around the  $H\alpha$  complex, though this may be the result of the spectra probing somewhat different regions of the host galaxy (which is observed to be non-spherically symmetric, see Fig. 6). Fe emission remains unchanged between the DESI and follow-up spectra. However, the uncertain timescales involved preclude this from being used to disfavour a TDE interpretation with other TDE-ECLEs also known to display CrL emission for years during extended MIR declines (Clark et al. 2024). We conclude that Raichu is best explained as a TDE-ECLE, where the originating TDE occurred well before the start of available optical and MIR observations.

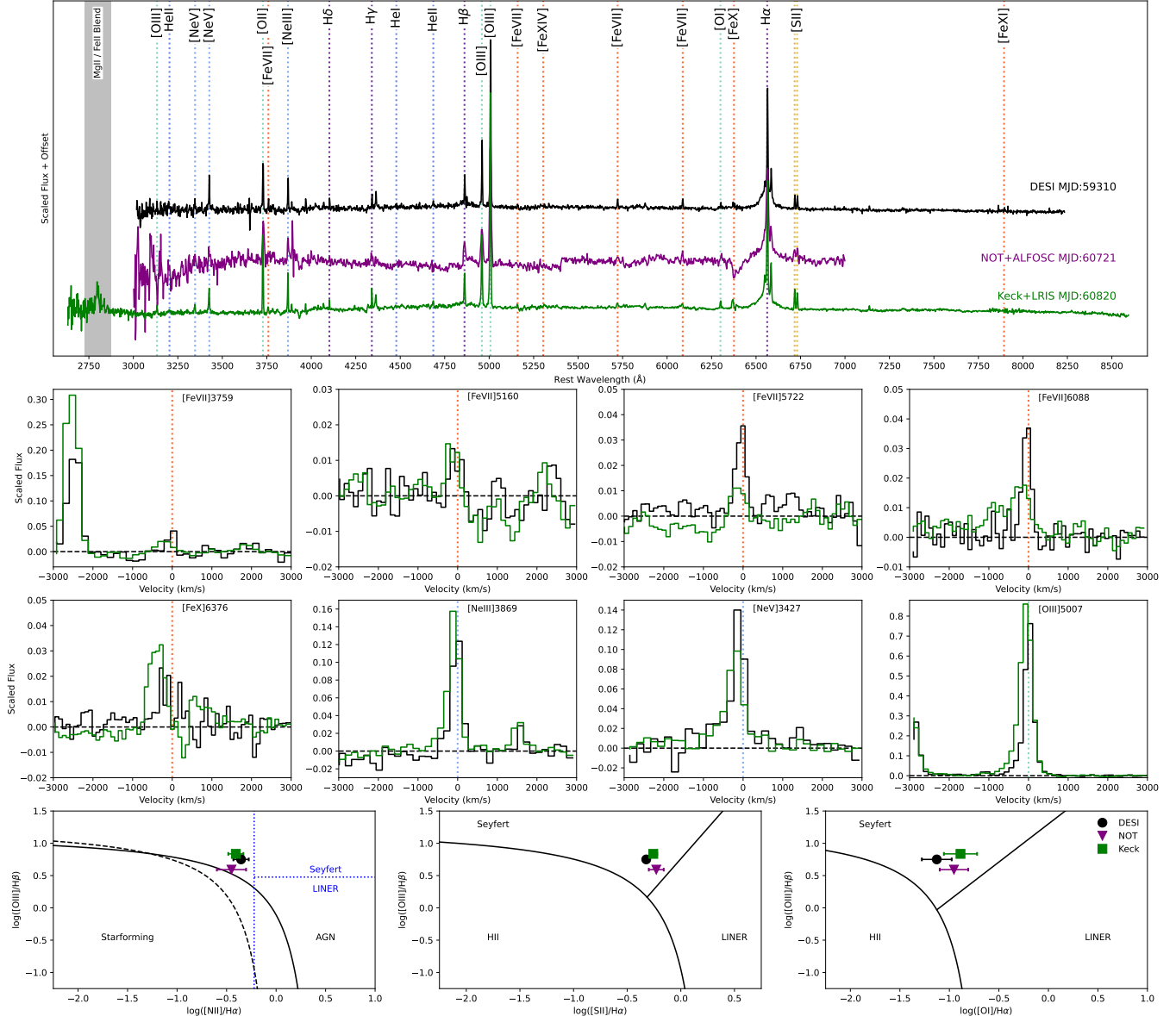


**Figure 9.** In all panels spectra have been rebinned to a shared 2 Å wavelength regime, but have not otherwise been smoothed. *Top row:* Spectral evolution of Pidgeot. *Second and third rows:* Comparison between the spectral features of most interest between the DESI and Keck+LRIS spectra. Clear reductions in [Fe vii]  $\lambda 5722\text{\AA}$ , [Fe vii]  $\lambda 6088\text{\AA}$  and [Ne v]  $\lambda 3427\text{\AA}$  line strength are observed, in contrast to increasing [O iii]  $\lambda 5007\text{\AA}$  and [Ne ii]  $\lambda 3869\text{\AA}$  emission strength. Whilst some level of [Fe x]  $\lambda 6376\text{\AA}$  emission in the DESI spectrum is possible but telluric contamination and instrumentation artefacts prevent its confirmation. The emission feature observed just blueward of [Fe x]  $\lambda 6376\text{\AA}$  in the Keck+LRIS spectrum is likely to be [O i]. *Bottom row:* BPT diagnostic diagrams for all spectral epochs.

## 5.2 AGN-linked candidates

We now describe the six candidate objects that were identified during the analysis process as potentially the result of TDEs, but were ultimately being the result of AGN activity.

### 5.2.1 DESI 39627700695996439 : Venusaur

Venusaur was identified as a potential ECLE candidate by an earlier development version of SLEIPNIR, and does not meet the standard selection criteria used in the ‘live’ version of the code and is thus not included in the formal EDR CrL Object Sample. We include

discussion of the object here, as due to its early identification we obtained several follow-up data sets of the object, including both photometry and spectra.

Venusaur was identified as a potential TDE-ECLE candidate based on the presence of [Fe vii] and [Fe xiv] emission lines (see Fig. 15). The [Fe vii]  $\lambda 6088\text{\AA}$  line now fails the current line strength requirements, with the other [Fe vii] emission lines also too weak to trigger the spectrum for visual inspection through the back-up flagging criteria.

Following its initial identification, we triggered spectroscopic follow-up with Gemini+GMOS and optical photometric observations with LT+IO:O. Both sets of follow-up observations revealed no sig-

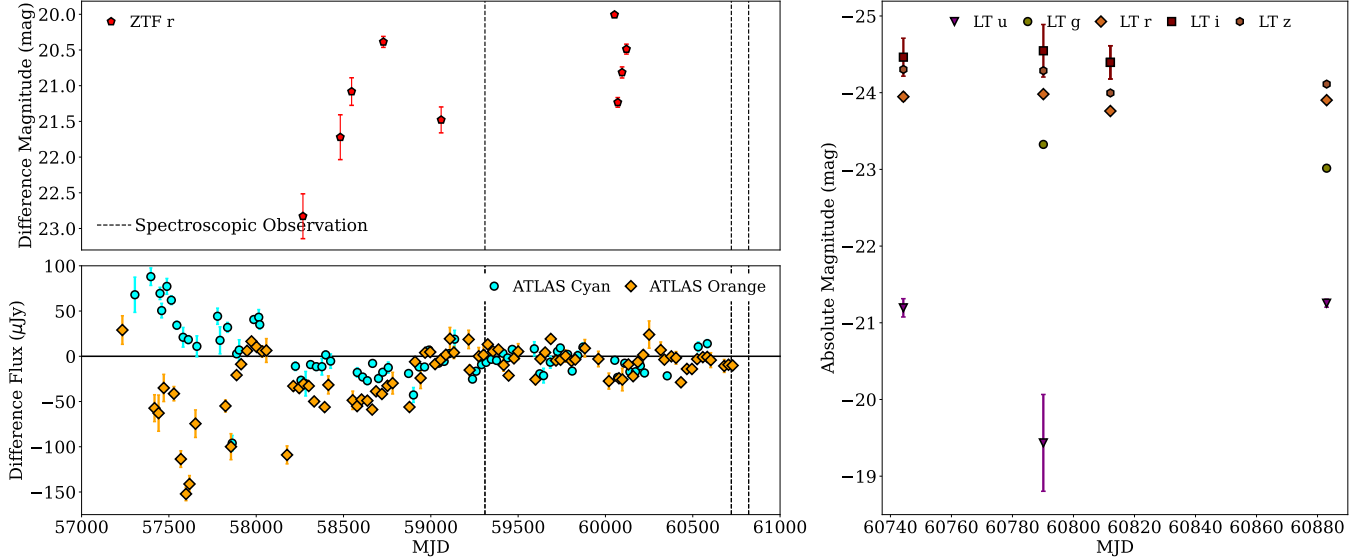


**Figure 10.** Photometric evolution of Pidgeot. *Top left:* ZTF forced photometry difference magnitude light curve. *Bottom left:* ATLAS forced photometry light curve presented in flux space. *Right:* LT absolute magnitude light curve.

nificant changes, with the Fe CrLs well recovered in Gemini+GMOS spectrum and remaining unchanged. Likewise, photometric follow-up with the LT (later supplemented with analysis of ATLAS and ZTF observations - Fig. 16) has shown no evidence for outbursts or other evolution. Additionally, the MIR behaviour and optical emission line properties (e.g., the very prominent [O III]  $\lambda 5007\text{\AA}$  emission feature) of Venusaur strongly indicate the dominance of AGN activity, with a lack of detection in either VLA-FIRST or VLASS suggesting this activity is radio-quiet.

#### 5.2.2 DESI 39633255741260888 : Charizard

Charizard was identified early in our analysis of the EDR sample by the presence of multiple clear CrLs (though lacking [Fe XIV] emission). We triggered targeted spectroscopic follow-up with Gemini+GMOS and optical photometric observations with LT+IO:O. The spectroscopic observation with Gemini revealed no change in the CrL-emission lines (see Fig. 17) but note the contamination affecting the GMOS observation of [Fe X] which makes its non-detection unreliable), with optical photometric observations also showing no signs of outburst or significant fading activity (Fig. 18). The LT observations do show some indications of repeated fading and re-brightening activity in the *riz* bands, but the large uncertainties on these observations make such trends difficult to confirm. Additionally, such behaviour is not observed in ATLAS or ZTF observations.

In the MIR (Fig. 7), Charizard displays repeated cycles of brightening and fading by a few 0.1 mags in both the *W1* and *W2* bands, consistent with AGN activity and further supported by a *W1*-*W2* colour above the Stern et al. (2012) AGN activity threshold. As with Venusaur, the lack of detections in either VLA-FIRST or VLASS suggest that this activity is radio-quiet.

#### 5.2.3 DESI 39633255741260888 : Fearow

Fearow was identified by SLEIPNIR as an ECLE candidate based on the detection of an extremely strong [Fe XIV] feature, with a pEQW of  $-30.89\text{\AA}$  - by far the strongest CrL feature detected in our search.

Visual inspection revealed an unusual spectrum with multiple strong emission features. Fearow lacks both 2MASS NIR and *WISE* MIR detections in any band. Additional optical photometry from ZTF shows no sign of outburst behaviour over the course of the survey. ATLAS observations display a large outburst, ( $\sim$  MJD 58000). However, following an inspection of the difference imaging, we attribute this to issues with the image subtraction at these epochs rather than true transient activity.

Following a re-examination of the spectrum, we conclude that Fearow is a broad-line absorption QSO that experienced a redshift measurement failure during processing by REDROCK. We estimate that the true redshift of the galaxy is  $z = 3.928$ , with the detected '[Fe XIV]' feature in reality produced by N V. The strong emission features displayed in the spectrum are thus (in order of increasing wavelength): Ly $\alpha$ , N V, C IV, and a broad and blueshifted C III feature. As the detection of [Fe XIV] has been determined to be a false positive, Fearow is not included in the EDR CrL Object Sample.

#### 5.2.4 DESI 39633066745924399 : Arbok

Arbok was identified by SLEIPNIR as a potential ECLE based on the presence of weak but consistent [Fe VII] emission lines. A visual inspection of the spectrum confirmed this automated assessment, whilst also revealing the presence of very broad H features.

Arbok was also spectroscopically observed by the SDSS BOSS (MJD 55480 i.e.,  $\sim 10$  yrs prior to the DESI spectrum). The SDSS automatic analysis pipeline incorrectly identified the broad H $\alpha$  feature as Ly $\alpha$  emission, resulting in an erroneous redshift determination of  $z=6.6$ , which excluded the spectrum from our previous BOSS ECLE search (Callow et al. 2025). A comparison between the two spectra, including detailed comparisons of the [Fe VII] emission lines, is shown in Fig. 21. We note that the SDSS Legacy and DESI spectra were obtained with fibres of differing diameter (2 and 1.5 arcseconds, respectively). As such, the two spectra do not explore identical regions of the galaxy despite both being centred on the nucleus. We have previously explored the potential effect this aperture size difference may have on the interpretation of ECLEs through our

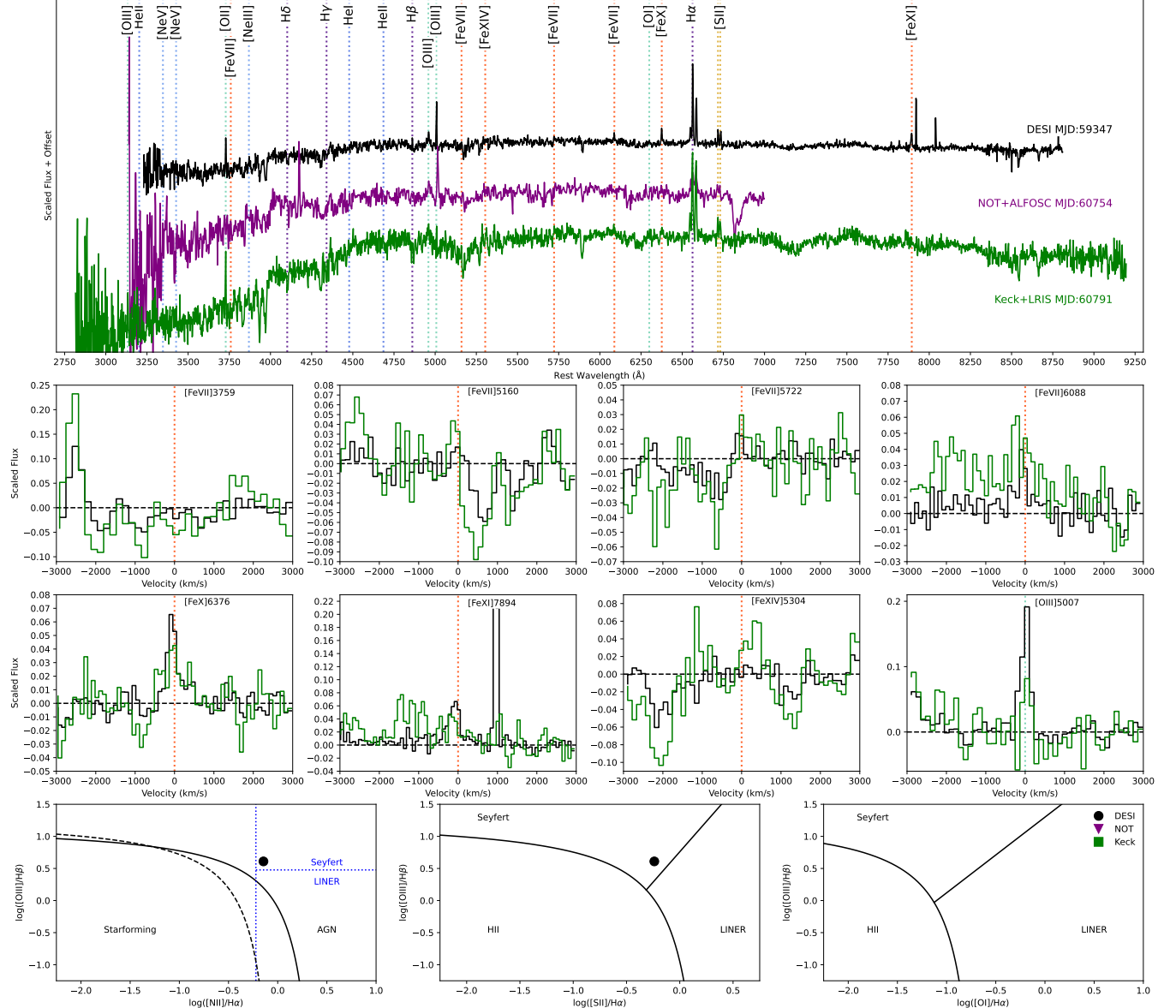


**Figure 11.** In all panels spectra have been rebinned to a shared 2 Å wavelength regime, but have not otherwise been smoothed. *Top row:* Spectral evolution of Raticate. *Second and third rows:* Comparison between the spectral features of most interest between the DESI and Keck+LRIS spectra. *Bottom row:* BPT diagnostic diagrams for the DESI spectrum. The NOT+ALFSOC spectrum is not included in these subplots due to a wavelength calibration issue. Values for the Keck spectrum are also not included due to the non-detection of H $\beta$  and [O I]/H $\alpha$  was not measured in the DESI spectrum due to the non-detection of [O I]  $\lambda 6300\text{\AA}$ .

analysis of synthetic aperture spectra derived from a MaNGA IFU spectral dataset of the host of the CrL-TDE AT 2018dyk and found this effect to be negligible (Clark et al. 2025). While we do not have corresponding MaNGA data of Arrokoth for a similar level of comparison, we find it unlikely that the aperture size difference would significantly influence the overall spectral properties observed. We do, however, note that the redshift of Arrokoth is  $\sim 0.4$  compared to the  $\sim 0.04$  redshift of AT 2018dyk, which means the the physical size differences between the apertures are larger in this case.

The spectral comparison reveals the optical spectrum of Arrokoth to be largely unchanged over the intervening 10.5 yrs. The weak [Fe vii] coronal line emission was already present at the time of the SDSS spectrum, in addition to prominent [Ne iii] and [Ne v] emission

features. Variability in the broad H $\alpha$  and H $\beta$  complexes is observed with changes in the line profiles, with the features being relatively stronger in the DESI spectrum. Despite this, their presence in the SDSS spectrum confirms that they are not related to the occurrence of a transient outburst.

The optical photometry from ATLAS and ZTF shows two clear states in the object's luminosity: a 'high' state from the start of optical observations until  $\sim$  MJD 59000, followed by a decline across all optical bands until a 'low' state is reached at  $\sim$  MJD 59400. During this state-change a colour change is also observed, with the colour in the high state (maximal  $g-r = \sim 1$ ) being significantly redder than in the low state ( $g-r = \sim 0$ ). The DESI spectrum obtained on MJD 59282 lies close to the end of this state change. No associated

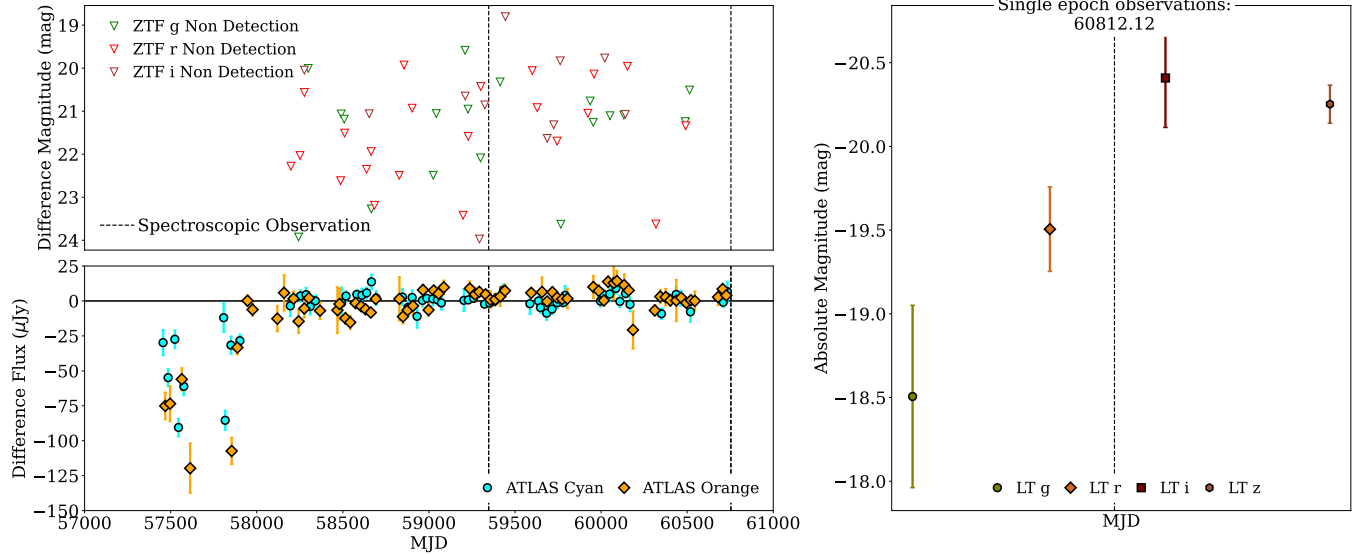


**Figure 12.** Photometric evolution of Raticate. *Top left:* ZTF forced photometry difference magnitude light curve. *Bottom left:* ATLAS forced photometry light curve presented in flux space. *Right:* LT absolute magnitude light curve.

radio sources are observed in either VLA-FIRST or VLASS. The lack of long-term spectral variability of the coronal lines, optical emission line diagnostics and both NIR and MIR photometric diagnostics all indicate that Arbok is driven by AGN activity.

#### 5.2.5 DESI 39633255741260888 : Sandslash

Like Arbok, Sandslash was identified by SLEIPNIR as a potential ECLE through the presence of weak but clearly detected [Fe VII] emission lines. Visual inspection confirmed these [Fe VII] lines, along with additional weak (below the pEQW detection thresholds of SLEIPNIR) [Fe x], [Fe xi], and [Fe xiv] emission lines.

Also clearly visible from a cursory inspection of the spectrum are strong emission signatures associated with AGN activity, such as [O III] and S II. BPT diagnostics confirm that all three of the usual diagnostics are well within the parameter space occupied by Seyfert AGNs.

Sandslash also has an archival SDSS-Legacy spectrum obtained on MJD 52365 (i.e.,  $\sim 19$  yrs prior to the DESI spectrum, see Fig. 23). The spectral comparison reveals the observed CrLs were also present at the time of the SDSS spectrum, with the SDSS and DESI spectra very similar overall, though with the DESI spectrum having a slightly bluer continuum. The weakness of the overall features is the primary reason why the object was not identified in our previous SDSS based search. We note that the [Fe xi] emission is stronger in the SDSS spectrum, indicating that some variability in the Fe CrLs displayed by AGNs may be expected when explored over long enough timescales.

Despite this spectral similarity, Sandslash was selected for further analysis as its MIR behaviour and colour are more typical of a quiescent galaxy rather than an AGN. AIWISE W1-W2 vs W2-W3 colour information provides an unclear classification, with Sandslash occupying a parameter region consistent with a range of galaxy types (spiral galaxies, LIRGS, ULIRGS, LINERS and starburst galaxies). More recent NEOWISE W1-W2 photometry suggests a lack of strong AGN activity, with a stable value of  $\sim 0.24$  mag, significantly below the AGN identification threshold of 0.8 mag developed by Stern et al. (2012). We remind the reader that this threshold is

not a fully complete demarcation between AGNs and non-AGNs, with Stern et al. (2012) indicating an AGN completeness of 73 per cent for objects above their threshold. Sandslash additionally lies outside the Mateos et al. (2012) AGN wedge (unsurprising given the similar W1-W2 threshold), which becomes less sensitive at lower AGN luminosities. Sandslash's host galaxy also has a somewhat disturbed morphology (Figure 6) that could indicate possible interaction or mergers that may affect the MIR AGN diagnostic. Furthermore, Sandslash does not display either an W1-W2 outburst or long-term decline expected of a TDE-ECLE. Sandslash is not associated with a radio source in either VLA-FIRST or VLASS, but is coincident with an isolated and clearly detected radio source in LoTSS-DR2 (ILTJ113040.22+503704.7) further supporting its classification as being AGN-related.

Based on the lack of large spectroscopic or photometric evolution and radio detection, we classify Sandslash as the result of CrL-AGN activity (albeit from one with unusual MIR colours) rather than being TDE-related.

#### 5.2.6 DESI 39633290029695741 : Nidoqueen

Nidoqueen was again selected by SLEIPNIR for the presence of weak but clearly detected [Fe VII] emission lines, which were confirmed by visual inspection.

As with Arbok and Sandslash, Nidoqueen was spectroscopically observed by the SDSS-Legacy on MJD 52468 (19 yrs prior to the DESI observation) and as with these other objects, the [Fe VII] emission is seen to be persistent and accompanied by little overall spectral variability other than a somewhat bluer continuum in the DESI spectrum. Additionally, the wider wavelength coverage of the DESI spectrum allows for the detection of [Ne V]. Emission line diagnostics indicate the presence of a narrow-line AGN, given the high strength of the [O III] emission. ATLAS and ZTF photometry shows no signs of significant variability across the time period of observations.

As with Sandslash, Nidoqueen was further analysed due to its MIR colour being atypical of an AGN, showing a W1-W2 colour of  $\sim 0.3$  mag at all epochs. Additionally, its NIR colours were not

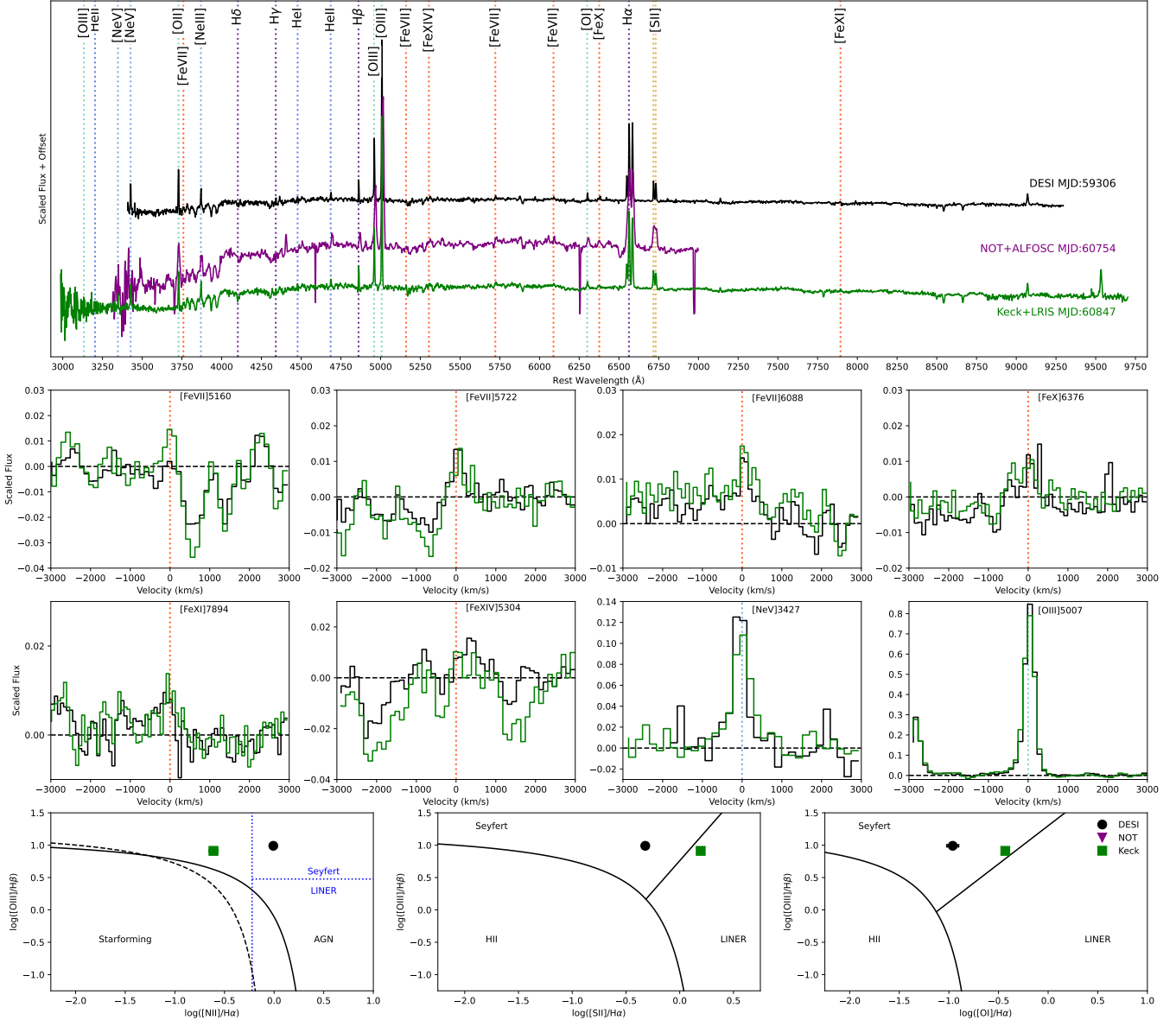


**Figure 13.** In all panels spectra have been rebinned to a shared 2 Å wavelength regime, but have not otherwise been smoothed. *Top row:* Spectral evolution of Raichu. *Second and third rows:* Comparison between the spectral features of most interest between the DESI and Keck+LRIS spectra. *Bottom row:* BPT diagnostic diagrams for the DESI and Keck+LRIS spectra. The NOT+ALFSOC spectrum is not included in these subplots due to a wavelength calibration issue.

suggestive of the presence of an AGN (see Figure 8). As in the case of Sandslash, Nidoqueen's host galaxy also has a somewhat disturbed morphology in the DESI Legacy survey imaging (Figure 6) which may be at least partly responsible for its unusual NIR and MIR colours through mergers or interaction. Whilst Nidoqueen is not within the sky-coverage region of LoTSS-DR2, it is not associated with a radio source in either VLA-FIRST or VLASS suggesting its AGN activity is radio-quiet.

As with Sandslash, based on the lack of spectroscopic, or photometric evolution we classify Nidoqueen as the result of CrL-AGN activity (albeit from one with unusual MIR colours) rather than being linked to a TDE.

## 6 ANALYSIS

### 6.1 MIR behaviour comparison

We compare the MIR outburst behaviour of the three candidates we identify as being most likely TDE-related to the behaviour of the CrL object sample described by Clark et al. (2025). First, we compare the AllWISE  $W1-W2$  vs  $W2-W3$  colours of the candidates to those of the Wang et al. (2012) sample, as shown in Fig. 27.

During the time of the AllWISE observations, Pidgeot was in a quiescent state and displayed the MIR colours of a star-forming galaxy without any significant AGN activity (noting the contamination from the star in close observational proximity as previously described). Raichu occupied a similar location in this parameter space as SDSS J1241+4426, which also showed a slow consistent decline in both the  $W1$  and  $W2$  bands and an increasingly blue colour. Rati-

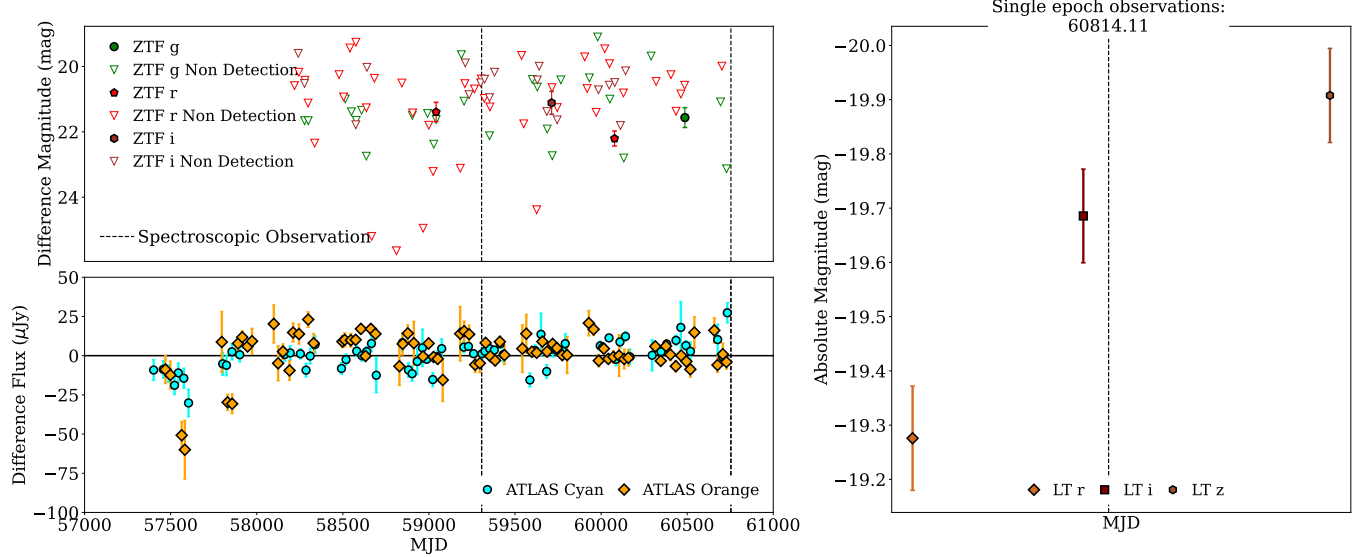


**Figure 14.** Photometric evolution of Raichu. *Top left:* ZTF forced photometry difference magnitude light curve. *Bottom left:* ATLAS forced photometry light curve presented in flux space. *Right:* LT absolute magnitude light curve.

**Table 12.** Peak changes in absolute magnitude and colour of the MIR outbursts displayed by the DESI EDR TDE-ECLEs.

Object	$\Delta W1$	$\Delta W2$	$\Delta(W1-W2)$
Pidgeot <sup>1</sup>	$-0.66 \pm 0.01$	$-0.88 \pm 0.01$	$0.30 \pm 0.01$
Raticate <sup>2</sup>	$-1.32 \pm 0.02$	$-1.66 \pm 0.02$	$0.49 \pm 0.04$
Raichu	$< -0.12$	$< -0.25$	$< 0.15$

*Notes:* In all cases, values for each band and the overall observed peak colour change are determined independently and do not necessarily occur at the same phase.

<sup>1</sup> Pidgeot displays a long-term decline in both  $W1$  and  $W2$  bands apparently independent of its outbursts. These measured  $\Delta$  values are given following the removal of this long-term decline using a linear fit.

<sup>2</sup> Raticate displays two outbursts in *WISE* data. Measured  $\Delta$  values here reflect the second outburst for which the rise, peak and decline have all been observed. The quiescent period used for to set the baseline for these measurements is MJD 57048–58304.

cate was in an active/outburst state during the AllWISE observations, displaying MIR colours more typical of AGNs, and is found in the region of both the [Stern et al. \(2012\)](#) and [Mateos et al. \(2012\)](#) AGN regions, in similarity with the TDE-ECLEs in the [Wang et al. \(2012\)](#) sample.

As in [Clark et al. \(2025\)](#), we also measure and compare the maximum difference between outburst peak and pre-outburst quiescence ( $\Delta$  values) for both MIR bands and MIR colour for the DESI EDR TDE-ECLEs (Table 12 and Fig. 28).

The  $\Delta$  values for Raichu were measured in the same manner as the TDE-ECLEs explored in [Clark et al. \(2025\)](#), with the assumption that the original outburst occurred well before the start of MIR observations, so that the measured values reflect lower limits only.

The MIR behaviour of Raichu is most similar to SDSS J1241+4426 from the original [Wang et al. \(2012\)](#) ECLE sample, though the long-term per-band declining light curves and blueward colour trends displayed by Raichu are smaller overall across the same time frame ( $\Delta W1 < -0.12$ ,  $\Delta W2 < -0.25$ , and  $\Delta(W1-W2) > 0.15$  mag). SDSS J1241+4426 already displayed the smallest changes in both

bands and colour evolution ( $\Delta W1 < -0.30$ ,  $\Delta W2 < -0.61$ , and  $\Delta(W1-W2) > 0.35$  mag) compared to the means observed in the overall TDE-ECLE sample ( $\Delta W1 < -0.65$ ,  $\Delta W2 < -1.38$ , and  $\Delta(W1-W2) > 0.77$  mag; [Clark et al. 2025](#)).

As such, Raichu sits somewhat below the expected  $\Delta W2$  vs  $\Delta W1$  relation, though remains above the one-to-one ratio (Fig. 28). Given the lack of data from the start of outburst, we cannot determine if this represents a deviation from the expected behaviour at low outburst intensities or if the late-time behaviour observed does not represent the evolution as a whole.

The remaining two objects required additional analysis prior to the determination of their  $\Delta$  values. As described in Section 5.1.1, Pidgeot displays a long-term decline and blueward MIR colour trend in addition to the expected outburst from the occurrence of a TDE. To isolate this long-term decline from the outburst, we first remove the observations from the start of the outburst (MJD 57215) to its apparent end, as determined by the last point to be on a consistent decline (MJD 58501). We perform a linear fit to the remaining data points and use these fits to normalise the light-curves without the long-term behaviour. Following this step, we return to the method used by [Clark et al. \(2025\)](#), with the first observation post outburst in both bands now identified as occurring at MJD 58298.

From these long-term linear fits, we find a  $W1$  decline of  $3.9 \times 10^{-5}$  mag d $^{-1}$  and  $W2$  decline of  $6.8 \times 10^{-5}$  mag d $^{-1}$ , though we note that the increasing rate of decline in  $W2$  following MJD 60000 is not well described by this general fit. The  $\Delta$  values measured for Pidgeot following this correction are within the expected parameter range of CrL-TDEs, further supporting its classification as being TDE-related (see Fig. 28).

As noted in Section 5.1.2, Raticate displays two distinct MIR outbursts, with the first beginning, and likely peaking, prior to the start of MIR observations. We base our  $\Delta$  analysis on the second outburst, for which the start, peak and decline are all observed.

We set the quiescent baseline as the mean observed magnitudes in the MJD range 57048–58304, with the first observation in the second outburst occurring at 58507. As with Pidgeot, we find the measured  $\Delta$  values to be within the expected parameter ranges for

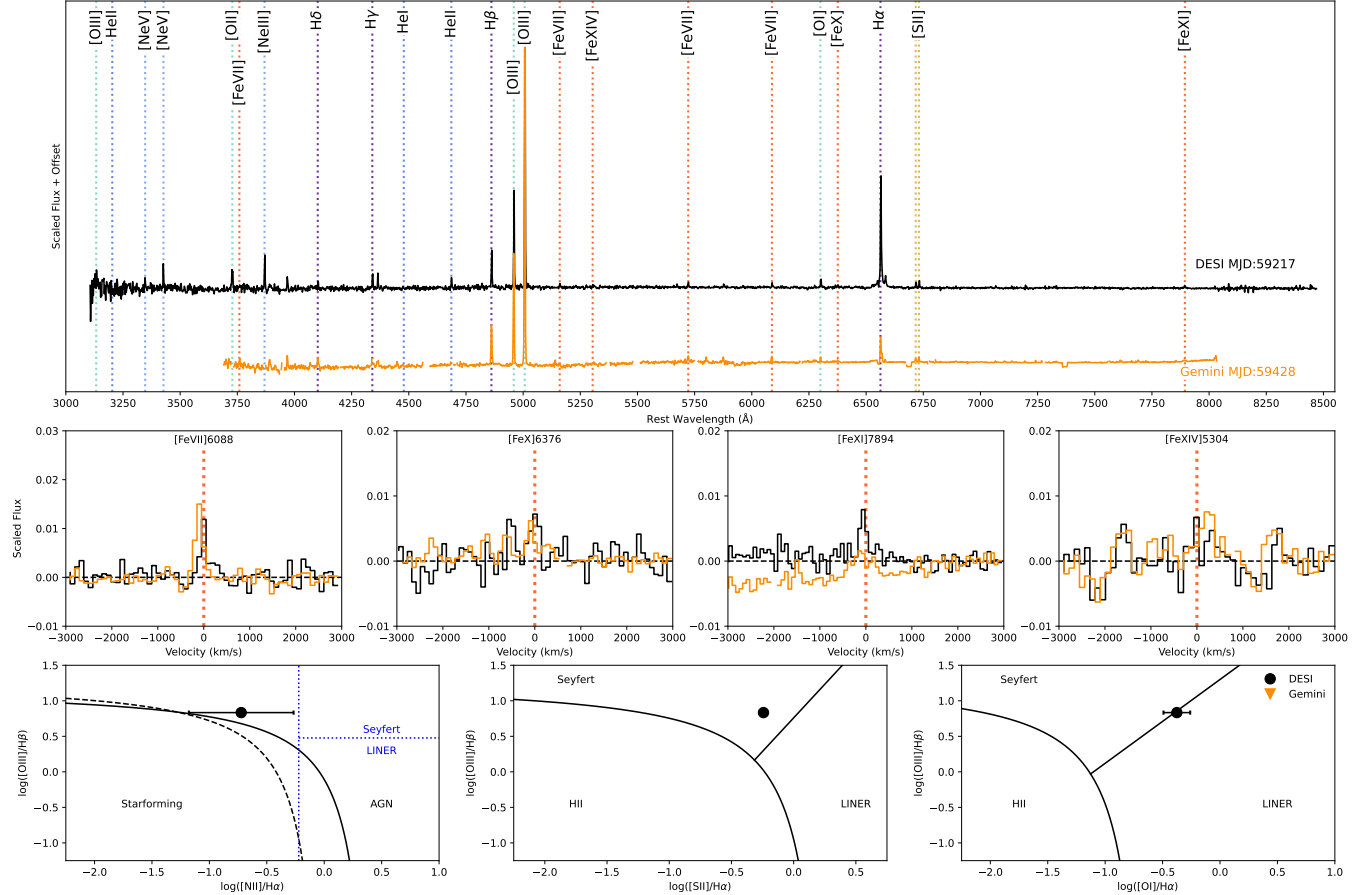


**Figure 15.** In all panels spectra have been rebinned to a shared 2  $\text{\AA}$  wavelength regime, but have not otherwise been smoothed. *Top row:* Spectral observations of Venusaur from both DESI and Gemini+GMOS. Prominent emission lines are labelled (coloured by element). Spectra have been normalised relative to the flux of the strongest feature and then offset from each other for ease of interpretation. *Middle row:* Comparison between the strongest Fe CrLs in velocity space, following a calibration matching each spectrum's mean flux at 2000–3000  $\text{km s}^{-1}$ . Fe emission is unchanged between the two spectra, though not possible to confirm for [Fe xi] which suffered from an artificial offset in the Gemini+GMOS spectrum due to issues with flux calibration. *Bottom row:* BPT diagnostic diagrams for the DESI spectrum. BPT diagrams have not been produced for the Gemini+GMOS spectrum due to the significant atmospheric contamination of the  $\text{H}\alpha$  feature.

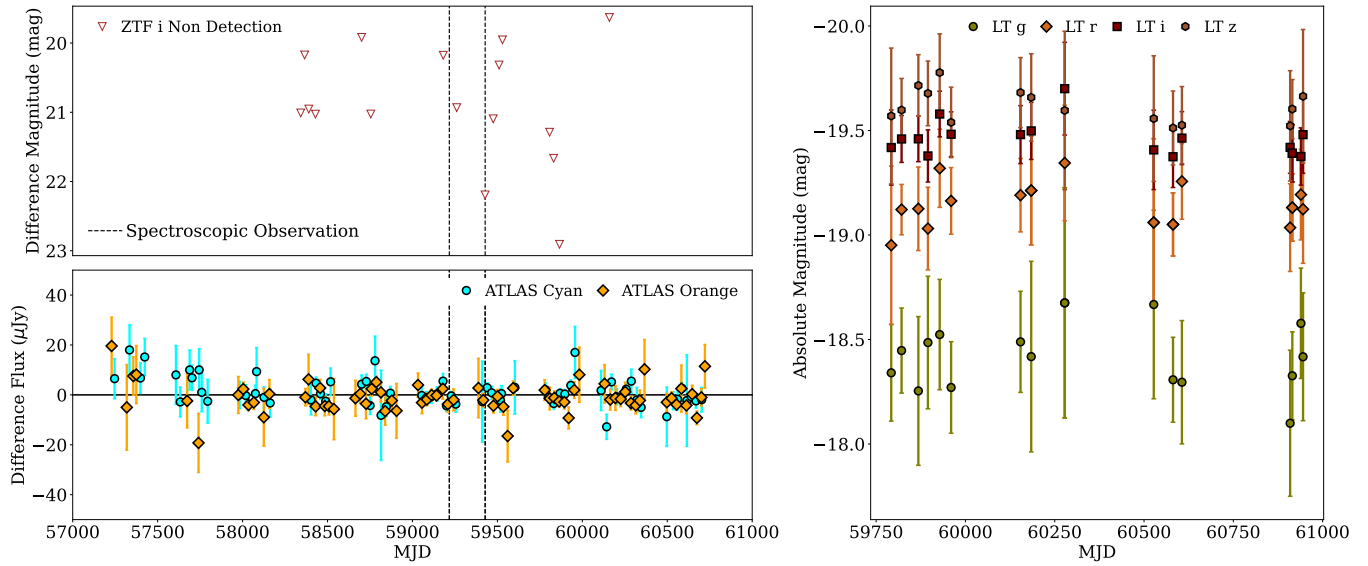


**Figure 16.** Photometric evolution of Venusaur. *Top left:* ZTF forced photometry difference magnitude light curve. *Bottom left:* ATLAS forced photometry light curve presented in flux space. *Right:* LT absolute magnitude light curve.

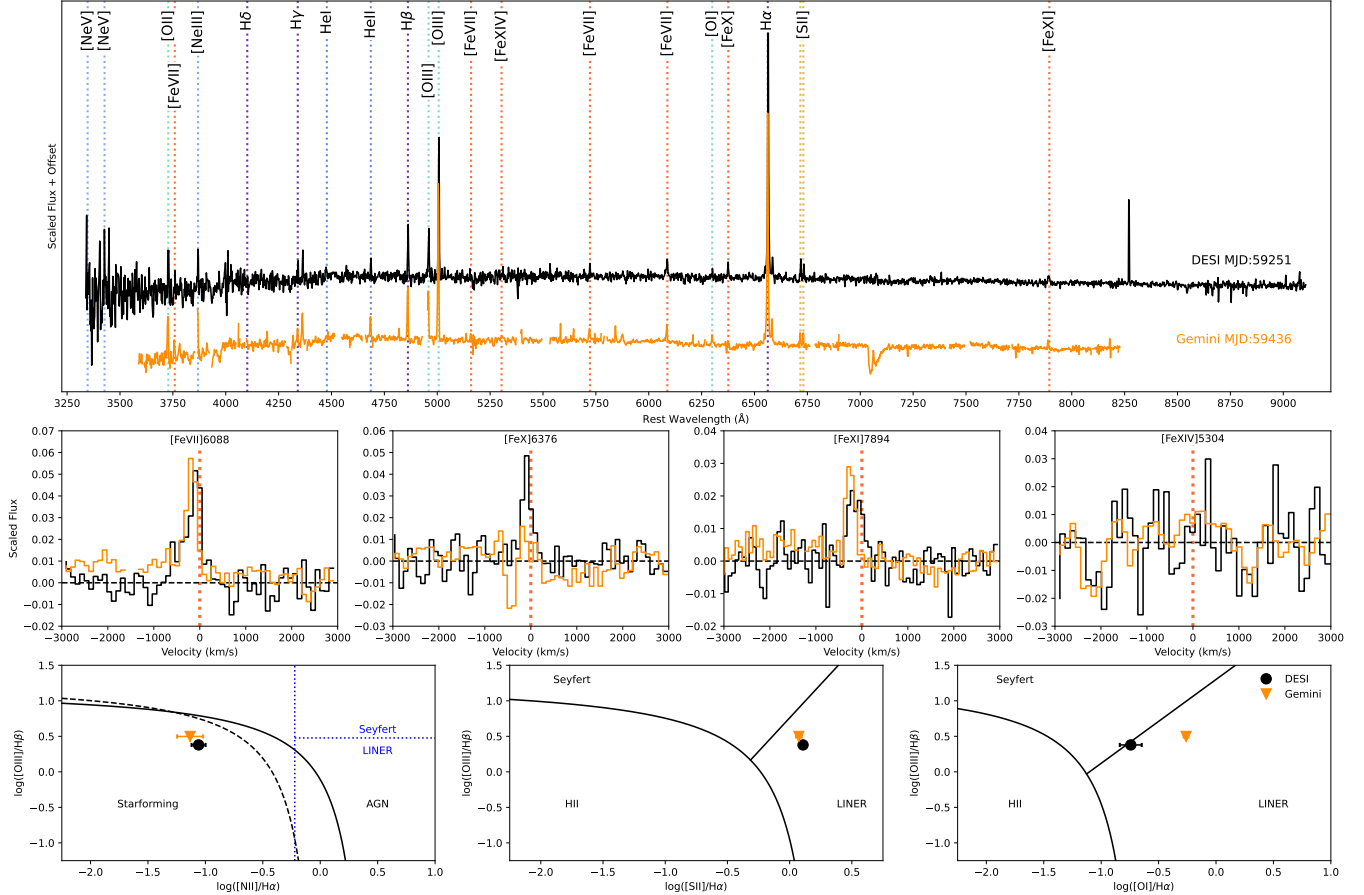


**Figure 17.** In all panels, both spectra have been rebinned to a resolution of 2 Å prior to display. *Top row:* Spectral observations of Charizard from both DESI and Gemini+GMOS. Prominent emission lines are labelled (coloured by element). Spectra have been normalised relative to the flux of the strongest feature and then offset from each other for ease of interpretation. *Middle row:* Comparison between the strongest Fe CrLs in velocity space, following a calibration matching each spectrum's mean flux at 2000–3000 km s<sup>-1</sup>. Fe emission is unchanged between the two spectra, though this is not possible to confirm for [Fe x] which suffered from telluric contamination in the Gemini+GMOS spectrum. *Bottom row:* BPT diagnostic diagrams for the DESI and Gemini+GMOS spectra showing broadly similar results. The difference in [O I] over H $\alpha$  ratio being driven by a somewhat broader [O I] line observed in the Gemini spectrum.

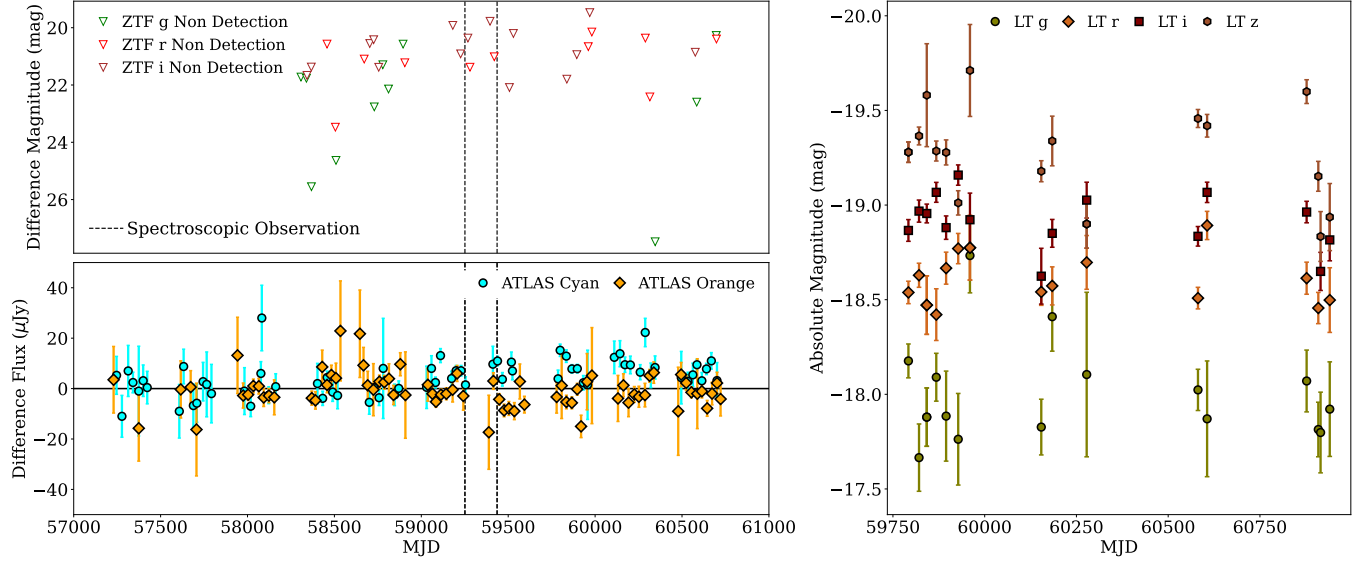


**Figure 18.** Photometric evolution of Charizard. *Top left*: ZTF forced photometry difference magnitude light curve. *Bottom left*: ATLAS forced photometry light curve presented in flux space. *Right*: LT absolute magnitude light curve.

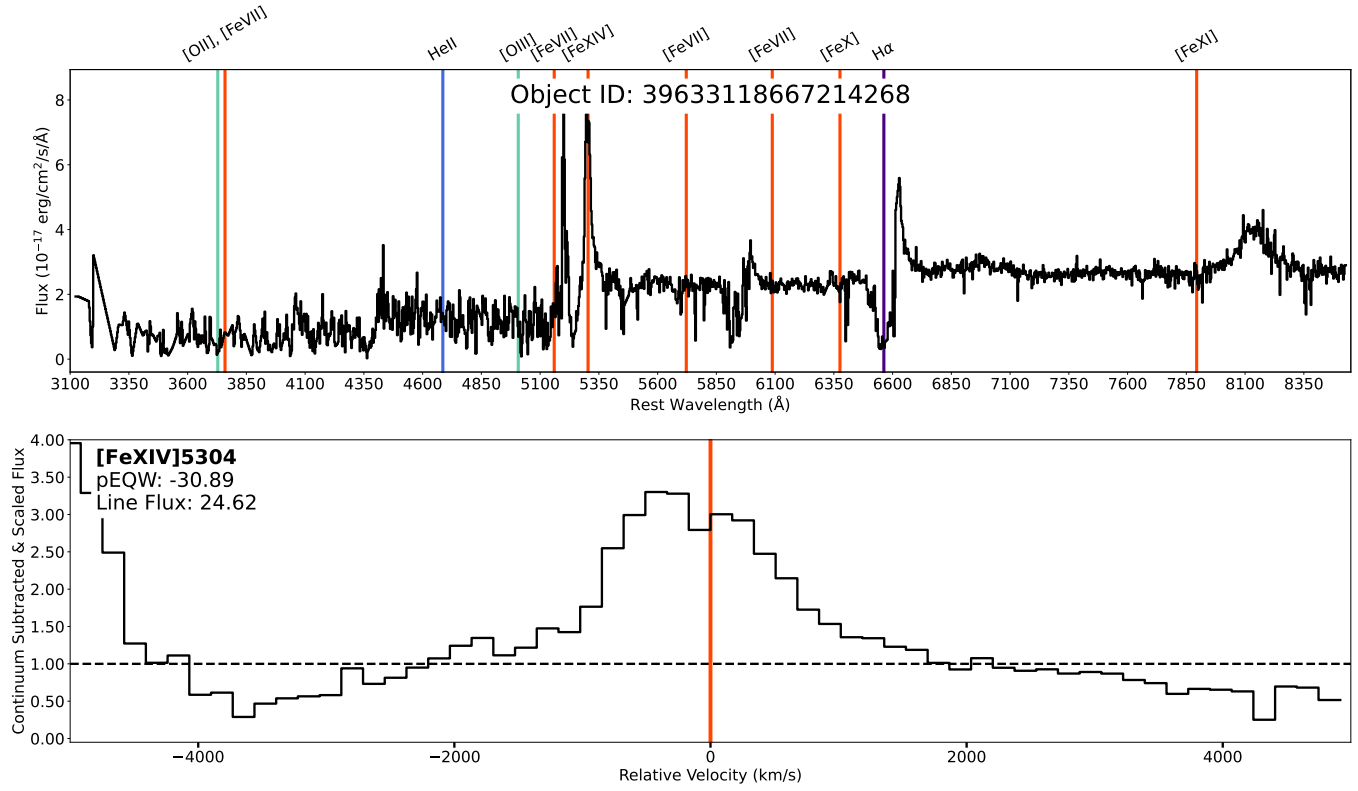


**Figure 19.** *Top*: DESI spectrum of Fearow, showing at the erroneous redshift determined by REDROCK ( $z = 0.152$ , compared to correct  $z = 3.928$ ), a strong N $\vee$  feature appears as [Fe XIV]. Emission lines displayed are shown if the REDROCK determined redshift was accurate. In reality, these features are (in order of increasing wavelength) Ly $\alpha$ , N $\vee$ , C IV and a broad blueshifted C III featurex. *Bottom*: Region local to the '[Fe XIV]' feature.

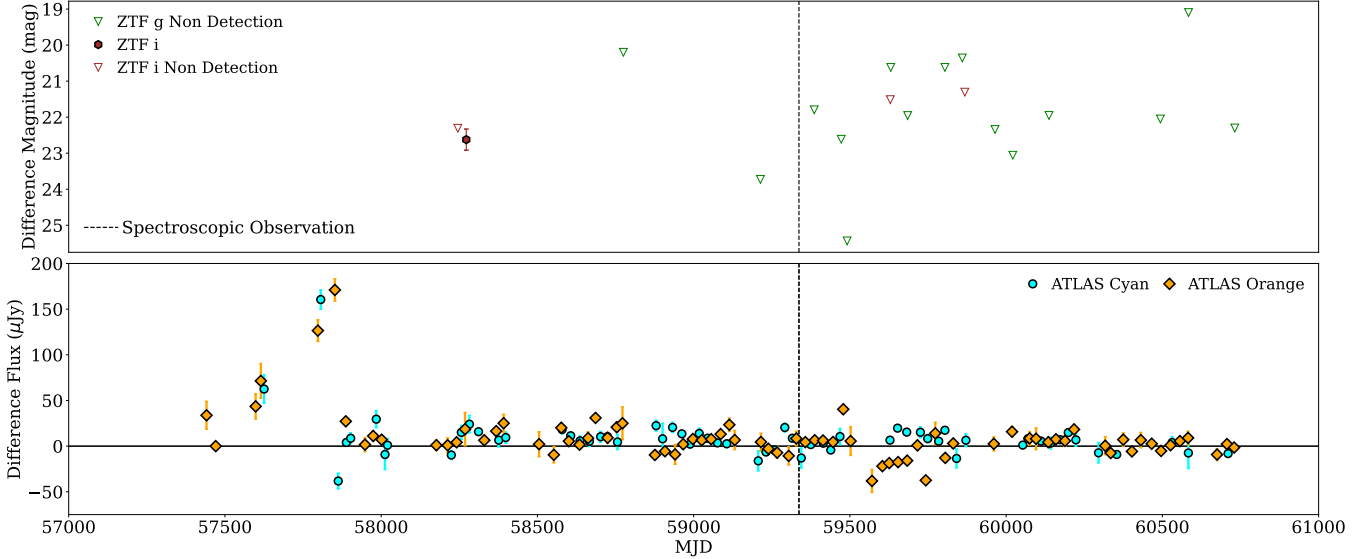


**Figure 20.** Photometric evolution of Fearow. *Top:* ZTF forced photometry difference magnitude light curve. *Bottom:* ATLAS forced photometry light curve presented in flux space.

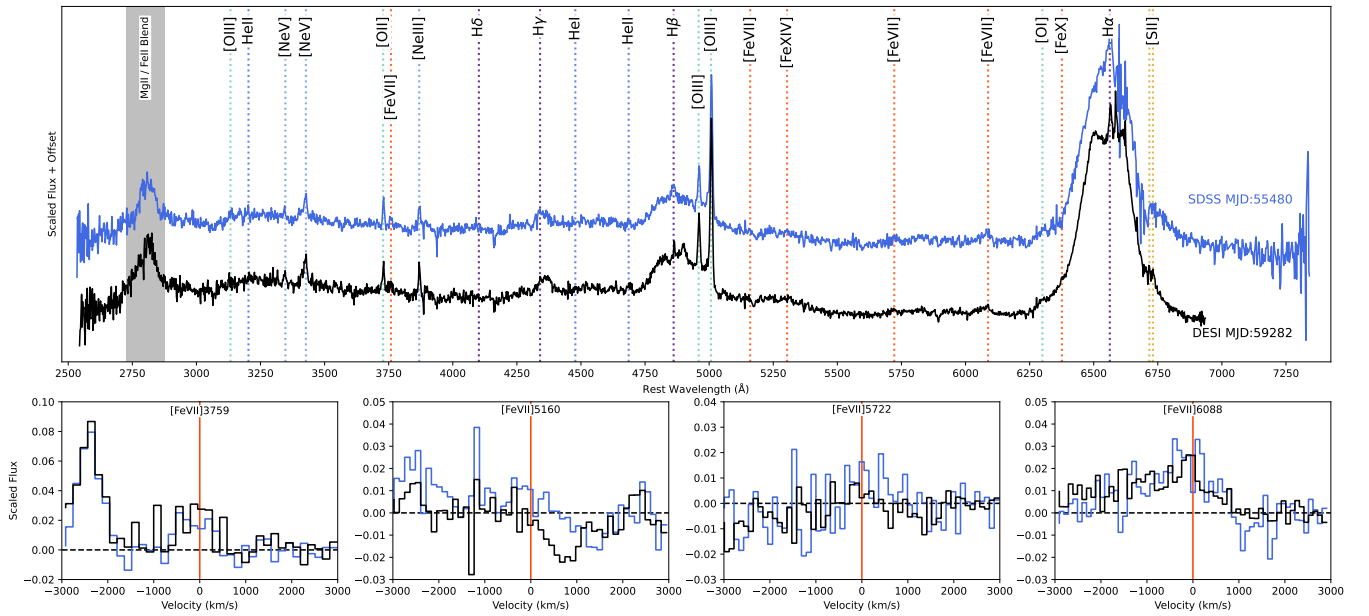


**Figure 21.** In all panels, both spectra have been rebinned to a resolution of  $2 \text{ \AA}$  prior to display. *Top row:* Spectral observations of Arbok from both SDSS-BOSS and DESI. Prominent emission lines are labelled (coloured by element). Spectra have been normalised relative to the flux of the strongest feature and then offset from each other for ease of interpretation. *Bottom row:* Comparison between the spectra lines of most interest in velocity space, following a calibration matching each spectrum's mean flux at  $2000-3000 \text{ km s}^{-1}$ . [Fe VII] emission whilst, weak, is present largely unchanged in both spectra. Note: Due to the significant broad H features present, we do not attempt line de-blending to produce BPT diagrams for Arbok.

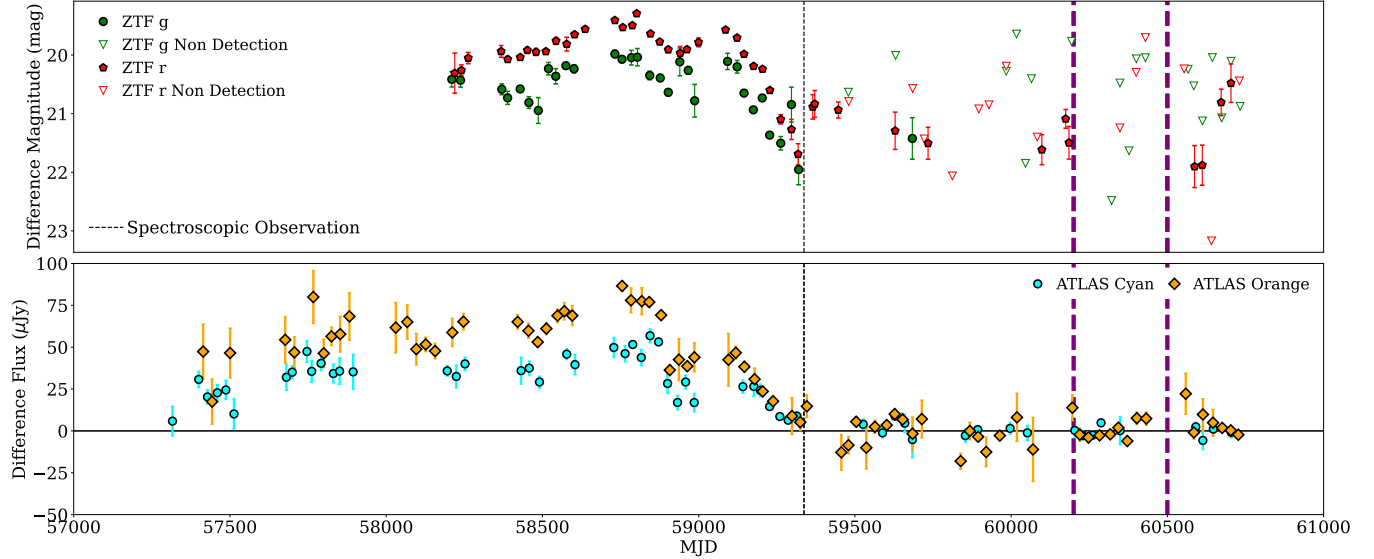


**Figure 22.** Photometric evolution of Arbok. Observational time frame used to re-reference the forced photometry are shown by the thick dashed purple lines. Observation time frame chosen to select the ‘low-state’ as the baseline for comparison. *Top*: ZTF forced photometry difference magnitude light curve. *Bottom*: ATLAS forced photometry light curve presented in flux space.

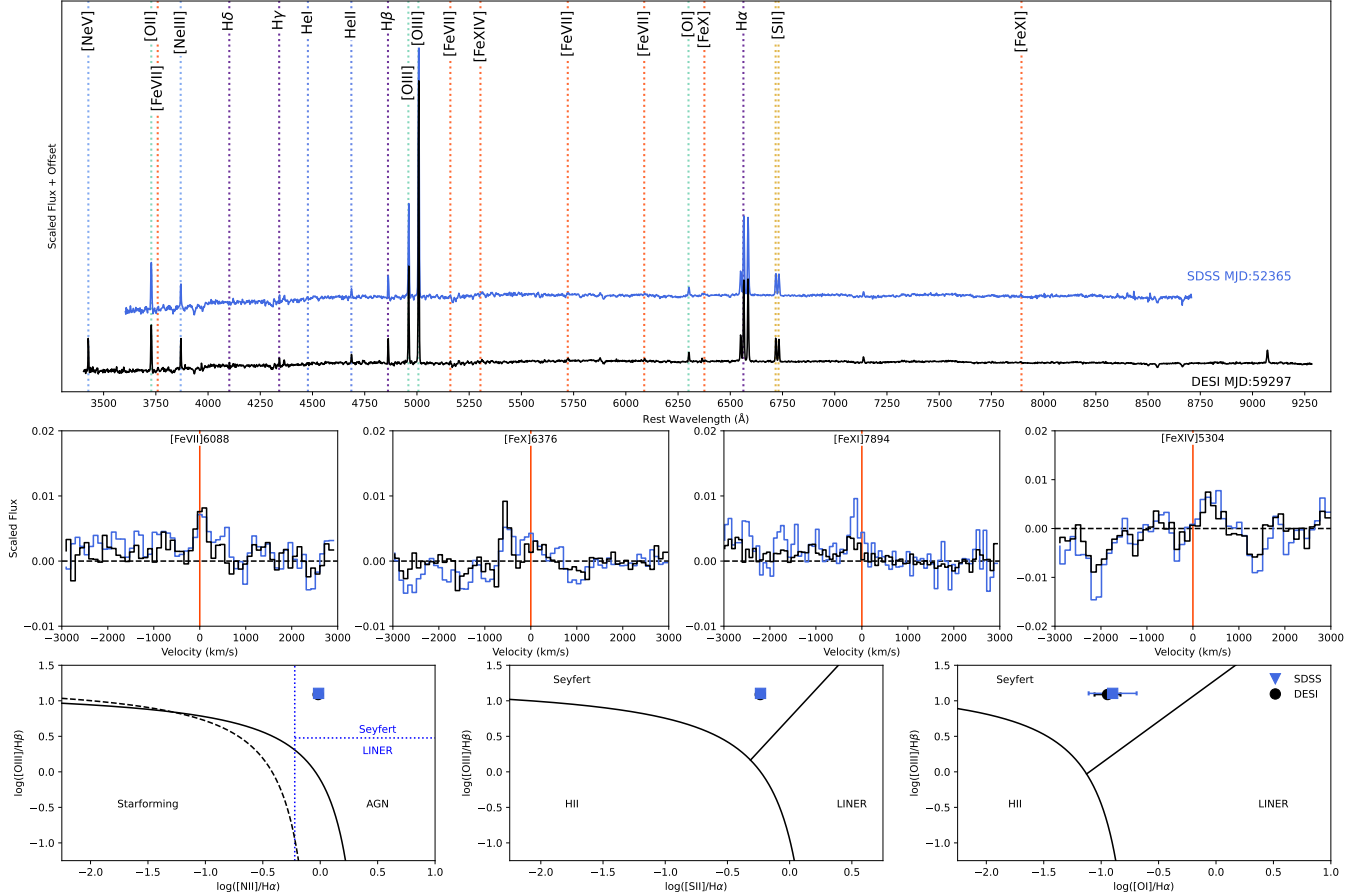


**Figure 23.** In all panels, both spectra have been rebinned to a resolution of  $2 \text{ \AA}$  prior to display. *Top row:* Spectral observations of Sandslash from both SDSS-Legacy and DESI. Prominent emission lines are labelled (coloured by element). Spectra have been normalised relative to the flux of the strongest feature and then offset from each other for ease of interpretation. *Middle row:* Comparison between the spectra lines of most interest in velocity space, following a calibration matching each spectrum's mean flux at  $2000-3000 \text{ km s}^{-1}$ .  $[\text{Fe VII}]$  and  $[\text{Fe X}]$  emission are close matches despite the  $\sim 19$  yr between the two spectra.  $[\text{Fe XI}]$  whilst still present in the DESI spectrum is somewhat reduced indicating that some variability in the Fe CrLs displayed by AGNs may be expected over long-timescales. *Bottom row:* BPT diagnostic diagrams for the SDSS and DESI spectra.

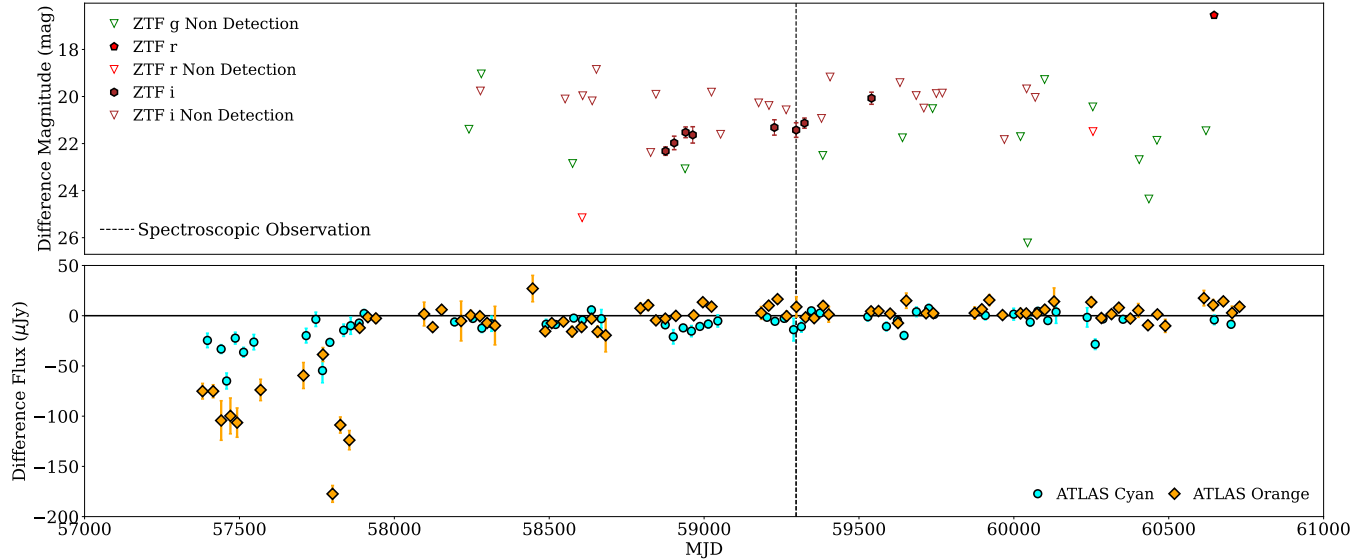


**Figure 24.** Photometric evolution of Sandslash. *Top:* ZTF forced photometry difference magnitude light curve. *Bottom:* ATLAS forced photometry light curve presented in flux space.

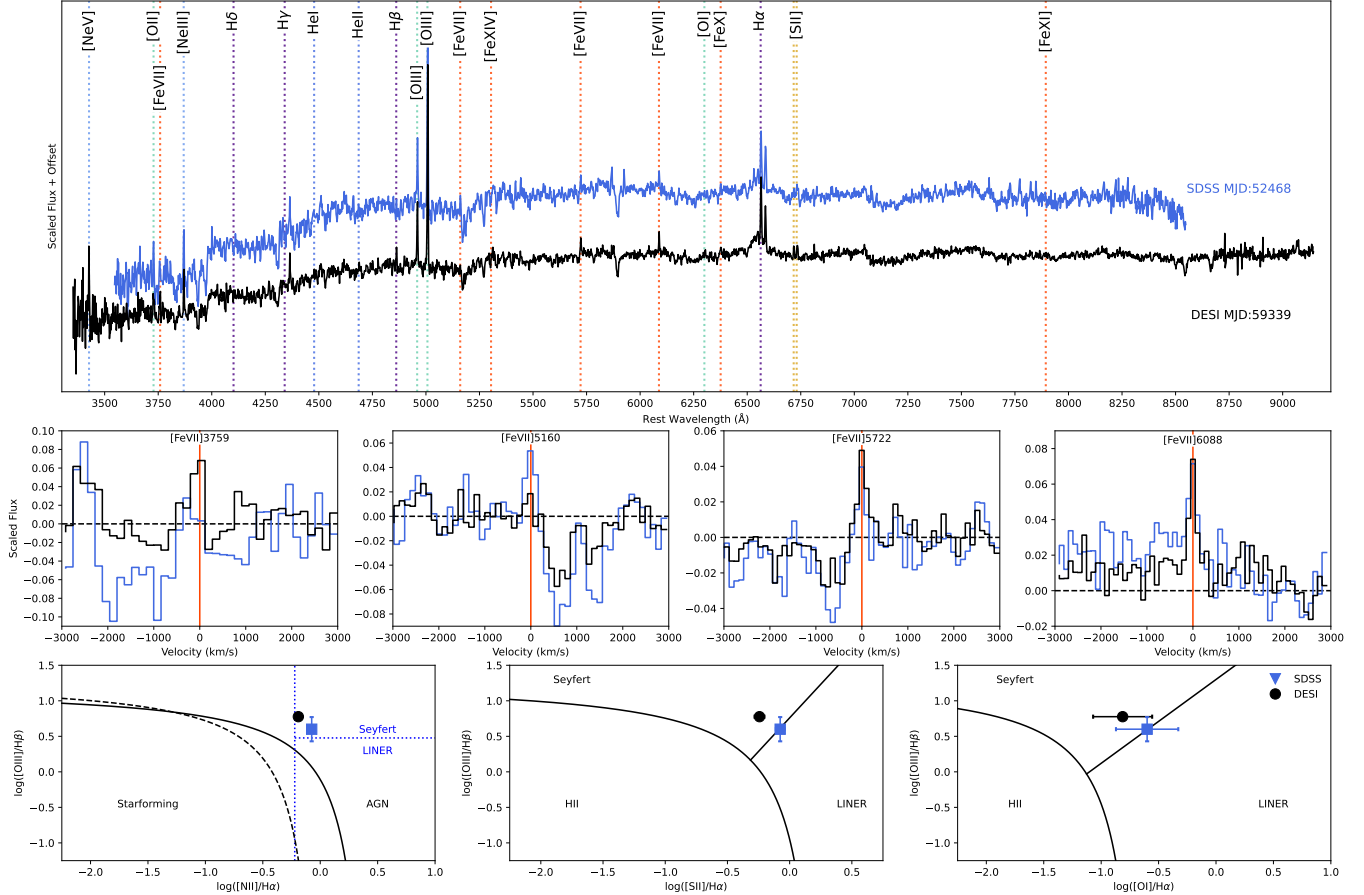


**Figure 25.** In all panels spectra have been rebinned to a shared 2 Å wavelength regime, but have not otherwise been smoothed. *Top row:* Spectral observations of Nidoqueen from both SDSS-Legacy and DESI. Prominent emission lines are labelled (coloured by element). Spectra have been normalised relative to the flux of the strongest feature and then offset from each other for ease of interpretation. *Middle row:* Comparison between the spectra lines of most interest in velocity space, following a calibration matching each spectrum's mean flux at 2000–3000 km s $^{-1}$ . [Fe VII] emission is present in both spectra showing little evolution despite the  $\sim 19$  yr between the two spectra. *Bottom row:* BPT diagnostic diagrams for the SDSS and DESI spectra.

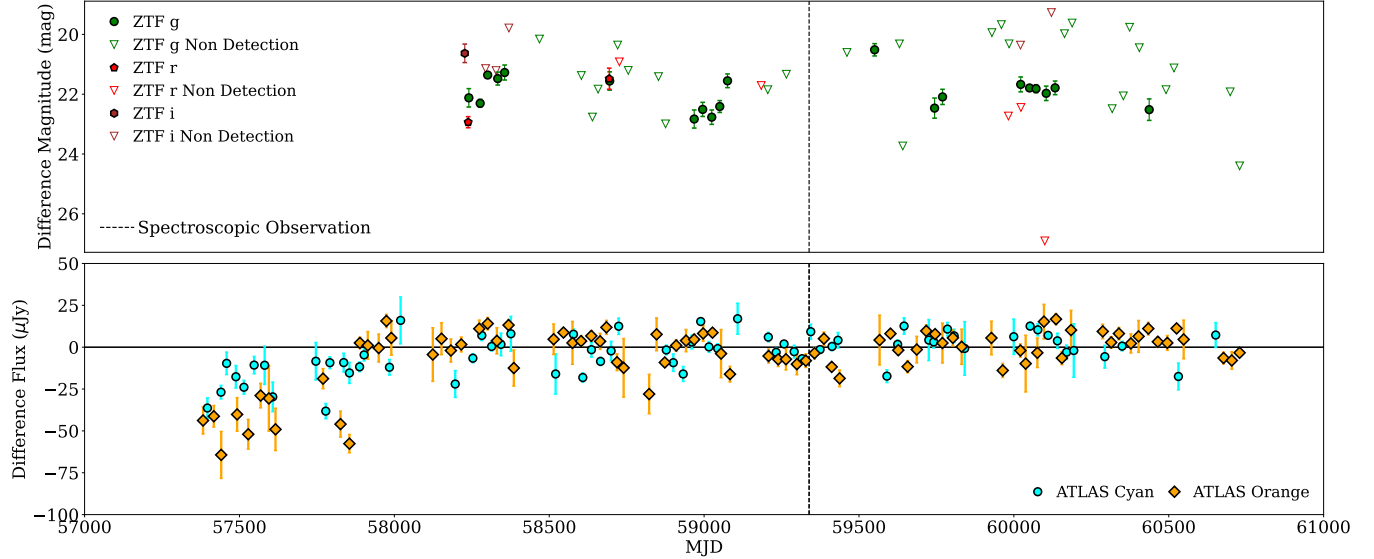


**Figure 26.** Photometric evolution of Nidoqueen. *Top:* ZTF forced photometry difference magnitude light curve. *Bottom:* ATLAS forced photometry light curve presented in flux space.

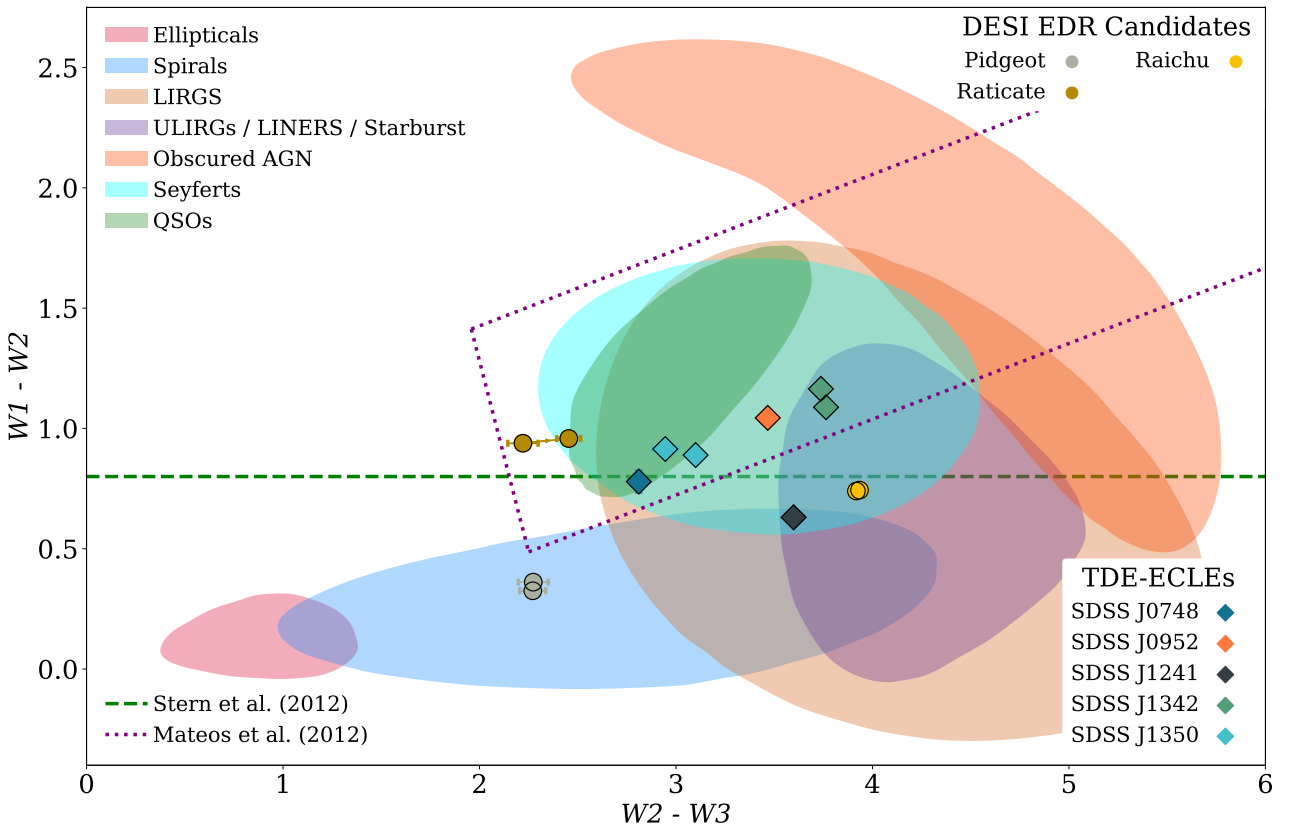


**Figure 27.** AllWISE colour-colour plot showing the DESI EDR TDE-ECLE candidates (circles) in comparison to the Wang et al. (2012) sample of TDE-ECLEs (diamonds). Regions have been sourced from Wright et al. (2010). The AGN identification cuts from Stern et al. (2012) and Mateos et al. (2012) are included as a green dashed line and purple dotted lines, respectively. Uncertainties in both axes are included but are generally smaller than the points.

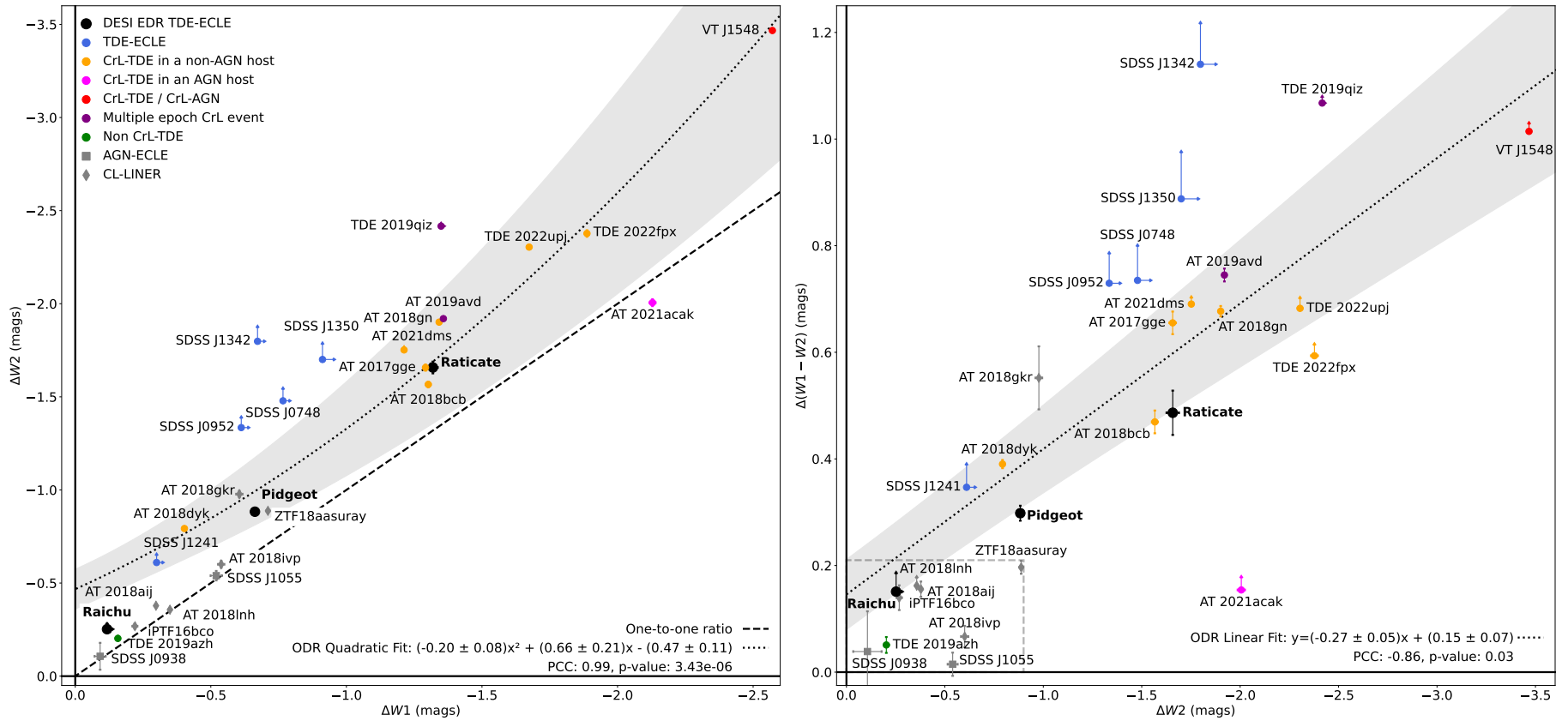


**Figure 28.** *Left:* Comparison between the maximum change in  $W1$  and  $W2$  between the DESI EDR TDE-ECLEs (black circles) and a range of comparison objects. Dashed black line shows a 1-to-1 relation. Dotted line shows the orthogonal distance regression (ODR) best fitting quadratic for the CL-TDEs excluding objects with only upper limits, with the shaded region displaying the  $1\sigma$  fitting uncertainty region. A quadratic fit to the data was preferred at a  $> 5\sigma$  level when tested against a constant and a linear fit using a likelihood ratio test, supported through AIC comparisons. A strong positive correlation is also supported by the Pearson's correlation coefficient with a value of 0.99 and corresponding p-value of  $3.4 \times 10^{-6}$ . *Right:* Comparison between the maximum change in  $W1 - W2$  colour versus maximum change in  $W2$  brightness. A trend is visible in the behaviour of the CrL-TDEs and TDE-ECLEs with those objects with brighter MIR outbursts (larger  $\Delta W2$  values) also showing larger shifts to MIR redder colours. Dotted line shows the ODR linear fit for this trend after excluding objects that only have upper limits on either variable, with the shaded region displaying the  $1\sigma$  fitting uncertainty region. Restricting the fit to objects with measurable values for both parameters (6), excluding those constrained only by upper or lower limits supports this assessment with the linear relation having a Pearson's correlation coefficient with a value of -0.86 and corresponding p-value of 0.03. We note that formally the statistical tests prefer a quadratic fit to the data, but given the lack of constraining points at low and high values of  $\Delta W2$ , this fit is not supported by the overall dataset when those objects measured as limits are considered. The region of parameter space occupied by the CL-LINERs from [Frederick et al. \(2019\)](#) and AGN-ECLEs (excluding AT 2018gkr) is demarcated by the dashed grey box.

CrL-TDE outbursts, supporting Raticate's classification as being at least partially driven by a TDE (see Fig. 28).

We fit a quadratic polynomial (preferred over a fixed constant or linear fit by a maximum likelihood and AIC comparison see Table E1) to our measurements, alongside those from Clark et al. (2025). The best-fitting curve, continues to reflect the increased magnitude of the outbursts in the  $W2$  band compared to  $WI$ , as shown in Equation 1:

$$\Delta W2 = (-0.2 \pm 0.1)\Delta WI^2 + (0.7 \pm 0.2)\Delta WI - (0.5 \pm 0.1) \quad (1)$$

The updated relation linking the increasing redness of a MIR outburst to an increasing  $W2$  luminosity is shown in Equation 2:

$$\Delta(WI - W2) = (-0.27 \pm 0.05)\Delta W2 + (0.15 \pm 0.07) \quad (2)$$

The addition of the TDE-ECLEs studied in this work to the sample from Clark et al. (2025) raises the statistical significance of the fit (when restricted to those objects with measurable values for both parameters), which now results in a Pearson's correlation coefficient of -0.86 and a p-value of 0.03. We note that formal statistical tests indicate that this relation is best fitted by a quadratic rather than a linear form, but this preference is due to the lack of constraining points at low and high values of  $\Delta W2$ . Such a fit is not supported by the overall dataset when those objects measured as limits are considered. A full statistical report of these fits is provided in Table E1. These relations are similar to the trend identified for the MIRONG sample by Jiang et al. (2021b), where again those object's showing larger outbursts in  $W2$  (i.e., more negative  $\Delta W2$  values) also displayed larger (i.e., redder)  $\Delta(WI - W2)$  values. A more in-depth exploration of the MIR behaviour of these and other similar transients is planned for a future work.

## 6.2 Rate estimation

The rate of TDE-ECLEs was initially estimated by Wang et al. (2012), assuming all seven of their ECLEs were linked to TDEs. Callow et al. (2024) re-searched the SDSS-Legacy dataset first searched by Wang et al. (2012) and conducted a complete rates analysis. Their ECLE rate, at a median redshift of  $\sim 0.1$ , was consistent with the low end of TDE rates and implied that 10–40 per cent of TDEs create ECLEs. This result was corroborated by Callow et al. (2025), who measured a similar ECLE rate based on a single variable ECLE discovered in the BOSS LOWZ survey at  $z \sim 0.3$ . Here, we use the three TDE-ECLEs described above and the detection efficiency measured in Section 3.3 to measure the ECLE rate at the DESI EDR median redshift of  $\sim 0.2$ .

### 6.2.1 Visibility time

In order to estimate the rate of ECLEs using our DESI EDR sample, we must first calculate the visibility time for each galaxy in the sample, which is the length of time an ECLE would be detectable at that galaxy's redshift. We do this using the method developed by Callow et al. (2024). This process starts with sampling a TDE peak X-ray luminosity from the Sazonov et al. (2021) luminosity function (LF), which is parameterized as

$$\frac{d\dot{N}}{d \log_{10} L} = \dot{N}_0 (L/L_0)^a, \quad (3)$$

where  $\dot{N}$  is the volumetric rate and  $L$  is the peak luminosity of the TDE. The constants are  $L_0 = 10^{43} \text{ erg s}^{-1}$ ,  $\dot{N}_0 = (1.4 \pm 0.8) \times 10^{-7} \text{ Mpc}^{-3} \text{ yr}^{-1}$ , and  $a = -0.6 \pm 0.2$ . As the LF gives the rate of

TDEs of a particular peak luminosity, we normalize it over the range of luminosities the LF was constructed over,  $10^{42.7} - 10^{44.9} \text{ erg s}^{-1}$ , to create a probability distribution.

We convert the peak luminosity to a peak coronal line strength using spectroscopic observations of the coronal line TDE, AT 2017gge (Onori et al. 2022; Callow et al. 2024). We require that the ratio between the peak coronal line strength,  $S_{\max}$ , and AT 2017gge's peak coronal line strength at 218 d post-discovery,  $S_{\text{gge}}$ , be equal to the ratio between the sampled peak luminosity and AT 2017gge's peak X-ray luminosity,  $L_{\text{gge}}$ , i.e.,

$$\frac{S_{\max}}{S_{\text{gge}}} = \frac{L_{\max}}{L_{\text{gge}}}. \quad (4)$$

The peak coronal line strength is then evolved over a period of 10 yr according to a power-law. The time period was selected as it was the length of time over which the coronal lines of the Wang et al. (2012) ECLEs faded, and a power-law was used as it is the predicted shape of a TDE light curve decline. The power-law index was sampled from the range of theoretical light curve indices,  $-5/12$  to  $-5/3$ . The strength curve is then redshifted according to the galaxy's redshift, which, due to cosmological time dilation, increases the time over which the coronal lines are visible.

The visibility time,  $t_v$ , for each galaxy is then:

$$t_v = \int \epsilon(S(t)) dt, \quad (5)$$

where  $\epsilon(S)$  is the detection efficiency as a function of coronal line strength measured in Section 3.3 and the integral runs over the full time over which the strength evolution is modelled.

### 6.2.2 Galaxy-normalized rate

The galaxy-normalized ECLE rate is

$$R_G = \frac{N_{\text{ECLE}}}{\sum_{i=1}^{N_g} t_{v,i}}, \quad (6)$$

where  $N_{\text{ECLE}}$  is the number of ECLEs detected,  $N_g$  is the number of galaxies searched over, and  $t_{v,i}$  is the visibility time of the  $i$ -th galaxy.

We detected three ECLEs in our EDR sample, which means that the errors on the resultant rate are dominated by the Poisson uncertainty on three detections,  $N = 3.0^{+2.9}_{-1.6}$ . In order to account for the statistical uncertainties on the parameters used in the total visibility time calculation, we conducted a Monte Carlo simulation by repeating the visibility time calculation 500 times and taking the peak of the resulting distribution of visibility times as the value used in the rate calculation. The  $1\sigma$  standard deviation of the distribution is then used as the error on the total visibility time. This results in a galaxy-normalized rate of  $R_G = 5^{+5}_{-3} \times 10^{-6} \text{ galaxy}^{-1} \text{ yr}^{-1}$ .

We add this rate to the galaxy-normalized rate vs. mass relation developed in Callow et al. (2024, 2025) at the mean stellar mass of EDR in Figure 29. This rate is consistent with the relation calculated using the rates from SDSS Legacy and BOSS LOWZ. The values of the parameters of the fit change to  $a = -0.7 \pm 0.3$  and  $b = 1.5^{+3.1}_{-3.5}$ , with a reduced  $\chi^2 = 0.14$ .

We caution that the  $\chi^2$  distribution used to determine the power-law fit parameters and confidence region is a biased estimator due to the inclusion of Poisson uncertainties stemming from the small number of ECLEs per bin. Hence, the errors on the parameters and the confidence region are likely underestimated. However, we note that the shape of the power-law fit and the theoretical TDE rate versus mass relation are still qualitatively consistent.

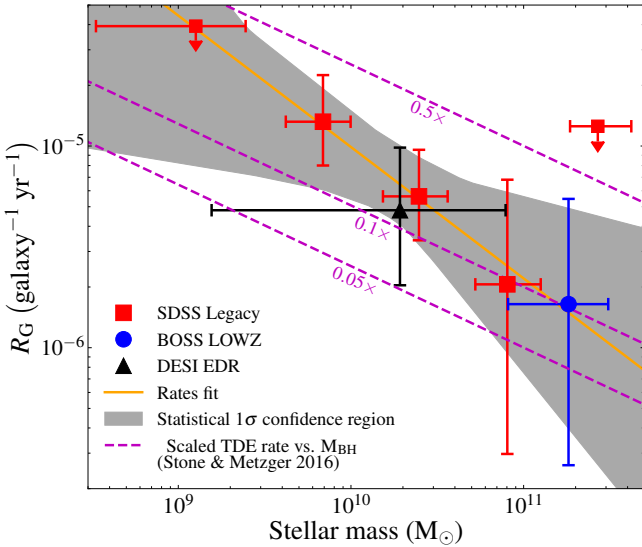


**Figure 29.** Galaxy-normalized ECLE rates as a function of galaxy stellar mass for SDSS Legacy (red squares), BOSS LOWZ (blue square) and DESI EDR (black square). Vertical error bars show the statistical errors on the rates derived using the Monte Carlo simulations detailed above; and the horizontal error bars denote the range within each mass bin that 68 per cent of the galaxies fall. The points marked with downward arrows are  $2\sigma$  upper bounds on the rates calculated using the upper Poisson error on zero detections. The solid orange line shows the power-law fit to the Legacy, LOWZ, and EDR rates and the shaded area is the  $1\sigma$  confidence region. The dashed purple line shows the TDE rate vs. black hole mass relation calculated by Stone & van Velzen (2016), scaled by 0.05, 0.1, and 0.5.

### 6.2.3 Mass-normalized rate

We calculate the mass-normalized rate by weighting each galaxy's visibility time by its stellar mass taken from the FASTSPECFit VAC. We perform the same Monte Carlo process of calculating the total visibility time 500 times and taking the peak of the distribution as the true value. This gives a mass-normalized rate of  $R_M = 1.1^{+1.2}_{-0.6} \times 10^{-16} M_\odot^{-1} \text{ yr}^{-1}$ . We add this rate to the mass-normalized rate vs. stellar mass relation from Callow et al. (2024, 2025) in Figure 30. The power-law fit of the form of produces values of  $a = -1.7^{+0.4}_{-0.3}$  and  $b = 2^{+3}_{-4}$ , with a reduced  $\chi^2 = 1.5$ . The resultant relation is consistent with the one measured using the SDSS Legacy and BOSS LOWZ samples.

We also investigate the relation between the mass-normalized ECLE rate and star-formation rates (SFR) and specific SFRs (sSFRs) of the galaxies in the sample to test whether they strengthen the tentative positive correlation between rate and sSFR found in Callow et al. (2025). This is shown in Figure 31. The mass-normalized rate continues to show no dependence on SFR, whereas the DESI EDR rate is consistent with the positive correlation with sSFR found previously. A likelihood ratio test continues to prefer a 1<sup>st</sup>-order polynomial over a 0<sup>th</sup>-order polynomial at a  $> 2\sigma$  confidence level. We also measure a Pearson r coefficient of 0.88 with a p-value of 0.047, indicating a hint of a correlation. More measurements at a higher precision are needed to claim statistical significance of this relation. The DESI ECLEs also lie in similar regions of the SFR/sSFR vs. stellar mass phase space as the previously discovered ECLEs. These results of no dependence on SFR and a possible correlation with sSFR are very similar to the relations found for SNe Ia by Graur et al. (2015). Those correlations were explained as a consequence

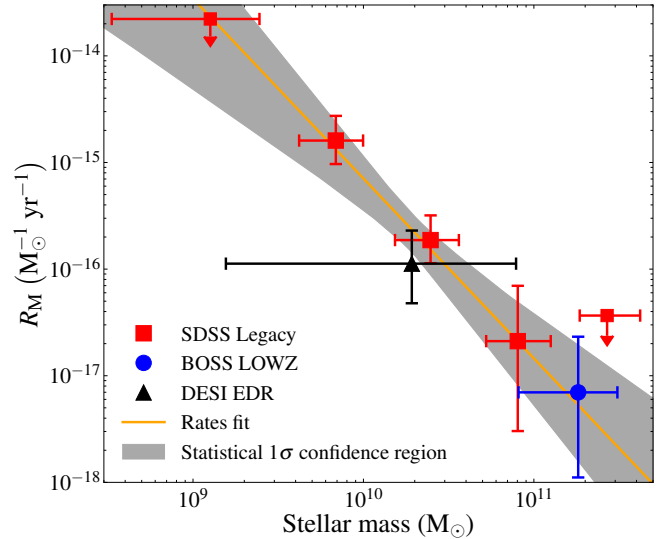


**Figure 30.** Mass-normalized ECLE rates as a function of galaxy stellar mass for SDSS Legacy (red squares), BOSS LOWZ (blue square) and DESI EDR (black square). Vertical error bars show the statistical errors on the rates derived using the Monte Carlo simulations detailed above; and the horizontal error bars denote the range within each mass bin that 68 per cent of the galaxies fall. The points marked with downward arrows are  $2\sigma$  upper bounds on the rates calculated using the upper Poisson error on zero detections. The solid orange line shows the power-law fit to the Legacy, LOWZ, and EDR rates and the shaded area is the  $1\sigma$  confidence region.

of the galaxy age-mass relation, in combination with the additional correlation between galaxy stellar mass and either SFR or sSFR, and the delay-time distribution of SNe Ia. Given the similarities between the relations in this work and Graur et al. (2015), future work may find a similar explanation is suitable for ECLEs and, by extension, TDEs.

### 6.2.4 Volumetric rate

We calculate the volumetric ECLE rate by multiplying the mass-normalized rate by the cosmic stellar mass density. This is calculated by integrating the galactic stellar mass function (GSMF), accounting for the mass distribution of EDR and the ECLE rate vs. stellar mass relation by including them both in the calculation. As the Baldry et al. (2012) GSMF has been shown to be valid out to  $z \sim 0.5$ , which covers the full redshift range of our EDR sample, we continue to use it for this calculation. The volumetric rate is then calculated to be  $R_V = 2.3^{+10.7}_{-1.6} \times 10^{-8} \text{ Mpc}^{-3} \text{ yr}^{-1}$ .

We also investigate the contribution of each source of uncertainty to the overall values by repeating the Monte Carlo simulations and varying each source of uncertainty individually. The resultant error budget is presented in Table 13. The total uncertainty percentages are the linear sum of the total statistical and systematic uncertainties divided by the corresponding rate value.

The positive uncertainty on the volumetric rate is proportionally much larger than the corresponding uncertainties on the galaxy- and mass-normalized rates. The uncertainty budget shows that the main contributing factor to this large uncertainty is the fit to the mass-normalised rate vs. galactic stellar mass trend. This is because the stellar masses of the SDSS Legacy ECLE host galaxies and the mean stellar masses of the BOSS LOWZ and DESI EDR samples are all within the range  $\sim 10^9 - 10^{11} M_\odot$ . Therefore, the fit to the trend

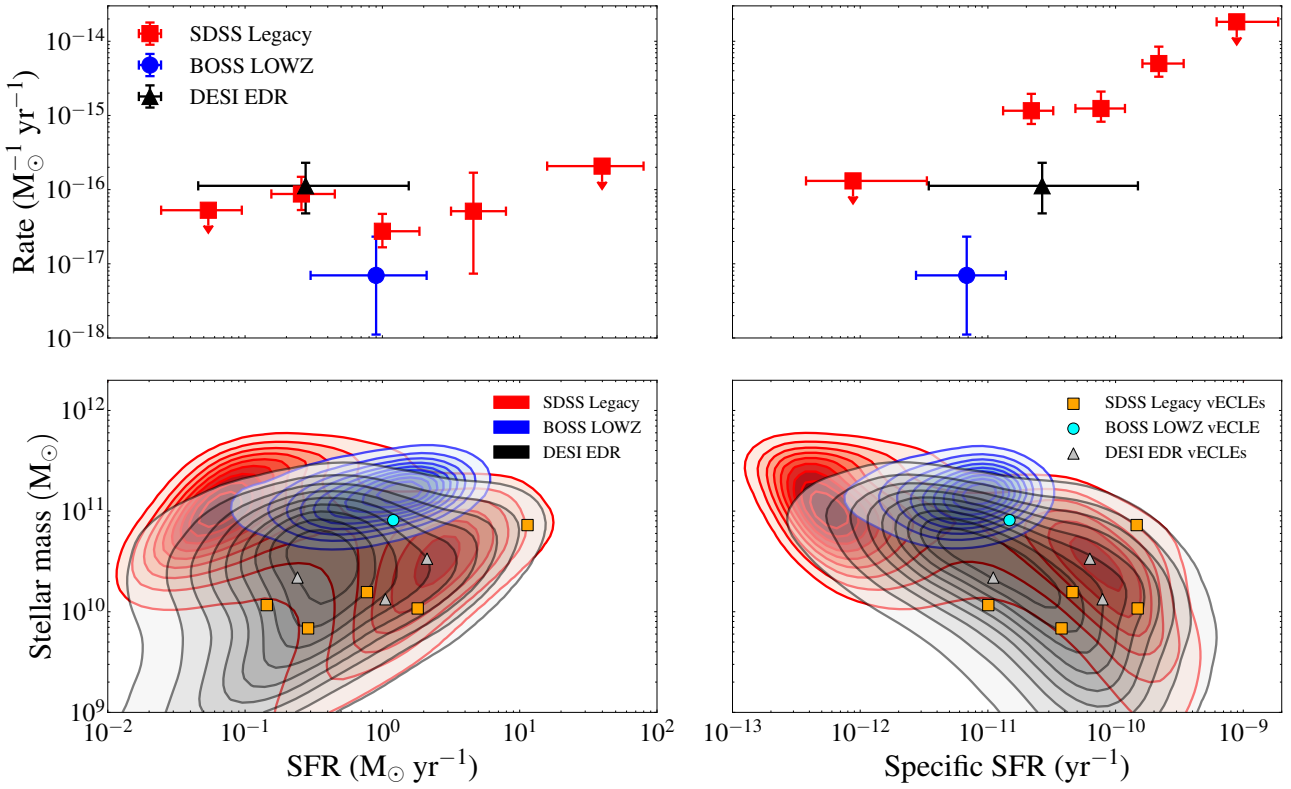


**Figure 31.** *Top:* Mass-normalized ECLE rates as a function of galaxy SFR (left) and sSFR (right) for SDSS Legacy (red squares), BOSS LOWZ (blue circle), and DESI EDR (black triangle). Vertical error bars show the statistical errors on the rates, while the horizontal error bars denote the SFR and sSFR ranges comprising 68 per cent of the galaxies in each bin. The points marked with downward arrows are  $2\sigma$  upper limits on the rates calculated using the upper Poisson error on zero detections. *Bottom:* Contours showing the density of galaxies in the SDSS Legacy (red), BOSS LOWZ (blue), and DESI EDR (black) samples in decrements of 10 per cent. The ECLEs detected in SDSS Legacy by Wang et al. (2012) and are shown as orange squares, the ECLE detected in BOSS LOWZ as a cyan circle, and the ECLEs detected in DESI EDR as grey triangles.

**Table 13.** ECLE rate uncertainty percentages.

Uncertainty	Percentage of rate
<b>Galaxy-normalized rate</b>	
Total	+104/-58
Statistical	
Poisson	+97/-54
AT 2017gge peak CrL strength	+3/-4
AT 2017gge peak luminosity	+31/-13
Range of power-law indices	+24/-14
<b>Mass-normalized rate</b>	
Total	+104/-58
Galaxy stellar masses	$\pm 1$
<b>Volumetric rate</b>	
Total	+593/-70
GSMF parameters	+174/-65
Rate mass trend fit	+490/-1

is best constrained in this range and the confidence region of the fit grows outside the range. DESI EDR contains galaxies with stellar masses down to  $\sim 10^7 M_\odot$ , well outside the well-constrained region. Calculating the volumetric rate requires integrating the rate-mass relation over the full mass range of the galaxy sample. Therefore, the large uncertainties in the rate-mass fit at the low stellar masses that DESI EDR contains propagate through to the volumetric rate uncertainties. A similar effect is seen in the SDSS Legacy volumetric rate uncertainties, although not to as great an extent, as SDSS Legacy did not contain as many lower-mass galaxies as DESI EDR.

#### 6.2.5 Comparison to previous rates

In Figure 32, we compare our galaxy-normalized and volumetric ECLE rates from SDSS Legacy, BOSS LOWZ, and DESI EDR to TDE rates from the literature (Donley et al. 2002; Esquej et al. 2008; Maksym et al. 2010; Khabibullin & Sazonov 2014; van Velzen & Farrar 2014; Holoi et al. 2016; Hung et al. 2018; van Velzen 2018; Sazonov et al. 2021; Lin et al. 2022; Yao et al. 2023; Masterson et al. 2024) and the ECLE rate estimated by Wang et al. (2012). The EDR ECLE galaxy-normalized rate is consistent with both the SDSS and BOSS rates, but is still roughly half an order of magnitude lower than the Wang et al. (2012) estimate (which counted two non-variable ECLEs among its seven objects). The volumetric rate from EDR is also consistent with the SDSS Legacy rate, but is higher than the BOSS LOWZ rate. Given that we control for the different surveys selecting galaxies in different mass regimes, this could be due to ECLE rates being lower at higher redshifts, aligning with theoretical work on the evolution of the TDE rate with redshift (Kochanek 2016). However, more precise rates at higher redshifts are required to check whether this is truly the case.

The galaxy-normalized rate is over an order of magnitude lower than the theoretical minimum TDE rate and all three ECLE rates are lower than all the observational TDE rates, strengthening our proposition that only a subset of TDEs produce CrLs. By comparing the EDR rates to the theoretical minimum TDE rate and the lowest observational galaxy-normalized and volumetric TDE rates, we can constrain the percentage of TDEs that create strong CrLs. The Wang

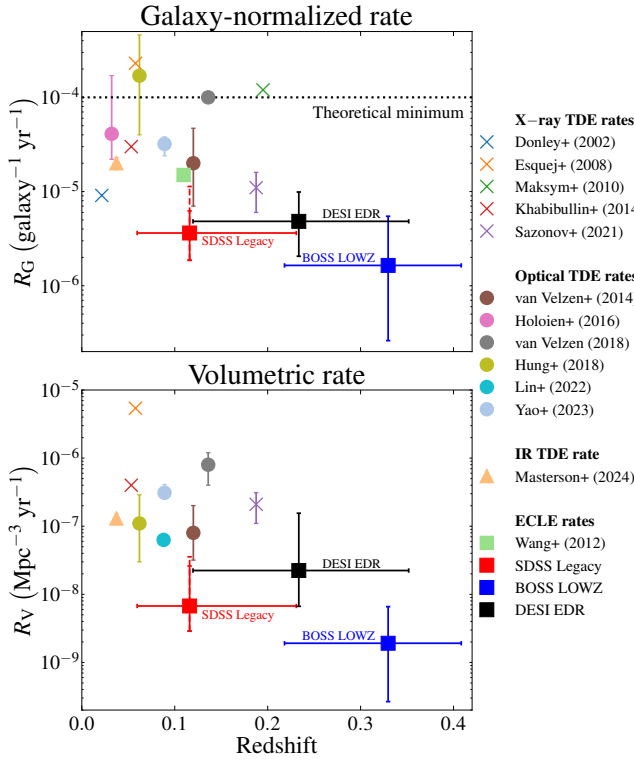


**Figure 32.** Comparisons of our galaxy-normalized (left) and volumetric (right) ECLE rates with TDE and ECLE rates from the literature. TDE rates derived from X-ray surveys are shown as crosses (Donley et al. 2002; Esquej et al. 2008; Maksym et al. 2010; Khabibullin & Sazonov 2014; Sazonov et al. 2021), those from optical/UV surveys are shown as circles (van Velzen & Farrar 2014; Holoiien et al. 2016; van Velzen 2018; Hung et al. 2018; Lin et al. 2022; Yao et al. 2023), and IR surveys are shown as triangles (Masterson et al. 2024). Our previous SDSS Legacy (Callow et al. 2024) and BOSS LOWZ (Callow et al. 2025) ECLE rates are shown as red and blue squares, respectively, while the Wang et al. (2012) over-estimated galaxy-normalised ECLE rate is shown in green. Error bars are shown if available. The statistical errors of our ECLE rates are denoted by the solid error bars and the systematic errors by the dashed error bars. The horizontal error bars show the range of redshifts spanned by 68 per cent of the galaxies in the spectroscopic samples used. The dotted horizontal line marks the theoretical minimum TDE rate calculated by Wang & Merritt (2004).

& Merritt (2004) theoretical minimum gives  $5^{+5}_{-3}$  per cent, whereas the galaxy normalized rate from Donley et al. (2002) gives  $50^{+50}_{-30}$  per cent, and the volumetric rate from Lin et al. (2022) gives  $36^{+64}_{-25}$  per cent. All of these ratios are consistent with the values calculated using the SDSS and BOSS rates with the conclusion that roughly 5 – 50 per cent of TDEs result in the creation of ECLEs. However, these ratios are calculated under the assumption that all ECLEs are the result of TDEs. If other transients are able to create strong, variable CrLs, then the ratio of TDEs that produce CrLs would be lower. Komossa & Grupe (2024) investigated extreme AGN flares, a subset of which can appear similar to TDEs with a large increase in X-ray luminosity that fades over the following months to years. They discuss two such flares that also developed CrLs, which then continued to vary or fade. However, it is unclear whether these flares were the result of variability of the AGN itself or due to a TDE occurring in the AGN. Another possible example of this is the transient AT 2019aalc, which showed strong transient CrLs similar to those in this work and CrL-TDEs (Milán Veres et al. 2024). It has been

classified as a Bowen fluorescence flare (a type of AGN flare) due to Bowen fluorescence lines in the transient spectrum and an AGN-like pre-transient spectrum. Again, the progenitor of this flare is not understood, so it is possible that AT 2019aalc is a TDE occurring in an AGN. Given these examples, it is possible that not all ECLEs are created by TDEs, and so the ratios calculated in this work can be considered as upper limits on the true values.

## 7 CONCLUSIONS

In this work we conducted a search for new ECLEs within DESI's EDR, with a focus on identifying those linked to the occurrence of TDEs. We have described the details of the search, including the custom python code (SLEIPNIR) used to perform the search, highlighting the primary sources of potential contamination in similar analyses and how these can be mitigated.

Our search of DESI EDR has identified a total of 208 galaxies displaying Fe CrLs. Using archival and follow-up imaging and spectroscopy in the optical, NIR, and MIR, we have classified three of these ECLEs as being linked to TDEs (i.e., TDE-ECLEs). The other 205 found to be consistent with AGN activity.

Based on the identification of these objects, we have been able to add further strengthen the claim made by Clark et al. (2025) that TDEs displaying MIR outbursts show a colour-luminosity relationship in their MIR evolution. Specifically, objects with brighter MIR flares show more significant reddening at outburst. We also calculate the rates of TDE-linked ECLEs at the DESI median redshift of 0.2, finding a galaxy-normalized rate of  $R_G = 5^{+5}_{-3} \times 10^{-6}$  galaxy $^{-1}$  yr $^{-1}$ , a mass-normalized rate of  $R_M = 1.1^{+1.2}_{-0.6} \times 10^{-16}$  M $_{\odot}^{-1}$  yr $^{-1}$ , and a volumetric rate of  $R_V = 2.3^{+10.7}_{-1.6} \times 10^{-8}$  Mpc $^{-3}$  yr $^{-1}$ . These rates are consistent with those measured for other surveys. More precise rates, such as those that could be measured from an ECLE survey of the complete DESI sample, are required to ascertain whether TDE-ECLE rates decline with redshift, as predicted by Callow et al. (2025) under the assumption that TDEs are the dominant source of variable extragalactic coronal lines and following previous studies that TDE rates generally decrease with increasing redshift. Based on the number of TDE-ECLEs discovered in DESI EDR and the rates measured here, we expect the full DESI survey to yield  $\sim 35$ – $50$  new TDE-ECLEs.

The search has also revealed more than 200 AGNs that display CrLs, which given their nature as the primary astrophysical contaminant in ECLE searches will serve as an important reference for future work in screening them from TDE samples. This work also highlights the necessity for long-term, multi-wavelength follow-up of nuclear transients on a years-long timescale.

## ACKNOWLEDGEMENTS

PC was supported by the Science & Technology Facilities Council grant ST/Y001850/1. OG and PC were also supported by the Science & Technology Facilities Council [grant numbers ST/S000550/1 and ST/W001225/1].

The authors would like to thank Yi Yang for their role in obtaining and processing the follow-up Keck spectra used in this work.

This material is based upon work supported by the U.S. Department of Energy (DOE), Office of Science, Office of High Energy Physics, under Contract No. DE-AC02-05CH11231, and by the National Energy Research Scientific Computing Center, a DOE Office

of Science User Facility under the same contract. Additional support for DESI was provided by the U.S. National Science Foundation (NSF), Division of Astronomical Sciences under Contract No. AST-0950945 to the NSF's National Optical Infrared Astronomy Research Laboratory; the Science and Technology Facilities Council of the United Kingdom; the Gordon and Betty Moore Foundation; the Heising-Simons Foundation; the French Alternative Energies and Atomic Energy Commission (CEA); the National Council of Humanities, Science and Technology of Mexico (CONAHCYT); the Ministry of Science, Innovation and Universities of Spain (MICIU/AEI/10.13039/501100011033), and by the DESI Member Institutions: <https://www.desi.lbl.gov/> collaborating-institutions. Any opinions, findings, and conclusions or recommendations expressed in this material are those of the author(s) and do not necessarily reflect the views of the U. S. National Science Foundation, the U. S. Department of Energy, or any of the listed funding agencies. The authors are honored to be permitted to conduct scientific research on I'oligam Du'ag (Kitt Peak), a mountain with particular significance to the Tohono O'odham Nation.

The Liverpool Telescope is operated on the island of La Palma by Liverpool John Moores University in the Spanish Observatorio del Roque de los Muchachos of the Instituto de Astrofísica de Canarias with financial support from the UK STFC (Project IDs: PL22A04, PL22B03, PL23A03, PL23B07, PL24A13, PL24B03 and PL25A01, PI: P. Clark).

Several spectra presented in this work were obtained with ALFOSC, which is provided by the Instituto de Astrofísica de Andalucía (IAA) under a joint agreement with the University of Copenhagen and NOT (Proposal ID: 70-108, PI: P.Clark).

The DESI Legacy Imaging Surveys consist of three individual and complementary projects: the Dark Energy Camera Legacy Survey (DECaLS), the Beijing-Arizona Sky Survey (BASS), and the Mayall z-band Legacy Survey (MzLS). DECaLS, BASS and MzLS together include data obtained, respectively, at the Blanco telescope, Cerro Tololo Inter-American Observatory, NSF's NOIRLab; the Bok telescope, Steward Observatory, University of Arizona; and the Mayall telescope, Kitt Peak National Observatory, NOIRLab. NOIRLab is operated by the Association of Universities for Research in Astronomy (AURA) under a cooperative agreement with the National Science Foundation. Pipeline processing and analyses of the data were supported by NOIRLab and the Lawrence Berkeley National Laboratory (LBNL). Legacy Surveys also uses data products from the Near-Earth Object Wide-field Infrared Survey Explorer (NEOWISE), a project of the Jet Propulsion Laboratory/California Institute of Technology, funded by the National Aeronautics and Space Administration. Legacy Surveys was supported by: the Director, Office of Science, Office of High Energy Physics of the U.S. Department of Energy; the National Energy Research Scientific Computing Center, a DOE Office of Science User Facility; the U.S. National Science Foundation, Division of Astronomical Sciences; the National Astronomical Observatories of China, the Chinese Academy of Sciences and the Chinese National Natural Science Foundation. LBNL is managed by the Regents of the University of California under contract to the U.S. Department of Energy. The complete acknowledgments can be found at <https://www.legacysurvey.org/acknowledgment/>.

This research has made use of the VizieR catalogue access tool, CDS, Strasbourg Astronomical Observatory, France (DOI : [10.26093/cds/vizier](https://doi.org/10.26093/cds/vizier)).

NOIRLab IRAF is distributed by the Community Science and Data Center at NSF NOIRLab, which is managed by the Association of Universities for Research in Astronomy (AURA) under a cooperative agreement with the U.S. National Science Foundation.

## DATA AVAILABILITY

The data underlying this work are available in the article and in its online supplementary material available through Zenodo ([Clark et al. 2026](#)).

Additionally, all DESI spectra utilised in this work are part of the public 'Early Data Release'. Details of which, and how to access the data itself, can be found within [DESI Collaboration et al. \(2024e\)](#) and through the DESI data [website](#). The public version of the SLEIPNIR code will be released through [GitHub](#) upon this work's publication.

## REFERENCES

Abazajian K. N., et al., 2009, *ApJS*, 182, 543  
 Abdurro'uf et al., 2022, *ApJS*, 259, 35  
 Ahumada R., et al., 2020, *ApJS*, 249, 3  
 Almeida A., et al., 2023, *ApJS*, 267, 44  
 Arcavi I., 2018, Transient Name Server Classification Report, 2018–1764, 1  
 Auchettl K., Guillochon J., Ramirez-Ruiz E., 2017, *ApJ*, 838, 149  
 Auchettl K., Ramirez-Ruiz E., Guillochon J., 2018, *ApJ*, 852, 37  
 Ayal S., Livio M., Piran T., 2000, *ApJ*, 545, 772  
 Bach Y. P., 2023, ysBach/Ysfitsutilpy: V0.2, Zenodo, [doi:10.5281/zenodo.7639489](https://doi.org/10.5281/zenodo.7639489)  
 Baldry I. K., et al., 2012, *MNRAS*, 421, 621  
 Baldwin J. A., Phillips M. M., Terlevich R., 1981, *PASP*, 93, 5  
 Becker R. H., White R. L., Helfand D. J., 1995, *ApJ*, 450, 559  
 Bellm E. C., et al., 2019, *PASP*, 131, 18002  
 Best P. N., Kauffmann G., Heckman T. M., Brinchmann J., Charlton S., Ivezic Ž., White S. D. M., 2005, *MNRAS*, 362, 25  
 BiÉmont E., FrÉmat Y., Quinet P., 1999, *Atomic Data and Nuclear Data Tables*, 71, 117  
 Brennan S. J., Fraser M., 2022, *A&A*, 667, A62  
 Callow J., et al., 2024, *MNRAS*, 535, 1095  
 Callow J., et al., 2025, *MNRAS*, 539, 231  
 Chabrier G., 2003, *PASP*, 115, 763  
 Clark P., et al., 2024, *MNRAS*, 528, 7076  
 Clark P., et al., 2025, *MNRAS*, 540, 871  
 Clark P., Callow J., Graur O., Al E., 2026, Zenodo  
 DESI Collaboration et al., 2016a, The DESI Experiment Part I: Science, Targeting, and Survey Design, [doi:10.48550/arXiv.1611.00036](https://doi.org/10.48550/arXiv.1611.00036)  
 DESI Collaboration et al., 2016b, The DESI Experiment Part II: Instrument Design, [doi:10.48550/arXiv.1611.00037](https://doi.org/10.48550/arXiv.1611.00037)  
 DESI Collaboration et al., 2022, *AJ*, 164, 207  
 DESI Collaboration et al., 2024a, DESI 2024 II: Sample Definitions, Characteristics, and Two-point Clustering Statistics, [doi:10.48550/arXiv.2411.12020](https://doi.org/10.48550/arXiv.2411.12020)  
 DESI Collaboration et al., 2024b, DESI 2024 V: Full-Shape Galaxy Clustering from Galaxies and Quasars, [doi:10.48550/arXiv.2411.12021](https://doi.org/10.48550/arXiv.2411.12021)  
 DESI Collaboration et al., 2024c, DESI 2024 VII: Cosmological Constraints from the Full-Shape Modeling of Clustering Measurements, [doi:10.48550/arXiv.2411.12022](https://doi.org/10.48550/arXiv.2411.12022)  
 DESI Collaboration et al., 2024d, *AJ*, 167, 62  
 DESI Collaboration et al., 2024e, *AJ*, 168, 58  
 DESI Collaboration et al., 2025a, Data Release 1 of the Dark Energy Spectroscopic Instrument ([arXiv:2503.14745](https://arxiv.org/abs/2503.14745)), [doi:10.48550/arXiv.2503.14745](https://doi.org/10.48550/arXiv.2503.14745)  
 DESI Collaboration et al., 2025b, *Phys. Rev. D*, 112, 083515  
 DESI Collaboration et al., 2025c, *JCAP*, 2025, 012  
 DESI Collaboration et al., 2025d, *JCAP*, 2025, 021  
 DESI Collaboration et al., 2025e, *JCAP*, 2025, 124  
 Dawson K. S., et al., 2013, *AJ*, 145, 10  
 Dey A., et al., 2019, *AJ*, 157, 168  
 Ding W., Kong W., Sui J., Yao Y., Lin Z., Guo W.-J., Zou H., 2025, *ApJ*, 988, 187  
 Dodd S. A., Nukala A., Connor I., Auchettl K., French K. D., Law-Smith J. A. P., Hammerstein E., Ramirez-Ruiz E., 2023, *ApJ*, 959, L19

Donley J. L., Brandt W. N., Eracleous M., Boller Th., 2002, *AJ*, 124, 1308  
 Dou L., Wang T.-g., Jiang N., Yang C., Lyu J., Zhou H., 2016, *ApJ*, 832, 188  
 Esquej P., et al., 2008, *A&A*, 489, 543  
 Evans C. R., Kochanek C. S., 1989, *ApJ*, 346, L13  
 Eyles-Ferris R. A. J., Starling R. L. C., O'Brien P. T., Page K. L., Evans P. A., 2025, Nine Tidal Disruption Event Candidates in eROSITA-DE DR1 Discovered through Supersoft X-ray Selection ([arXiv:2508.08389](https://arxiv.org/abs/2508.08389)), doi:[10.48550/arXiv.2508.08389](https://doi.org/10.48550/arXiv.2508.08389)  
 Filippenko A. V., 1982, *PASP*, 94, 715  
 Fitzpatrick E. L., 1999, *PASP*, 111, 63  
 Fitzpatrick M., Placco V., Bolton A., Merino B., Ridgway S., Stanghellini L., 2024, Modernizing IRAF to Support Gemini Data Reduction, doi:[10.48550/arXiv.2401.01982](https://doi.org/10.48550/arXiv.2401.01982)  
 Flesch E. W., 2023, *OJAp*, 6, 49  
 Fraser M., et al., 2017, The Astronomer's Telegram, 10747, 1  
 Frederick S., et al., 2019, *ApJ*, 883, 31  
 Gezari S., et al., 2006, *ApJ*, 653, L25  
 Gharaibeh M. F., et al., 2011, *Phys. Rev. A*, 83, 043412  
 Giustini M., Miniutti G., Saxton R. D., 2020, *A&A*, 636, L2  
 Gomez S., et al., 2020, *MNRAS*, 497, 1925  
 Gordon Y. A., et al., 2021a, *VizieR Online Data Catalog*, 225, J/ApJS/255/30  
 Gordon Y. A., et al., 2021b, *ApJS*, 255, 30  
 Graur O., Bianco F. B., Modjaz M., 2015, *MNRAS*, 450, 905  
 Green D., et al., 2025, Using Active Learning to Improve Quasar Identification for the DESI Spectra Processing Pipeline ([arXiv:2505.01596](https://arxiv.org/abs/2505.01596)), doi:[10.48550/arXiv.2505.01596](https://doi.org/10.48550/arXiv.2505.01596)  
 Greiner J., Schwarz R., Zharikov S., Orio M., 2000, RX J1420.4+5334 - Another Tidal Disruption Event?, doi:[10.48550/arXiv.astro-ph/0009430](https://doi.org/10.48550/arXiv.astro-ph/0009430)  
 Grotova I., et al., 2025, The Population of Tidal Disruption Events Discovered with eROSITA, doi:[10.48550/arXiv.2504.08424](https://doi.org/10.48550/arXiv.2504.08424)  
 Guy J., et al., 2023, *AJ*, 165, 144  
 Hall X. J., et al., 2025, Transient Name Server Discovery Report, 2025–1549, 1  
 Hammerstein E., Yao Y., Gezari S., Velzen S. V., Somalwar J., Kulkarni S., 2021, Transient Name Server Classification Report, 2021–1723, 1  
 Hammerstein E., et al., 2023, *ApJ*, 942, 9  
 Hills J. G., 1975, *Nature*, 254, 295  
 Hinkle J. T., 2024, *MNRAS*, 531, 2603  
 Hinkle J. T., Shappee B. J., Hololen T. W. S., 2024, *MNRAS*, 528, 4775  
 Hololen T. W. S., et al., 2016, *MNRAS*, 463, 3813  
 Hook I. M., Jørgensen I., Allington-Smith J. R., Davies R. L., Metcalfe N., Murowinski R. G., Crampton D., 2004, *PASP*, 116, 425  
 Hung T., et al., 2018, *ApJS*, 238, 15  
 Hyland A. R., Allen D. A., 1982, *MNRAS*, 199, 943  
 Jiang N., Pan Z., 2025, *ApJL*, 983, L18  
 Jiang N., et al., 2021a, *ApJS*, 252, 32  
 Jiang N., Wang T., Hu X., Sun L., Dou L., Xiao L., 2021b, *ApJ*, 911, 31  
 Juneau S., et al., 2025, *AJ*, 169, 157  
 Khabibullin I., Sazonov S., 2014, *MNRAS*, 444, 1041  
 Kochanek C. S., 2016, *MNRAS*, 458, 127  
 Komossa S., Grupe D., 2024, *Serbian Astronomical Journal*, 209, 1  
 Komossa S., et al., 2008, *ApJ*, 678, L13  
 Komossa S., et al., 2009, *AJ*, 701, 105  
 Kramida A., Ralchenko Y., 2024, NIST Atomic Spectra Database, NIST Standard Reference Database 78, doi:[10.18434/T4W30F](https://doi.org/10.18434/T4W30F)  
 Kramida A., Bastin T., Biémont E., Dumont P.-D., Garnir H.-P., 1999, *Eur. Phys. J. D*, 7, 525  
 Krogager J.-K., 2025, PyNOT-redux: Data Reduction Pipeline for NOT/ALFOSC  
 Kynoch D., Landt H., Dehghanian M., Ward M. J., Ferland G. J., 2022, *MNRAS*, 516, 4397  
 Labrie K., Anderson K., Cárdenes R., Simpson C., Turner J. E. H., 2019, in Astronomical Data Analysis Software and Systems XXVII. p. 321  
 Lacy J. H., Townes C. H., Hollenbach D. J., 1982, *ApJ*, 262, 120  
 Lacy M., et al., 2020, *PASP*, 132, 035001  
 Lin Z., Jiang N., Kong X., Huang S., Lin Z., Zhu J., Wang Y., 2022, *ApJL*, 939, L33  
 Mainzer A., et al., 2011, *ApJ*, 743, 156  
 Mainzer A., et al., 2014, *ApJ*, 792, 30  
 Maksym W. P., Ulmer M. P., Eracleous M., 2010, *ApJ*, 722, 1035  
 Masci F. J., et al., 2023, A New Forced Photometry Service for the Zwicky Transient Facility, doi:[10.48550/arXiv.2305.16279](https://doi.org/10.48550/arXiv.2305.16279)  
 Masterson M., et al., 2024, *ApJ*, 961, 211  
 Mateos S., et al., 2012, *MNRAS*, 426, 3271  
 Milán Veres P., et al., 2024, Back from the Dead: AT2019aalc as a Candidate Repeating TDE in an AGN, doi:[10.48550/arXiv.2408.17419](https://doi.org/10.48550/arXiv.2408.17419)  
 Miller T. N., et al., 2024, *AJ*, 168, 95  
 Moffat A. F. J., 1969, *A&A*, 3, 455  
 Moustakas J., Buhler J., Scholte D., Dey B., Khederlarian A., 2023, Astrophysics Source Code Library, p. ascl:2308.005  
 Nagao T., Taniguchi Y., Murayama T., 2000, *AJ*, 119, 2605  
 Neustadt J. M. M., et al., 2020, *MNRAS*, 494, 2538  
 Newsome M., Arcavi I., Dgany Y., Pellegrino C., 2022, Transient Name Server AstroNote, 236, 1  
 Ochsenebein F., Bauer P., Marcout J., 2000, *ApJS*, 143, 23  
 Oke J. B., et al., 1995, *PASP*, 107, 375  
 Onori F., et al., 2022, *MNRAS*, 517, 76  
 Perley D. A., 2019, *PASP*, 131, 084503  
 Phinney E. S., 1989, *Nature*, 340, 595  
 Poppett C., et al., 2024, *AJ*, 168, 245  
 Qin Y.-J., et al., 2022, *ApJS*, 259, 13  
 Rees M. J., 1988, *Nature*, 333, 523  
 Reines A. E., Volonteri M., 2015, *ApJ*, 813, 82  
 Sazonov S., et al., 2021, *MNRAS*, 508, 3820  
 Schlafly E. F., Finkbeiner D. P., 2011, *ApJ*, 737, 103  
 Schlafly E. F., et al., 2023, *AJ*, 166, 259  
 Shimwell T. W., et al., 2022, *A&A*, 659, A1  
 Shingles L., et al., 2021, Transient Name Server AstroNote, 7, 1  
 Short P., et al., 2020, *MNRAS*, 498, 4119  
 Skrutskie M. F., et al., 2006, *AJ*, 131, 1163  
 Steele I. A., et al., 2004, in Oschmann Jacobus M. Jr., ed., Ground-Based Telescopes Vol. 5489, SPIE 5489. International Society for Optics and Photonics, pp 679–679, doi:[10.1117/12.551456](https://doi.org/10.1117/12.551456)  
 Stern D., et al., 2012, *ApJ*, 753, 30  
 Stone N. C., van Velzen S., 2016, *ApJ*, 825, L14  
 Sugar J., Corliss C., 1985, Technical Report PB-86-165446/XAB, Atomic Energy Levels of the Iron-Period Elements: Potassium through Nickel. American Chemical Society, Washington, DC  
 Tody D., 1986, *Instrumentation in Astronomy VI*, 627, 733  
 Tody D., 1993, Astronomical Data Analysis Software and Systems II, 52  
 Tonry J. L., et al., 2018, *PASP*, 130, 64505  
 Ulmer A., 1999, *ApJ*, 514, 180  
 Wang J., Merritt D., 2004, *ApJ*, 600, 149  
 Wang T.-G., Zhou H.-Y., Wang L.-F., Lu H.-L., Xu D., 2011, *ApJ*, 740, 85  
 Wang T.-G., Zhou H.-Y., Komossa S., Wang H.-Y., Yuan W., Yang C., 2012, *ApJ*, 749, 115  
 Wang Y., et al., 2022, *ApJS*, 258, 21  
 Wang Y., et al., 2024, *ApJ*, 966, 136  
 Wiseman P., et al., 2025, *MNRAS*, 537, 2024  
 Wright E. L., et al., 2010, *AJ*, 140, 1868  
 Yang C.-W., Wang T.-G., Ferland G., Yuan W., Zhou H.-Y., Jiang P., 2013, *ApJ*, 774, 46  
 Yao Y., et al., 2023, *ApJL*, 955, L6  
 Yao Y., Chornock R., Guo X., LeBaron N., Margutti R., Ravi V., Somalwar J., 2024, Transient Name Server AstroNote, 177, 1  
 Yao Y., Ye J., Sun L., Jiang N., Masterson M., Shu X., 2025, Distinguishing Tidal Disruption Events and Changing-look Active Galactic Nuclei via Variation of Mid-infrared Color ([arXiv:2503.10053](https://arxiv.org/abs/2503.10053)), doi:[10.48550/arXiv.2503.10053](https://doi.org/10.48550/arXiv.2503.10053)  
 York D. G., et al., 2000, *AJ*, 120, 1579  
 Young D., 2024, Plot\_atlas\_fp.Py, Zenodo, doi:[10.5281/zenodo.1097896](https://doi.org/10.5281/zenodo.1097896)  
 van Velzen S., 2018, *ApJ*, 852, 72  
 van Velzen S., Farrar G. R., 2014, *ApJ*, 792, 53

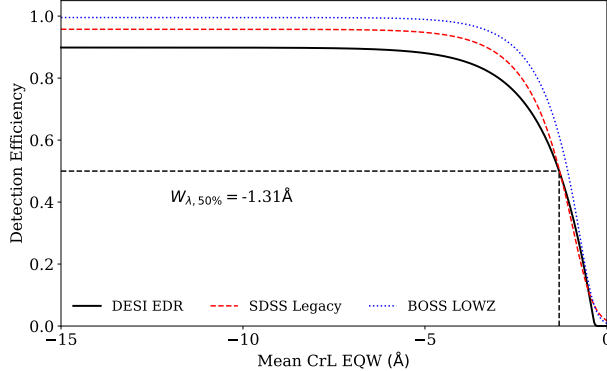


**Figure B1.** SLEIPNIR detection efficiency as a function of the average equivalent width of the coronal lines for DESI EDR and the comparison SDSS Legacy and BOSS LOWZ galaxy samples (Callow et al. 2024, 2025). Curves are generalized sigmoid fits to the underlying distributions.

## APPENDIX A: FASTSPECFIT VALUE ADDED CATALOGUE INFORMATION

In this appendix we outline the specific parameters retrieved from the FASTSPECFIT VAC used in this work for our comparative host galaxy analysis.

## APPENDIX B: DETECTION EFFICIENCY COMPARISON

Here we show the comparative performance of SLEIPNIR when deployed on the DESI EDR sample compared to the SDSS Legacy and BOSS LOWZ samples used in Callow et al. (2024) and Callow et al. (2025) respectively.

## APPENDIX C: DETAILED CROSMATCHING RESULTS

Here we provide the full results of the sample crossmatching as described in Section C.

### C1 TNS crossmatch

We first provide the full results of the crossmatch between the SLEIPNIR Input Galaxy Sample and the TNS database in Table C1. A total of 1,219 crossmatches were obtained, of which six are within our final EDR CrL Object Sample classified as CrL-AGN. This crossmatch was completed against the full public TNS database as of 2025 August 28.

### C2 Literature nuclear transient crossmatch

Next, in Table C2 provide the full results of the crossmatch between the SLEIPNIR Input Galaxy Sample and our expanded database of nuclear transients. A total of 11 crossmatches were obtained. None of these nuclear transients were seen to display CrLs in their DESI EDR spectra.

### C3 SDSS crossmatches

Here we describe the full results of the crossmatches conducted between the SLEIPNIR Input Galaxy Sample and the samples of

CrL galaxies constructed from the previous uses of SLEIPNIR on SDSS data.

As described in Section 4.3.3, 18 crossmatches were obtained between the SLEIPNIR Input Galaxy Sample and the CrL object sample of Callow et al. (2024), five of which are in the EDR CrL Object Sample. Two of these objects failed to meet the CrL strength cut relative to  $[\text{O III}] \lambda 5007 \text{Å}$  used in the Callow et al. (2024) analysis (20 per cent) to trigger visual inspection. The remaining three were rejected as false detections following visual inspection of the SDSS spectra primarily due to the weakness of the CrL features. The higher SNR of the DESI spectra of these objects allowed the CrL features to be reassessed as real in following the classification process in this work.

Of the remaining 13 objects that were not flagged in the initial DESI EDR analysis (i.e., not part of the EDR CrL Object Sample), ten had failed to meet the requirements for visual inspection in the search of the SDSS Legacy sample, with the remaining three being discarded as false positive detections following visual inspection. Following visual inspection of the DESI spectra of all thirteen galaxies, 11 were confirmed to be non-CrL hosting galaxies, with the remaining two being likely AGN with weak  $[\text{Fe VII}]$  emission that was insufficient to trigger automatic SLEIPNIR flagging alone, these being DESI 39628465170813469 and DESI 39633362041702102. Of these, DESI 39628465170813469 failed to meet the CrL strength requirements in the SDSS Legacy search whilst DESI 39633362041702102 was discarded as a false positive following visual inspection by Callow et al. (2025).

The full crossmatch to the BOSS LOWZ CrL sample from Callow et al. (2025) returned seven objects. Of these, six were identified as being skyline contaminated false positive detections with the final object (SDSS J113104.36+531338.8) not meeting the CrL strength threshold to trigger visual inspection. Visual inspection of both the DESI spectrum (which was not flagged by SLEIPNIR) and the BOSS LOWZ spectrum reveal this to be a low SNR false positive. No objects within the DESI EDR CrL sample were crossmatched to the BOSS LOWZ CrL sample - unsurprising given the small number of matches overall.

## C4 MILLIQUAS crossmatch

Table C5 outlines the full results of the crossmatch between the SLEIPNIR Input Galaxy Sample and the MILLIQUAS AGN database (Flesch 2023). We remind the reader that some MILLIQUAS classifications have been made using DESI spectra so these datasets are not fully independent. A total of 7154 crossmatches were returned. Of the subset flagged by SLEIPNIR for visual inspection and 163 have been determined to show real CrL emission, with the remaining identified as being the result of false positive contamination.

## C5 Ding et al. (2025) crossmatch

Table C6 outlines the full results of the crossmatch between the SLEIPNIR Input Galaxy Sample and the independent sample of CrL objects within DESI EDR identified by Ding et al. (2025).

## APPENDIX D: CORONAL LINE AGN

In addition to the six objects initially as potential TDE-ECLE candidates, the SLEIPNIR classification analysis identified a further 201

**Table A1.** Parameters retrieved from the FASTSPECFit EDR VAC. Parameter descriptions from the FASTSPECFit documentation.<sup>1</sup> Version used: v3.2

Parameter	Description
TARGETID	DESI Target ID
Z	Recorded redshift <sup>2</sup>
ZWARN	REDROCK redshift warning bit
SFR	Instantaneous star formation rate (h=1.0, <a href="#">Chabrier (2003)</a> initial mass function)
LOGMSTAR	Logarithmic stellar mass (h=1.0, <a href="#">Chabrier (2003)</a> initial mass function).
LOGMSTAR_IVAR	Inverse variance of LOGMSTAR.

Notes: <sup>1</sup> Documentation available here <https://fastspecfit.readthedocs.io/en/latest/fastspec.html>

<sup>2</sup> Obtained from REDROCK, or from QUASARNET ([Green et al. 2025](#)) for QSO targets

**Table C1.** The results of the TNS crossmatch to the SLEIPNIR Input Galaxy Sample. Crossmatch performed on the full TNS database as of 2025 August 28. A small portion of the table is included here for guidance of form. The full machine readable version is included in the supplementary material.

DESI ID	CrL Classification	TNS Name	TNS Classification
39633453855017885	CrL-AGN	AT 2021yje	None
39633304189666247	CrL-AGN	AT 2019jw	None
39633300653869008	CrL-AGN	AT 2021lar	None
39628506220463012	CrL-AGN	AT 2018mer	None
39627782338120416	CrL-AGN	AT 2021mks	None
...	...	...	

**Table C2.** Crossmatch results between the full SLEIPNIR Input Galaxy Sample and a literature sourced database of TDEs and other nuclear transients. No crossmatched object displayed coronal lines in its DESI EDR spectrum / spectra.

DESI ID	Object Name	Classification	Classification Source
39633451355212798	AT 2019baf	TDE	<a href="#">Yao et al. (2023)</a>
39633342957617640	AT 2019mha	TDE	<a href="#">Hammerstein et al. (2023)</a>
39633290046475104	GALEX D3-13	TDE	<a href="#">Gezari et al. (2006)</a>
39627793834706352	J121116	TDE	<a href="#">Qin et al. (2022)</a>
39633390168704930	J123715	TDE	<a href="#">Qin et al. (2022)</a>
39633300964248835	RX J1420.4+5334	TDE	<a href="#">Greiner et al. (2000)</a>
39628433277325770	RX J1301.9+2747	QPE	<a href="#">Giustini et al. (2020)</a>
39627835576422677	SDSS J100350.97+020227.6	TDE	<a href="#">Jiang et al. (2021a); Wang et al. (2022)</a>
39627829549207044	TDE 2018hyz	TDE	<a href="#">Arcavi (2018); Short et al. (2020); Gomez et al. (2020)</a>
39632976878768365	TDE 2021gje	TDE	<a href="#">Hammerstein et al. (2021)</a>
39632941722109945	TDE 2024lhc	TDE	<a href="#">Yao et al. (2024)</a>

objects as being AGN displaying real CrL emission features. This assessment is based on both initial BPT diagnostics, visual inspection of their optical spectra and MIR light curves, and with a comparison of their MIR colours to the previously described [Stern et al. \(2012\)](#) colour cut. Whilst not the primary focus of this work, given their role as significant contaminants in TDE searches, identifying information for each of these objects is provided in Table D1, and we draw attention to several of the most unusual galaxies within this sample.

DESI 39627758191511075 (see Fig. D1) displays broader than usual CrL [Fe VII]  $\lambda 6088\text{\AA}$  emission, accompanied by strong and broad H $\alpha$  emission typical of broad-line AGN and evidence for an underlying blue AGN continuum. In the MIR, DESI 39627758191511075, whilst not having the typical AGN W1-W2 colour above the [Stern et al. \(2012\)](#) cut for selecting AGNs, does display erratic evolution with repeated episodes of brightening and fading at the level of several tenths of a magnitude. Additionally, DESI 39627758191511075 is associated with the unclassified TNS AT 2025ils ([Hall et al. 2025](#)).

DESI 39627671155511332 (see Fig. D2) also displays broader than usual CrL emission features and a multi-peaked MIR light-curve with overall changes in observed brightness  $\sim 0.7$  mag larger than the typical expected variability of AGNs, though with a W1-W2 colour more typical of AGNs.

## APPENDIX E: MIR OUTBURST PEAK ANALYSIS

Here in Table E1, we include the full fitting parameters and statistical test results for the MIR outburst peak analysis as described in Section 6.1 and Fig. 28.

This paper has been typeset from a  $\text{TeX}/\text{\LaTeX}$  file prepared by the author.

**Table C3.** Crossmatch results between the full SLEIPNIR Input Galaxy Sample and the sample of galaxies identified as showing potential CrLs by an earlier version of SLEIPNIR in the search for ECLEs in the SDSS Legacy DR17 survey by [Callow et al. \(2024\)](#).

DESI ID	DESI EDR Classification	SDSS Short Name	SDSS Legacy Classification
39628449278591796	CrL-AGN	SDSS J1300+2824	Rejected <sup>1</sup>
39633066712369198	CrL-AGN	SDSS J0731+3926	Weak CrLs <sup>2</sup>
39633236212582085	CrL-AGN	SDSS J1134+4912	Rejected
39633304827202451	CrL-AGN	SDSS J1606+5340	Weak CrLs
39633416353743637	CrL-AGN	SDSS J1243+6225	Rejected
39627775576903981	-	SDSS J1138-0035	Weak CrLs
39627788335973998	-	SDSS J1420-0004	Weak CrLs
39627799132112775	-	SDSS J0914+0023	Rejected
39627818576909309	-	SDSS J1430+0118	Weak CrLs
39627823480048542	-	SDSS J0959+0126	Weak CrLs
39627836692105274	-	SDSS J1429+0154	Weak CrLs
39628465170813469	-	SDSS J1301+2918	Weak CrLs
39628487006358229	-	SDSS J1648+3022	Weak CrLs
39633274808568349	-	SDSS J1148+5145	Weak CrLs
39633278537304499	-	SDSS J1143+5153	Weak CrLs
39633335630169483	-	SDSS J1204+5602	Weak CrLs
39633338981418326	-	SDSS J1151+5613	Weak CrLs
39633362041702102	-	SDSS J1153+5806	Rejected

*Notes:* <sup>1</sup> SDSS spectrum was manually inspected and determined to be a false positive detection.

<sup>2</sup> In cases of 'Weak CrLs', the SDSS spectrum was not manually inspected as no CrLs exceeded the strength threshold relative to [O III]  $\lambda 5007\text{\AA}$  (20 per cent) used in the [Callow et al. \(2024\)](#).

**Table C4.** Crossmatch results between the full SLEIPNIR Input Galaxy Sample and the sample of galaxies identified as showing potential CrLs by an earlier version of SLEIPNIR in the search for ECLEs in the SDSS BOSS LOWZ survey by [Callow et al. \(2025\)](#).

DESI ID	DESI EDR Classification	SDSS Short Name	SDSS BOSS LOWZ Classification
39632966892126678	-	SDSS J1645+3418	Skyline <sup>1</sup>
39633153945503422	-	SDSS J1546+4415	Skyline
39633296920938570	-	SDSS J1131+5313	Weak CrLs <sup>2</sup>
39633300582564759	-	SDSS J1147+5323	Skyline
39633300582564766	-	SDSS J1147+5323	Skyline
39633304143528511	-	SDSS J1131+5339	Skyline
39633311940741336	-	SDSS J1603+5409	Skyline

*Notes:* <sup>1</sup> SDSS spectrum was manually inspected and determined to be a false positive detection as a result of skyline contamination of one or more CrLs.

<sup>2</sup> In cases of 'Weak CrLs', the SDSS spectrum was not manually inspected as no CrLs exceeded the strength threshold relative to [O III]  $\lambda 5007\text{\AA}$  (20 per cent) used in the [Callow et al. \(2025\)](#) search.

**Table C5.** The results of the MILLIQUAS v8 crossmatch to the SLEIPNIR Input Galaxy Sample. A small portion of the table is included here for guidance of form. The full machine readable version is included in the supplementary material.

DESI ID	DESI EDR Classification	MILLIQUAS ID	MILLIQUAS Classification <sup>1</sup>
39627628482659947	CrL-AGN	SDSS J020852.34-063403.4	AX
39627671155511332	CrL-AGN	DESI 39627671155511332	A
39627694769445378	CrL-AGN	SDSS J022659.82-035015.0	A
39627758170540645	CrL-AGN	SDSS J142827.38-011845.9	Q
39627758191511075	CrL-AGN	PGC 3096363	AX
...	...	...	...

*Note:* <sup>1</sup> Classification description available through the MILLIQUAS documentation: <https://quasars.org/Milliquas-ReadMe.txt>

**Table C6.** The results of the [Ding et al. \(2025\)](#) crossmatch to the SLEIPNIR Input Galaxy Sample. A small portion of the table is included here for guidance of form. The full machine readable version is included in the supplementary material.

DESI ID	DESI EDR Classification	Ding ID	Ding Classification <sup>1</sup>
39627887837451274	CrL-AGN	DESI J027.9525+04.1951	FeX6376
39627902945332471	CrL-AGN	DESI J210.4959+04.6738	NeV3347 NeV3427 FeVII6088
39627956879886559	CrL-AGN	DESI J199.4801+06.9125	NeV3427
39628346308430103	CrL-AGN	DESI J208.7671+23.7873	NeV3427 FeVII6088
39628357146511265	CrL-AGN	DESI J194.5984+24.3064	NeV3427
...	...	...	...

*Note:*<sup>1</sup> Classification indicates which CrLs were detected in the Ding et al. (2025) analysis.

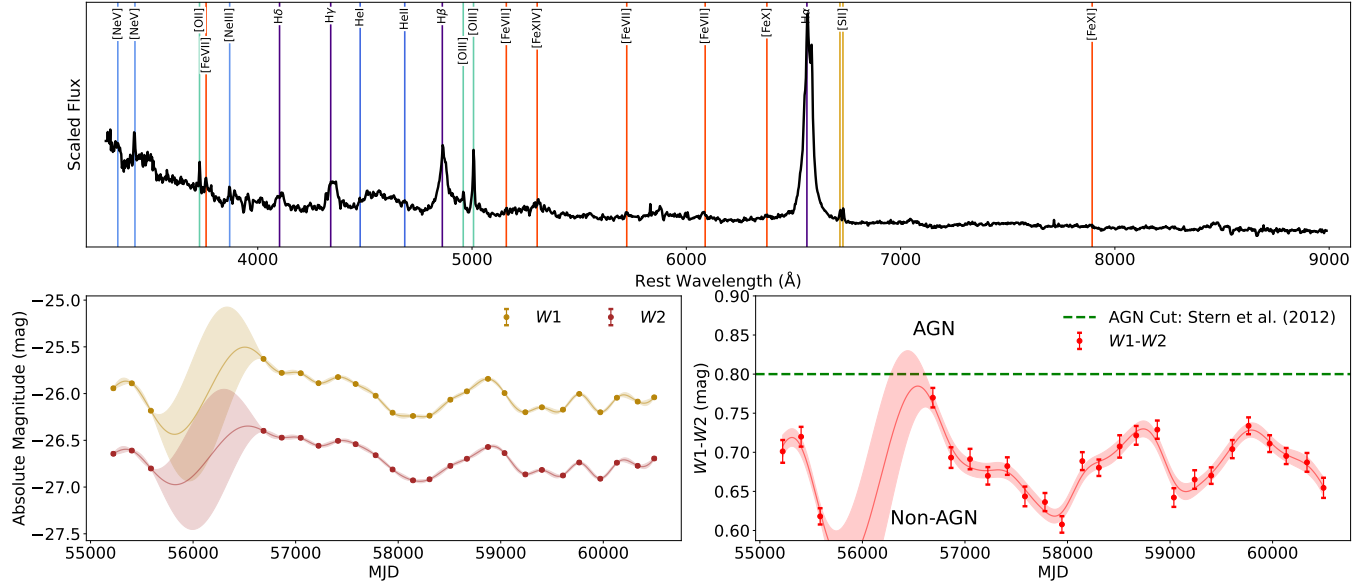


**Figure D1.** *Top:* Spectrum of the unusual CrL AGN DESI 39627758191511075. Prominent emission lines, including the broader than usual Fe CrLs are indicated by the vertical lines. *Bottom Left:* MIR evolution of DESI 39627758191511075 showing repeated variations of  $\sim 0.1$  mag; as expected of an AGN. *Bottom Right:* MIR W1-W2 colour evolution of DESI 39627758191511075, which whilst showing variation, remains below the [Stern et al. \(2012\)](#) selection cut for typical AGNs. In both MIR plots, fits displayed are obtained through Gaussian processes, with the shaded regions indicating the  $1\sigma$  fitting uncertainties.

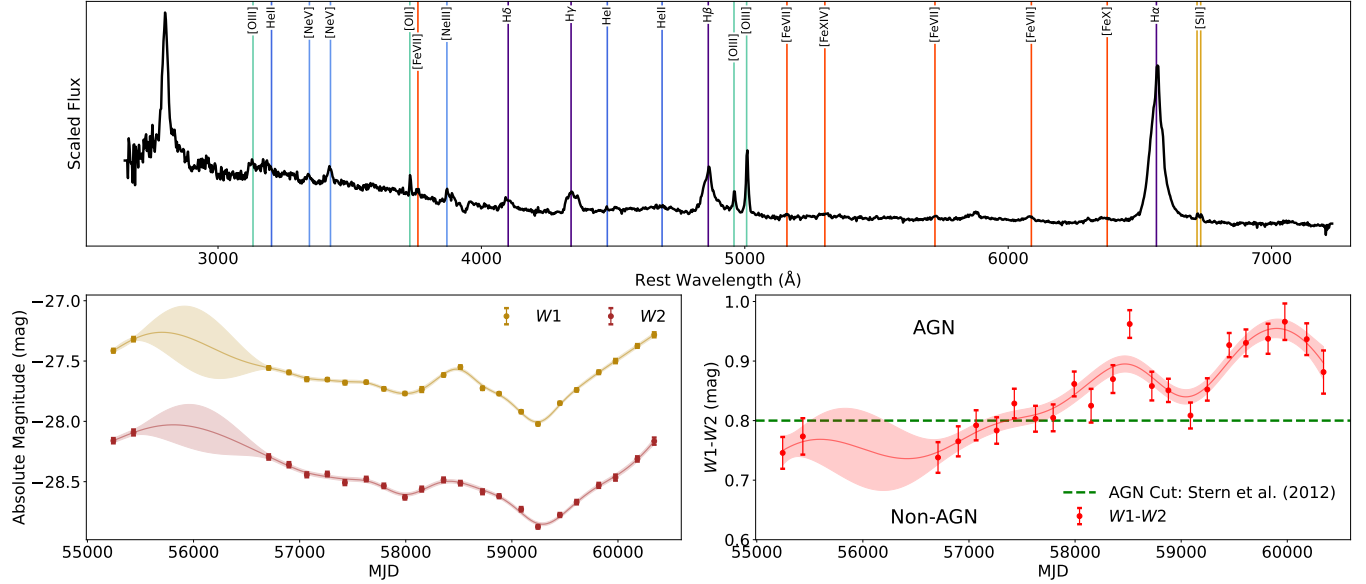


**Figure D2.** *Top:* Spectrum of the unusual CrL AGN DESI 39627671155511332. Prominent emission lines, including the broader than usual Fe CrLs are indicated by the vertical lines. *Bottom Left:* MIR evolution of DESI 39627671155511332 showing several phases of both fading and brightening, most recently brightening by  $\sim 0.7$  mag in both bands. *Bottom Right:* MIR W1-W2 colour evolution of DESI 39627671155511332, which whilst showing repeated variation and long-term reddening trend moving the measured colour above the Stern et al. (2012) selection cut for typical AGNs. In both MIR plots, fits displayed are obtained through Gaussian processes, with the shaded regions indicating the  $1\sigma$  fitting uncertainties.

**Table D1.** Identified information for sources identified as CrL-AGN in the DESI EDR sample. A small portion of the table is included here for guidance of form. The full machine readable version is included in the supplementary material.

DESI ID	RA	DEC	z	z err	EBV
39627628482659947	32.21810	-6.56766	0.238	1.15E-05	0.025
39627630114245131	130.07619	-6.40654	0.095	1.15E-06	0.025
39627640474179036	31.02454	-6.05817	0.298	5.62E-06	0.027
39627671155511332	66.39076	-4.77105	0.359	7.21E-06	0.036
39627694769445378	36.74930	-3.8375	0.292	5.34E-06	0.030
...	...	...	...	...	...

**Table E1.** Fitting parameters obtained in the  $\Delta$  value analysis. Data and fits shown in Fig. 28

Model	Parameter	Value	t-statistic	p-value	$\sigma$
$\Delta W2$ vs $\Delta WI$	Quadratic <sup>*</sup>				
	a	$-0.20 \pm 0.08$	-2.59	4.87e-02	1.97
	b	$0.66 \pm 0.21$	3.07	2.79e-02	2.20
	c	$-0.47 \pm 0.11$	4.36	7.32e-03	2.68
$\Delta(WI-W2)$ vs $\Delta W2$	Linear <sup>□</sup>				
	m	$-0.27 \pm 0.05$	-5.49	5.37e-03	2.78
	c	$0.15 \pm 0.07$	2.21	9.18e-02	1.69

<sup>\*</sup> Selected through maximum likelihood analysis and AIC value comparison between a fixed constant, a linear model and a quadratic model

<sup>□</sup> Selected through maximum likelihood analysis and AIC value comparison between a fixed constant and a linear model. A quadratic model was not included in this comparison due to the small number of data points (six) available for inclusion